Physically accurate advection

A discrete representation of the Lie Derivative

Pedro Pinto Rebelo

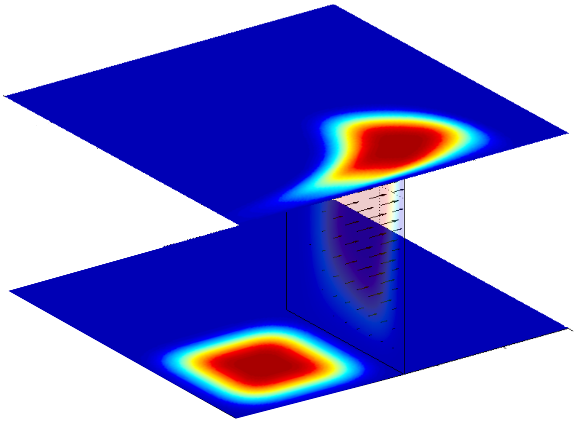

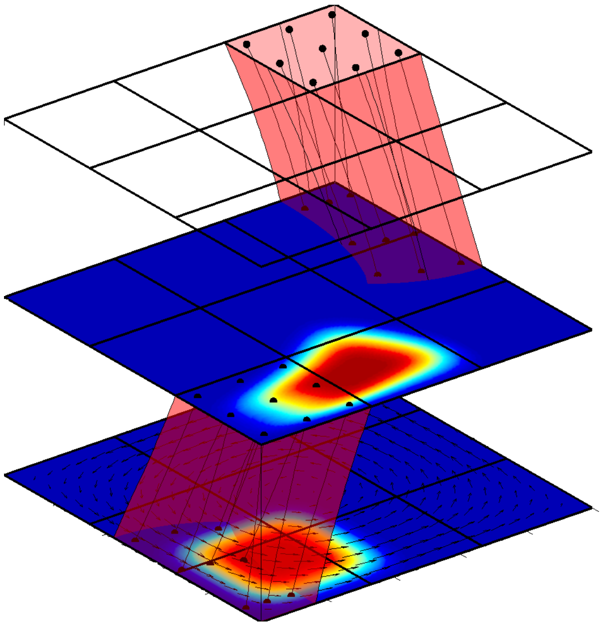

TU Delft
Delft
University of
Technology

Physically accurate advection
A discrete representation of the Lie Derivative

Master of Science Thesis

For the degree of Master of Science in Solid and Fluid Mechanics at
Delft University of Technology

Pedro Pinto Rebelo

December 16, 2011

Faculty of Mechanical, Maritime and Materials Engineering (3mE) · Delft University of
Technology

Copyright © Process and Energy
All rights reserved.

Delft University of Technology
Department of
Process and Energy

The undersigned hereby certify that they have read and recommend to the Faculty of Mechanical, Maritime and Materials Engineering (3mE) for acceptance a thesis entitled

Physically accurate advection

by

Pedro Pinto Rebelo

in partial fulfillment of the requirements for the degree of

Master of Science Solid and Fluid Mechanics

Dated: December 16, 2011

Supervisor(s): Prof.dr.ir. B.J. Boersma

Reader(s): Dr.ir. M.I. Gerritsma

Dr. R. Pecnik

Abstract

Mimetic discretization methods are emerging techniques designed to preserve, as much as possible, properties of the continuous differential equation. In this framework the geometric nature of physics plays a crucial role. Thus, it is necessary to use a new language to model physical problems, Differential Geometry. The calculus of differential forms reveals intrinsic structures that usually, are obscured by metric notions implicitly encoded in vector calculus. In the language of differential forms the unified treatment of scalar and non-scalar advection is simplified by the use of one operator: the Lie Derivative.

Much attention has been devoted to the discretization of scalar advection problems in numerical analysis. Therefore, it would be expected that non-scalar advection is not common or relevant. This is not true. The so-called magnetic advection in electromagnetism or the advection of vorticity in fluid mechanics are examples of important non-scalar fields. Furthermore, it is widely known that the classical Galerkin formulation when applied to scalar convection may lead to spurious (non-physical) oscillations. The goal of this thesis is to derive a physically accurate discretization of the generalized advection problem. Thus, very small or even vanishing artificial diffusion should reflect the robustness of these methods. Also in this thesis, geometric structure-preserving semi-Lagrangian and Eulerian discrete schemes are derived.

For the semi-Lagrangian methods it is necessary to determine the flow of a vector field, i.e. it is necessary to solve a set of ordinary differential equations. A new scheme, that aims to preserve the integral of velocity is presented and compared with high-order fully implicit Runge-Kutta methods. Furthermore, to compute the advection a backtrack algorithm is implemented. It will be shown that this scheme allows for large time steps, but, the error of the backtrack integration proves to be a drawback. For Eulerian methods, the derived scheme is solved based on a flux approach. Here the time step is more restrictive.

Table of Contents

Acknowledgements **xiii**

1 Setting the stage **1**

1-1 Why geometric mechanics? . . . 3

1-2 Outline . . . 5

2 Review of convection-diffusion **7**

2-1 Mathematics behind transport phenomena . . . 8

2-1-1 Convective and Diffusive fluxes . . . 9

2-2 Transport equation . . . 10

2-2-1 Elliptic transport equation . . . 11

2-2-2 Hyperbolic transport equation . . . 11

2-2-3 Parabolic transport equation . . . 12

2-3 Boundary conditions . . . 12

2-4 Numerical and physical constraints . . . 12

3 Old wine new bottles: Differential Geometry **15**

3-1 Geometric modeling . . . 16

3-2 Differential Geometry . . . 17

3-2-1 Differential forms . . . 17

3-2-2 The wedge product between forms . . . 19

3-2-3 Exterior derivative . . . 20

3-2-4 Transformation . . . 22

3-2-5 Generalized Stokes theorem . . . 23

3-2-6 Hodge-$\star$ . . . 24

3-2-7 de Rham complex . . . 25

3-2-8 Codifferential . . . 25

3-2-9 Laplace-deRham 26
3-2-10 Connection between forms and vector fields 26
3-2-11 Interior product & Extrusion 27
3-2-12 Lie Derivative 28

4 Algebraic Topology - The discrete world of differential forms 33

4-1 Cell Complexes 34
4-2 Chains and boundary operator 35
4-3 Cochains and coboundary operator 37
4-4 Discrete de Rham complex 40

5 Numerical implementation 41

5-1 Reduction operator 42
5-2 Reconstruction operator 43
5-3 Reduction and reconstruction of k-forms 45
5-3-1 0-forms 45
5-3-2 1-forms 45
5-4 Multidimensional problems 48

6 Geometric integration 51

6-1 Why preserve structure? 52
6-2 Hamiltonian system 52
6-3 Numerical integrators 54
6-3-1 Explicit Euler 54
6-3-2 Implicit Euler 54
6-3-3 Implicit mid-point 54
6-3-4 Symplectic Euler 55
6-3-5 Stormer/Verlet 55
6-3-6 Runge-Kutta 56
6-3-7 Mimetic geometric integrator 58
6-4 Numerical Experiments 60
6-4-1 Circle 60
6-4-2 Harmonic oscillator 65
6-4-3 Lotka-Volterra model 67
6-4-4 Rudman-Vortex 70
6-4-5 Two-body Kepler problem 70
6-4-6 Perturbed Kepler problem 74
6-4-7 Outer solar system 76

7 Discrete generalized advection 79
7-1 Lagrangian 80
7-2 Semi-Lagrangian 81
7-3 Eulerian 91
    7-3-1 2D 94

8 Conclusions 101
8-1 Future work 102

A Edge Functions 103
A-1 The edge functions 103
    A-1-1 Gradient operator 105
    A-1-2 Curl operator 106
    A-1-3 Divergence operator 107

B Geometric integration tableaus 109
B-1 Gauss 109

C Outer solar system 113

Bibliography 115

List of Figures

1-1 Approximation of the first order system for Poisson's equation, with $u = x(1 - x)y(1 - y)$ [1]. 3

2-1 Smoke plume of oil explosion in Baghdad 7
2-2 A fixed control volume V bounded by the control surface S 8
2-3 A fixed control volume V bounded by the control surface S 9
2-4 A fixed control volume V bounded by the control surface S 9

3-1 Geometric interpretation of the generalized Stokes theorem 24
3-2 Geometric interpretation of the extrusion concept 28
3-3 Advection of a 2-form by a divergence-free vector field 30

4-1 Cell complex for $\mathbb{R}^3$ and $\mathbb{R}^2$ 34
4-2 Different orientations for the cell complex in $\mathbb{R}^2$ 34
4-3 Boundary operator action in $\mathbb{R}^2$ and $\mathbb{R}^3$ 36
4-4 Coboundary operator example 38
4-5 Numbered primal and dual cell complex in $\mathbb{R}^2$ 39
4-6 Primal and dual cell complex in $\mathbb{R}^3$ 40

5-1 Reduction and exterior derivative of a 0-form for $sin(2\pi x)$ 43
5-2 Reduction and Reconstruction of a 1-form for $sin(2\pi x)$ 44
5-3 Reduction and reconstruction of a 0-form for $sin(2\pi x) + 1$ 46
5-4 Reconstruction basis functions on Gauss-Lobatto nodes 47
5-5 Reduction and reconstruction of a 1-form for $sin(2\pi x) + 1$ 48
5-6 Reduction and reconstruction of a k-form in $\mathbb{R}^2$ 50

6-1 Geometric interpretation of the Stormer/Verlet method [2] 55

6-2 Geometric interpretation of Runge-Kutta method for $\dot{y} = t^2+y^2$, $y_0 = 0.46$, $h = 1$; dotted: exact solution [2] . . . 57

6-3 Mimetic integrator explained for $\dot{y} = t^2 + y^2$ with $\Delta t = 1$ and $y_0 = 0.46$ . . . 59

6-4 Symmetry behavior of the mimetic integrator . . . 60

6-5 Circle phase plot for different integration schemes . . . 61

6-6 Energy error of Gauss vs Mimetic for the circle problem . . . 62

6-7 L2 error of Gauss vs Mimetic for the circle problem . . . 62

6-8 Hamiltonian and radius error of Gauss and mimetic method for the circle problem with $\Delta t = 0.1$ and $p = 3$ . . . 63

6-9 Hamiltonian and radius error of Gauss vs Mimetic for the circle with $\Delta t = 0.01$ for 100 seconds . . . 64

6-10 Hamiltonian and radius error of Gauss vs Mimetic for the circle with $\Delta t = 0.1$ for 100 seconds . . . 64

6-11 Hamiltonian and radius error of Gauss vs Mimetic for the circle with $\Delta t = 1$ for 100 seconds . . . 65

6-12 Phase plot of the pendulum problem for different integration schemes . . . 66

6-13 Gauss vs Mimetic for the pendulum problem after 10 seconds of physical time . . 67

6-14 Lotka-Volterra phase plot . . . 68

6-15 Gauss vs Mimetic for the Lotka-Volterra problem after 10 seconds . . . 69

6-16 Hamiltonian error for the Lotka-Volterra problem function of number of iterations with $\Delta t = 0.01$ . . . 69

6-17 Phase plot for the Rudman-Vortex problem with different integration schemes . . 71

6-18 Gauss vs Mimetic for the Rudman-Vortex problem . . . 72

6-19 Kepler $(q_1.q_2)$ plot for 2000 $steps$ with $\Delta t = 0.1$ . . . 73

6-20 Energy error of Gauss vs Mimetic for the Kepler problem . . . 74

6-21 Plot (q_1, q_2) for the perturbed Kepler problems with constant step size, $\Delta t = 0.065$ 75

6-22 Outer solar system phase plot. $\Delta t = 100$, $2000 steps$ . . . 77

7-1 Lagragian mesh movement (p = 1; p = 4; p = 30); . . . 80

7-2 Flux backtrack method . . . 82

7-3 Path tube method . . . 82

7-4 Comparison between the 1D advection of a 1-form, $sin(2\pi x) + 1dx$, with the analytical solution for the path tube method . . . 83

7-5 Space-time 1D advection of a 1-form, $sin(2\pi x) + 1dx$ by the flux backtrack method 84

7-6 Space-time 1D advection of a 1-form, $sin(2\pi x) + 1dx$ by the path tube method 85

7-7 L^2 error of the path tube method for $N = 100$ with $p_x = 10$ . . . 86

7-8 Integration error for semi-Lagrangian methods in 1D . . . 86

7-9 L^2 error of the path tube method for 10 seconds with $\Delta t = 0.01$ . . . 87

7-10 L^2 error of the flux backtrack method for $N = 100$ with $p_x = 10$ . . . 87

7-11 L^2 error of the flux backtrack method for $\Delta t = 0.01$ . . . 88

7-12 2D advection of a 2-form Gaussian bell with $N_x = N_y = 4$ and $p_x = p_y = 9$ . . 89

7-13 2D backtrack of the integration points for $p = 9$ after 1 second of simulation time (the origin of quadrature errors) . . . 90

7-14 Mass error for the 2D path tube method . . . 90

7-15 Different quadrature approach to compute the integral values in the 2D path tube method . . . 91

7-16 Boundary conditions implementation [3] . . . 91

7-17 Geometric representation of the time marching scheme . . . 92

7-18 Comparison between the 1D advection of a 1-form, $sin(2\pi x) + 1dx$, with the analytical solution . . . 94

7-19 Space-time 1D advection of a 1-form, $sin(2\pi x) + 1dx$ . . . 95

7-20 L^2 error of the Eulerian method for $N = 100$ and $p_x = 10$ . . . 96

7-21 Convergence plot for the initial and after advection of $\rho^1 = sin(2\pi x) + 1dx$ with $\Delta t = 10^{-4}$ (– – Initial ; — Final) . . . 96

7-22 Time error advection of a 1-form, $sin(2\pi x) + 1dx$ . . . 97

7-23 Space-time 1D advection-diffusion of a 1-form, $sin(2\pi x)+1dx$ with $N = 90$,$px = 10$ and a diffusion coefficient = 1 [4] . . . 98

7-24 2D advection of a 2-form Gaussian bell with $N_x = N_y = 10$ and $p = 4$ . . . 98

7-25 2D advection of a 0-form Gaussian bell with $N_x = N_y = 10$ and $p = 4$ . . . 100

A-1 Geometric representation of the discrete gradient operator . . . 106

A-2 Geometric representation of the discrete curl operator . . . 107

A-3 Geometric representation of the discrete divergence operator . . . 108

List of Tables

2-1 Type of equation for the transport problem 11

3-1 Forms used in Electromagnetism 16
3-2 Forms available in $\mathbb{R}^3$ 18
3-3 Duality paring for k-forms in $\mathbb{R}^3$ 18
3-4 Example of physical variables associated with k-forms 19
3-5 Relation between the exterior derivative and vector calculus operations 21
3-6 Pull-back action on k-forms in $\mathbb{R}^3$ 22
3-7 Connection between the integral theorems in vector calculus and differential geometry 23
3-8 Action of the Laplace-deRham onto forms in $\mathbb{R}^2$ 26
3-9 Algebraic and dynamic definition of the Lie derivative and the interior product . . 31
3-10 Connection between differential geometry operators and vector calculus in $\mathbb{R}^3$ . . 31

4-1 Coboundary operator $\mathbb{D}^{(1,0)}$ for the labeled cochain complex of Figure 4-5 39
4-2 Coboundary operator $\mathbb{D}^{(2,1)}$ for the labeled cochain complex of Figure 4-5 39

5-1 Connection between differential forms and co-chains established by the Reduction operator 42
5-2 Reconstruction of k-forms for $\mathbb{R}^3$ 49
5-3 Reconstruction of k-forms for $\mathbb{R}^2$ 49

6-1 Genral Butcher tableau 56
6-2 Fourth order explicit Runge-Kutta 57
6-3 Gauss-Legendre method of order 4 ($s = 2$) 58

B-1 Gauss method of order 6 109
B-2 Gauss method of order 8 110

B-3 Gauss method of order 10 111

C-1 Mass of the planets relative to the mass of the sun for the outer solar system simulation 113
C-2 Initial position and velocity of the planets relative to the mass of the sun for the outer solar system simulation 114

Acknowledgements

First and foremost, I would like to thank to my supervisor, Marc Gerritsma, for giving me the opportunity to work in such new and interesting topic; for giving me the freedom to try and explore new things; and obviously without his guidance and support this thesis wouldn't have been possible. I am also deeply grateful to Artur Palha, for his patience, guidance, ideas and incredible help developing this work. Furthermore, I am also grateful to the mimetic group, Jasper, Guido, Demian, Dennis, Rene, Peter and Deepesh for sharing their ideas and insights.

For the rest of the basement students thanks for drinks, dinners, lunches, politics and economics discussions. It was really a pleasure. Obviously, I cannot forget my brothers in pizza and afternoons/nights work during the master. Without Pejman, Maximo, Can and Arjang it would have been impossible to finish my studies in Delft. Before the master there was a bachelor. I cannot thank enough to everyone who I met during that time. Without Paulo, Martinho, Ze, Telmo, Lenny and so many other it wouldn't have been so funny and "easy" to finish it. To Hugo, that is stalking me since my days in Porto, goes a special thanks for his support and always going-out mood.

Furthermore, I would like to give a big thank you to all my friends back at my hometown. Isabel(s), Santos, Gambo, JP, Raquel, Tatiana, CÃątia, InÃłs and Helena for never leaving the spot at Vitor alone. I would also like to express my gratitude to my brother, JoÃčo, and AdÃľla for the small Portuguese/Czech place always with some good beer, wine, great food and awesome people there. Finally, I would like to thank to all my family mainly to my parents for their support, in several ways, without it any of this would be meaningful.

Obrigado a todos!!

“Any intelligent fool can make things bigger and more complex... It takes a lot of courage to move in the opposite direction.” — *Albert Einstein*

Chapter 1

Setting the stage

Physics in essence is an observing and measuring science. Associated with every object measured there is spatial and temporal geometric object. Thus, physical laws are no more than a relation between these different objects. Many of these laws are characterized by symmetries and invariants. For example, momentum preservation is a consequence of space symmetry, i.e space is all the same, from a mathematical point of view there is not a preferred origin. This connection between conservation laws and certain symmetries is elegantly formulated by Noether's theorem. Thus, preserving these structures numerically, independent of the order of accuracy of the method, is crucial to avoid unphysical solutions [5]. For example, it is known that linear momentum is preserved when dealing with the motion of a rigid body. Obviously, when designing a simulation of this system the linear momentum should also be preserved. This principle is likelihood to remove any unphysical behavior. The goal of structure preservation from the continuous equation to their discretization will be constant in this thesis.

The so-called geometric methods are designed with the clear goal to preserve symmetries and invariants. Geometry plays a vital role in this derivation. Consider an object with a certain mass and volume, the average mass density is the mass divided by the volume. Until this point, it is clear that average mass density is connect with a volume. In the purely mathematical world, consider that in the limit the volume tends to zero, which allows to compute density in a point. However, as small the limit can get the volume is never a point. These two views are the principles of integral and differential modeling, respectively. The integral modeling is the physical foundation of mimetic methods. The fact that physical laws are derived without mathematical abstractions, i.e. the limiting process, leads to a more physical discretization process. Furthermore, the association of physical variables to spatial and temporal geometric objects has deserved attention of several authors, [6, 7, 8, 9].

On the other hand, it was proven that the use of classic vector calculus is inadequate in fully encoding physical quantities and their relation with geometry. Hence, it is necessary to find a mathematical language that can encode different geometric structures in a concise and consistent manner for both smooth and curved spaces. Differential geometry provides this framework. Moreover, this language allows a clear identification of metric (angles, lengths, distances, etc) and non-metric (topological) components. In its core is the concept of differential form, that is an abstraction of the measurement process. Hence, the machinery of this coordinate-free approach are the line, surface and volume integral.

Finding a discrete notion of differential geometry is a crucial point in mimetic methods. Algebraic topology proves to be deeply connected with differential geometry and its objects. Mainly, the concepts of chains and cochains provide a natural tool to discretize exterior calculus in finite grids. Chains are related with the geometric objects of the finite grid, i.e. vertices, edges, surface and volumes. On the other hand, cochains are pointwise functions, line integrals, surface integrals and volume integrals. This view is perfectly compatible with the use of scalar functions, as in finite element methods, or volume integrals, as in finite volume methods [10]. In fact, it uses edge elements and facet elements introduced in the electromagnetism framework as H_{div} and H_{curl}.

The so-called discrete exterior calculus (DEC) [11], or equivalently, the mimetic finite difference approach [12], or finite element exterior calculus [1] proposes similar discretizations that preserve vector calculus fundamental identities. The use of differential geometry in the context of electromagnetism is wide spread [7]. However, its application to fluid mechanics remains limited.

Recently [13] established a general framework combining mimetic discretizations with spectral methods. Spectral/high-order methods are established tools in the field of discretization of PDE's [14, 15]. These methods use high-order basis functions. Its application to algebraic topology, which is the discrete counterpart of differential forms, is done in order to introduce smoother interpolation functions and use the valuable convergence properties of spectral elements.

The objective of this work is to model the generalized advection equation through the framework of differential geometry, by discretizing the Lie derivative. This treatment of advection allows a generalization from scalar to non-scalar fields. The advection of scalar fields is common and several numerical schemes have been proposed to solve these types of hyperbolic conservation laws [16, 17, 18, 19]. Recently, [20] have extended this applications to non-scalar fields using finite volume schemes based on DEC. Low numerical diffusion is attainable through the use of high-resolution finite volume methods. A similar approach, however, in context of finite element methods have been proposed by [21]. A different approach that combines differential geometry and variational calculus has been proposed by [22]. The realization that the loss of Lagrangian structures is a major numerical impediment of standard numerical techniques [23] is the foundation of this work.

1-1 Why geometric mechanics?

A common goal when designing numerical methods is to search for converge under refinement, i.e. when the size of the discrete element goes to zero the results accurately represent the continuous physical system. However, in the long term, even having convergence under refining, the numerical scheme might reveal inaccurate since important invariants are not kept in mind. The following examples give an insight on this.

As mentioned before, vector calculus tends to blur underlying mathematical structures. A common example is to consider the well-known Poisson equation, $\Delta p = f$, where $\Delta = \frac{\partial^2}{\partial x^2} + \frac{\partial^2}{\partial y^2}$. This can be rewritten as a first order system,

$$\Delta p = f \Leftrightarrow \begin{cases} \nabla \cdot q = f \\ \nabla p = u \\ u = q \end{cases} \tag{1-1}$$

Both equations in (1-1) can be discretized in an exact way, i.e. without error,

$$\begin{cases} \nabla \cdot q = f \\ \nabla p = u \\ u = q \end{cases} \iff \begin{cases} q_{i,j} - q_{i-1,j} + q_{i,j} - q_{i,j-1} = f_{i,j} \\ u_{i,j} = p_{i,j} - p_{i-1,j} \\ u_{i,j} = q_{i,j} \end{cases} \tag{1-2}$$

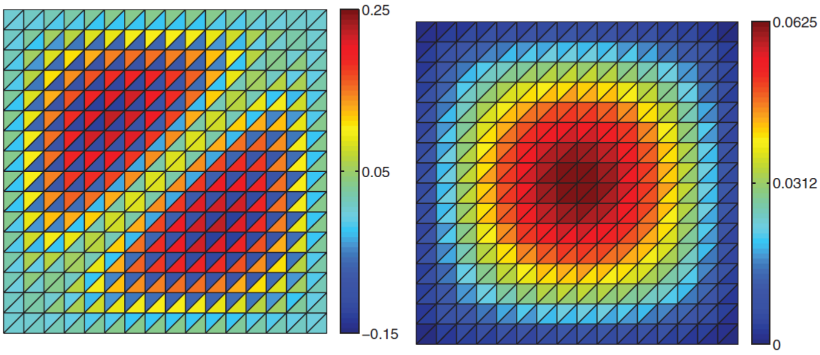

(a) Piecewise constants for p and u

(b) Piecewise constants for p and Raviart-Thomas elements for u

Figure 1-1: Approximation of the first order system for Poisson's equation, with $u = x(1-x)y(1-y)$ [1].

Naively, it would be expected that using (1-2) a solution without error would be retrieved. This is not true [1]. The reason for this is that in fact p and u cannot be discretize in the same way, i.e. as point value quantities, because they have different geometric interpretation. Inside the FEM community this has been identified as shown in Figure 1-1, where a comparison between using piecewise constants for p and, either, piecewise linear (Figure 1-1a) or edge Raviart-Thomas elements (Figure 1-1b) for u. It will be shown in the following section if one was aware of the geometry behind the problem the immediate choice would be the edge Raviart-Thomas elements.

The uncertain geometric nature of vector calculus is also revealed in the treatment of scalar fields. Consider a temperature field, $T(x, y, z)$ and a mass density field, $\rho(x, y, z)$. Both are scalar fields, however, one is associated with *point* values and the other as an average of mass per *volume*. The same problem occurs if one consider a potential flow, $\mathbf{u}(x, y, z) = \nabla\phi$ and a flux vector $\mathbf{f}(x, y, z)$. The first is defined along *line* segments and the second one along *surfaces*. However, in vector calculus both are described by vectors. These two intuitive examples prove the lack of crucial information to give proper representation of physical variables by vector calculus.

Lets consider the motion of a single body. Its dynamic behavior can be described by Newton's second law, $\mathbf{F} = m\mathbf{a}$ or equivalently,

$$\begin{aligned} \dot{x} &= v \\ \dot{v} &= \frac{F}{m}, \end{aligned} \tag{1-3}$$

where, $\dot{x}$ represents the velocity of the system and $\dot{v}$ the acceleration. Using an explicit Euler to discretize these ODE's,

$$\begin{aligned} x_{k+1} &= x_k + \Delta t v_k \\ v_{k+1} &= v_k + \Delta t \frac{F\left(x_k\right)}{m}. \end{aligned} \tag{1-4}$$

Alternatively, to Newton's second law an Hamilton's principle can be considered, this lead to the following system of ODE's,

$$\begin{aligned} x_{k+1} &= x_k + \Delta t v_{k+1} \\ v_{k+1} &= v_k + \Delta t \frac{F\left(x_k\right)}{m}. \end{aligned} \tag{1-5}$$

Both methods have the same accuracy and convergence to the correct solution when refined. However, the second one even using coarser meshes preserve a crucial property, the Hamiltonian.

1-2 Outline

Here is a brief summary of the contents of this thesis. In Chapter 2 a revision of the standard modeling of convection-diffusion is presented. Afterwards, in Chapter 3 the concepts of differential geometry of continuous modeling of physical problems are introduced. It will be shown that convection can be modeled by means of the Lie derivative and it can be seen in a more dynamic or algebraic approach that later will be the foundation of the semi-Lagrangian and Eulerian description, respectively.

The next chapter, Chapter 4, presents the connection between the discrete algebraic topology and the continuous differential geometry world. The discrete version of the metric free vector operators, **grad**, **curl** and **div** is presented.

Chapter 5 defines two crucial numerical operators, the reduction and reconstruction, that generalizes the approximation spaces. Afterwards, in Chapter 6 different type of ODE solvers are compared for different test cases, this will be the base for the dynamic view of convection.

Finally in Chapter 7 the generalized convection is computed. The computations are divided in two main fields, Semi-Lagrangian and Eulerian. In each section both 1D and 2D test cases are presented. The conclusions and future perspectives are presented in Chapter 8.

Chapter 2

Review of convection-diffusion

Rarely, heating, air conditioning and weather forecast are considered in terms of the math and physics involved. Fluid dynamics and transport phenomena, such as heat and mass transport are a critical part involved in these systems. Convection and diffusion are responsible for temperature fluctuations and transport of pollutants in air, water or soil. Therefore, the ability to predict these phenomena is essential. Figure 2-1 shows a practical example.

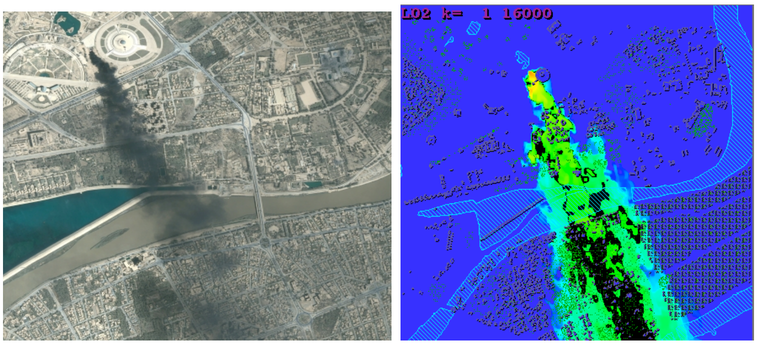

(a) Top view of the smoke plume

(b) CFD simulation

Figure 2-1: Smoke plume of oil explosion in Baghdad

This chapter gives a brief introduction to the mathematical structures of transport equations. A more detail discussion can be found [16]. Section 2-1 reviews the concept of convection and diffusion and their mathematical modeling, respectively. Afterwards, Section 2-2 details the different mathematical nature that the transport equations possess. Section 2-3 models boundary conditions. Finally, in Section 2-4 details of the numerical and physical constraints are discussed.

2-1 Mathematics behind transport phenomena

Consider an arbitrary control volume, $V \in \mathbb{R}^d$, where d is the number of space dimensions. If the fluid is in motion, it can flow across the control surface S which forms the boundary of V. Figure 2-2 gives an example of such control volume.

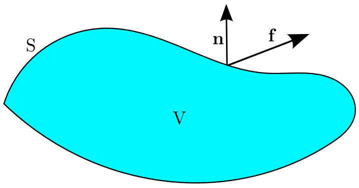

Figure 2-2: A fixed control volume V bounded by the control surface S

Let $c(\mathbf{x}, t) \in \mathbb{R}$ denote the concentration (amount per unit mass) of a scalar conserved quantity at point $\mathbf{x} \in V$ and time $t \geq 0$. The concentration per unit of volume is given by $u = \rho c$, where ρ is the mass density of the carrier fluid. The total amount of the conserved variable inside V is given by the volume integral,

$$C_v = \int_V u(\mathbf{x}, t) d\mathbf{x} = \int_V \rho(\mathbf{x}, t) c(\mathbf{x}, t) d\mathbf{x}. \tag{2-1}$$

The time rate of change of C_v of (2-1) depends on the rate at which c flows, i.e enters or leaves V through the boundary S. This rate is called flux and denoted by

$$\mathbf{f}(\mathbf{x}, t) = (f^1, \ldots, f^d),$$

where f^k corresponds to the rate of transport in the k-th coordinate direction, per unit area and time. If $\mathbf{ds} = \mathbf{n}ds$ is an infinitesimally small patch of S with the unit outward normal $\mathbf{n}$, then the mass crossing this patch per unit time is $\mathbf{f} \cdot \mathbf{n}ds$. In the simplest case, the flux vector $\mathbf{f}$ is a linear function of u and\or $\rho\nabla c$, where $\nabla = \left(\frac{\partial}{\partial x_1}, \ldots, \frac{\partial}{\partial x_d}\right)$.

Processes such as chemical reaction or heating give rise to interior sources or sinks that generate $s(\mathbf{x}, t)$ units of concentration per unit volume and time. Thus, the temporal variation of (2-1) satisfies the integral conservation law of the form

$$\frac{\partial}{\partial t} \int_V u(\mathbf{x}, t) d\mathbf{x} + \int_S \mathbf{f} \cdot \mathbf{n} ds = \int_V s(\mathbf{x}, t) d\mathbf{x}. \tag{2-2}$$

The surface integral is the mass that leaves V per unit area and time, whereas the right-hand side of (2-2) corresponds to the mass produced inside V per unit time. If the functions $u(\mathbf{x}, t)$ and $f(\mathbf{x}, t)$ are differentiable, then the divergence theorem applied to the surface integral in (2-2) yields

$$\int_V \left[\frac{\partial u(\mathbf{x}, t)}{\partial t} + \nabla \cdot f(\mathbf{x}, t) - s(\mathbf{x}, t) \right] d\mathbf{x} = 0.$$

Since any V can be chosen arbitrarily the following partial differential equation emerges,

$$\frac{\partial u(\mathbf{x}, t)}{\partial t} + \nabla \cdot f(\mathbf{x}, t) = s(\mathbf{x}, t). \tag{2-3}$$

2-1-1 Convective and Diffusive fluxes

Convection consists in the transport of quantities of interest with the fluid flow. For example, consider an horizontal pipe filled with water that flows from the left to the right with constant velocity. Consider the leaf at time $t = 0$ displayed in Figure 2-3. After a certain time interval, Δt, the leaf has moved towards the outlet.

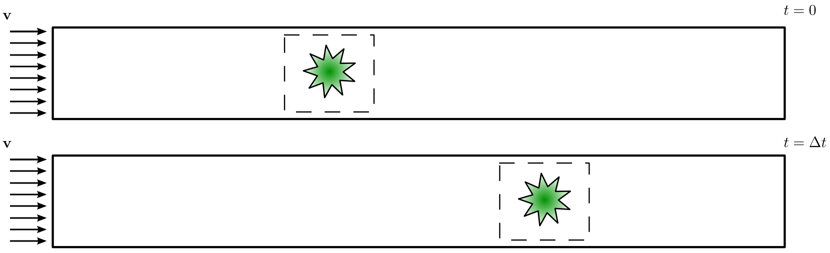

Figure 2-3: A fixed control volume V bounded by the control surface S

Another mechanism that allows transport is *diffusion*. Random molecular motion induces the diffusive fluxes. For instance, consider a tank where the left half contains ink and the left-right water. At time $t = 0$ there is a diaphragm that divides the tank in half. After removing the diaphragm the system will tend to equilibrium. This means that the ink will dissolve in the water.

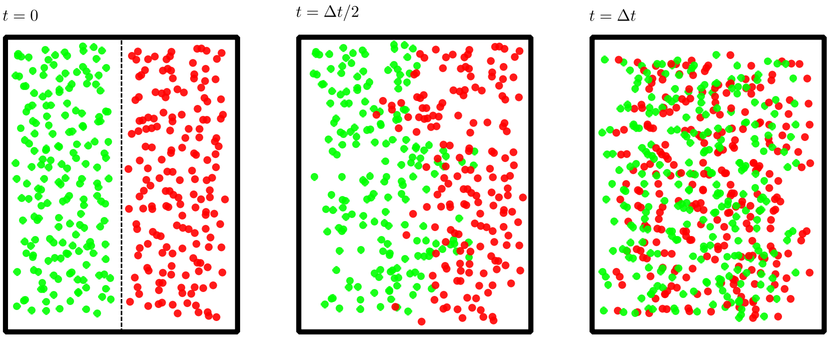

Figure 2-4: A fixed control volume V bounded by the control surface S

Knowing the velocity field $v(\mathbf{x}, t)$ the volume of fluid that crosses an infinitesimally small patch $\mathbf{ds} = \mathbf{n}ds$ during a small time interval dt is

$$dV = (\mathbf{v} \cdot \mathbf{n}ds)dt.$$

If the $\mathbf{n}$ is taken to be the unit vector along the coordinate direction, the convective flux

$$\mathbf{f}_C = \mathbf{v}(\mathbf{x}, t)u. \tag{2-4}$$

On the other hand, the diffusion process is driven by the gradients of the concentration field. The diffusive flux vector is,

$$\mathbf{f}_D = -\mathbb{D}(\mathbf{x}, t)\rho\nabla c, \tag{2-5}$$

where $\mathbb{D} = \{d_{ij}\}$ is a symmetric positive definitive diffusivity matrix. For a isotropic diffusion in all coordinate directions $d(\mathbf{x}, t) > 0$ the diffusive flux reduces to

$$\mathbf{f}_D = -d(\mathbf{x}, t)\rho\nabla c. \tag{2-6}$$

Thus, the total flux is given by

$$\mathbf{f}(\mathbf{x}, t) = \mathbf{v}(\mathbf{x}, t)u - \mathbb{D}(\mathbf{x}, t)\rho\nabla c. \tag{2-7}$$

The relative strength of $\mathbf{f}_C$ and $\mathbf{f}_D$ can be expressed in terms of the Peclet number

$$Pe = \frac{vL}{d}, \tag{2-8}$$

where v is the reference velocity, L the geometric length reference and d the diffusion coefficient. Thus, in the limit for pure convection the Peclet number is infinitive and for pure diffusion is zero.

2-2 Transport equation

The generic transport partial differential equation is given by

$$\frac{\partial \rho c}{\partial t} + \nabla \cdot (\mathbf{v}\rho c) - \nabla \cdot (\mathbb{D}\rho\nabla c) = s. \tag{2-9}$$

The terms of 2-9 correspond:

- $\frac{\partial \rho c}{\partial t}$ the net gain \loss of concentration per unit volume and time;
- the convective term $\nabla \cdot (\mathbf{v}\rho c)$ due to transport by the fluid velocity $\mathbf{v}$;
- the diffusive term $-\nabla \cdot (\mathbb{D}\rho\nabla c)$ due to nonuniform distribution of the concentration c;
- s the source or sink

In this thesis the parameters ρ, $\mathbf{v}$, $\mathbb{D}$ and s are assumed to be known. Moreover, (2-9) can also be formulated in terms of $u = \rho c$

$$\frac{\partial u}{\partial t} + \nabla \cdot (\mathbf{v}u) - \nabla \cdot (\mathbb{D}\nabla u) = s. \tag{2-10}$$

Furthermore, if the velocity field $\mathbf{v}$ is incompressible, $\nabla \cdot \mathbf{v} = 0$, then

$$\nabla \cdot (\mathbf{v}u) = \mathbf{v} \cdot \nabla u + (\nabla \cdot \mathbf{v})u.$$

Then,

$$\frac{\partial u}{\partial t} + \mathbf{v} \cdot \nabla u - \nabla \cdot (\mathbb{D}\nabla u) = s. \tag{2-11}$$

Alternatively take the average of (2-10) and (2-11) which gives the skew-symmetric form of the convective term,

$$\frac{\partial u}{\partial t} + \frac{1}{2}\mathbf{v} \cdot \nabla u + \frac{1}{2}\nabla \cdot (\mathbf{v}u) - \nabla \cdot (\mathbb{D}\nabla u) = s. \tag{2-12}$$

Note that the previous three formulations are equivalent for divergence-free velocity-fields but only (2-10) is conservative for $\nabla \cdot u \neq 0$. Equation (2-10) has a variety of types of differential equations that are summarized in Table 2-1.

Table 2-1: Type of equation for the transport problem

Elliptic	$\nabla \cdot (\mathbf{v}u - \mathbb{D}\nabla u) = s$ $-\nabla \cdot (\mathbb{D}\nabla u) = s$
Hyperbolic	$\nabla \cdot (\mathbf{v}u) = s$ $\frac{\partial u}{\partial t} + \nabla \cdot (\mathbf{v}u) = s$
Parabolic	$\frac{\partial u}{\partial t} + \nabla \cdot (\mathbf{v}u - \mathbb{D}\nabla u) = s$ $\frac{\partial u}{\partial t} - \nabla \cdot (\mathbb{D}\nabla u) = s$

2-2-1 Elliptic transport equation

If the system reaches an equilibrium between convection and diffusion the time derivative at (2-10) vanishes

$$\nabla \cdot (\mathbf{v}u - \mathbb{D}\nabla u) = s. \tag{2-13}$$

This is a second-order elliptic type of PDE. In elliptic problems the information does not have a preferred direction,but rather, propagates in all directions. Thus, the change of solution u at point $\mathbf{x}_1 \in \Omega$ may influence the solution at any other point $\mathbf{x}_2 \in \Omega$.

Furthermore, for the steady-diffusion process, i.e. $\mathbf{v} = 0$ is also a elliptic PDE,

$$-\nabla \cdot (\mathbb{D}\nabla u) = s. \tag{2-14}$$

Considering a constant diffusion coefficient, d, then the following Poisson equation emerges

$$-\Delta u = f. \tag{2-15}$$

2-2-2 Hyperbolic transport equation

Consider purely convective transport, $\mathbb{D} = 0$. In that case the following hyperbolic PDE appears in steady state

$$\nabla \cdot (\mathbf{v}u) = s. \tag{2-16}$$

For this type of equations the information is transported at a finite speed along the streamlines of the stationary velocity field $\mathbf{v}(\mathbf{x})$. Boundary conditions must be specified at the inflow part.

For the unsteady case,

$$\frac{\partial u}{\partial t} + \nabla(\mathbf{v}u) = s. \tag{2-17}$$

2-2-3 Parabolic transport equation

Consider now the unsteady diffusion process with constant diffusion,

$$\frac{\partial u}{\partial t} - d\Delta u = s. \tag{2-18}$$

This is a parabolic equation, even though, the steady part corresponds to an elliptic equation. Furthermore, in these type of equations the information travels forward in time at infinite speed and there is no backward influence.

2-3 Boundary conditions

Let $\Omega \in \mathbb{R}^d$ be a bounded domain and let the time interval vary between 0 and T. The boundary part Γ of Ω consists in an inflow part $\Gamma_- = \{\mathbf{x} \in \Gamma | \mathbf{v} \cdot \mathbf{n} < 0\}$, an outflow part $\Gamma_+ = \{\mathbf{x} \in \Gamma | \mathbf{v} \cdot \mathbf{n} > 0\}$ and a solid wall $\Gamma_0 = \{\mathbf{x} \in \Gamma | \mathbf{v} \cdot \mathbf{n} = 0\}$, where $\mathbf{n}$ denotes the unit outward normal to the boundary at the point $\mathbf{x} \in \Gamma$.

If the values of u are known on $\Gamma_D \in \Gamma$ it is possible to prescribe Dirichlet boundary conditions

$$u(\mathbf{x}, t) = u_D(\mathbf{x}, t), \qquad \forall \mathbf{x} \in \Gamma_D, \forall t \in (0, T). \tag{2-19}$$

Alternatively, a given normal flux can be prescribed defined as Neumann boundary condition

$$\mathbf{f} \cdot \mathbf{n} = g(\mathbf{x}, t), \qquad \forall \mathbf{x} \in \Gamma_N, \forall t \in (0, T). \tag{2-20}$$

Additionally, an initial state should be prescribed

$$u(\mathbf{x}, 0) = u_0(\mathbf{x}), \qquad \forall \mathbf{x} \in \Omega. \tag{2-21}$$

2-4 Numerical and physical constraints

In order to design reliable numerical schemes there are important constraints to take into account, mainly

- Consistency means that as numeric parameters are refined (e.g mesh size, time step, order of the method,etc) the discrete equations tends to the continuous representation;

- Stability concerns the fact that numerical errors (e.g. roundoff) are not amplified;
- Convergence measures the error between the discrete and exact solution as numeric parameters are refined.

Some discretization techniques might converge to stable numerical solutions however if they do not respect the physics of the problem they are useless. Therefore, concepts like:

- Conservation property is an essential requirement for the solution of transport phenomena. The fact that the physical laws are build under this principle should also be reflected in the numerical solution;
- Boundedness means that the solution must be within a certain range. For example, temperature or density cannot be negative;
- Causality assures that the information travels at the right speed and direction.

Chapter 3

Old wine new bottles: Differential Geometry

As the title suggests, this chapter does not intend to reformulate or reinvent mathematical concepts that are well studied. In fact, it intends to introduce a powerful new language, differential geometry, to describe physical models. The aim is the possibility to rewrite physical models with a deep connection with a geometric basis. This might come as a surprise, but bear in mind that ideas introduced by Euclid, Maxwell or Kelvin were strongly based on geometric concepts. Therefore, before entering in the discrete/numerical world, one must first understand the inherent structures, i.e. *the geometric background* upon which physics is build [6]. An astonishing observation is the realization that different physical theories share a common structure. This translates the common engineer feeling that concepts from electromagnetism can be easily transfered for fluid mechanics, for instance.

Furthermore, many concepts from differential geometry have a direct discrete representation. Unfortunately this is not true for all operators. For example, the operator that generalizes convection, the Lie derivative, does not have a one-to-one correspondence in the discrete world of algebraic topology and some numerical modeling needs to be applied. On this chapter concepts from this continuous representation will be introduced in a intuitive manner for a more formal introductions see [8, 9, 24, 25, 26].

First of all, in Section 3-1 the use of geometric ideas as modeling tool is introduced. The aim is connect with physics with a geometric representation. Afterwards, in Section 3-2 the connection between different objects is established by action of differential geometry and it main operators are explained.

3-1 Geometric modeling

It is common to understand the world as a 4-dimensional shape. This is inherently a geometric view. This representation goes back to the “Father of Geometry”, Euclid. In his work Euclid modeled physical phenomena using simple, geometric descriptions that reveal symmetries and experimental invariants, e.g mass conservation. This approach has been the foundation of many physical theories. Unfortunately, vectorial or tensorial notations, i.e. the use of a coordinate systems in which the equations are expressed, keeps the geometric nature of this theories under the hood.

Furthermore, it is possible to distinguish between two types of physical variables, global and local. Global quantities are the ones that are actually measured, therefore are associated with space-time domains -e.g. mass. Local variables - e.g. density - are derived quantities and it is natural to associate them to the oriented geometric object of the corresponding global variable. Reviewing the previous example, consider the mass of an object,

$$m = \int_V \rho dv, \tag{3-1}$$

in here m represents the global variable and ρdv the local quantity with the respective oriented object associated. Standard vector calculus does not allow this association to be represented [27].

In every physical theory quantities are related to the most basic geometric objects. Moreover, it is necessary to orient these objects. There are two kinds of orientations, inner and outer. The first one is related only with the geometric object itself and the second one relates the geometric object and the embedding space.

In this spirit [6] established various derivations for different physical theories. The importance of this approach and its advantages have been widely recognized in the field of electromagnetism, [7] where the main quantities of interest are best described as forms. Table 3-1 summarizes some of this association.

Table 3-1: Forms used in Electromagnetism

Quantity	Unit	Dimension
Electric Potential (ϕ)	V	0
Electric Flux ($\mathbf{D}$)	V/m	1
Magnetic Field ($\mathbf{B}$)	$(V \cdot s)/m^2$	2
Charge Density (q)	A/m^3	3

Each variable is associated with a different dimensional unit. A common example to prove the strength of this formulation is to define work. Consider a charge moving from point x to point $x + v(x)$, the energy transfered by the electric field, $\mathbf{E}$, is proportional to the displacement, $v(x)$. In a geometric interpretation, the value $\mathbf{E}$ should be a linear functional on the tangent space at x, as it will be shown in the next section this corresponds to a 1-form.

3-2 Differential Geometry

Previously, it was argued that vector calculus obscures the geometric nature of physical models. Thus, it is necessary to introduce a new language that allows to re-express physical theories in a way that the connection with geometry is not lost. Differential geometry has proven to be a natural language for electromagnetism, Hamiltonian mechanics, thermodynamics, etc [8, 9, 26, 28, 29].

This concise and consistent formalism allows to express differential and integral equations on smooth and curved space, while revealing geometric invariants [30]. The integration of differential forms is an abstraction of the measurement and as it will be shown the calculus by differential forms provides and intrinsic, coordinate-free approach to different physical problems [31]. The awareness that different physical quantities are associated with different geometric notions, therefore, have different properties is crucial. As mentioned before, different fields must be associated with different geometric objects, for example temperature with a point or mass density with a volume.

3-2-1 Differential forms

Lets start by considering a line integral along a curve from A to B. Its is known that if the integration is reversed, i.e. from B to A the integral value changes to its negative

$$\int_A^B f(\mathbf{x})dl = -\int_B^A f(\mathbf{x})dl. \tag{3-2}$$

Same principle occurs in oriented surface integrals if the direction of the normal is reversed,

$$\iint \mathbf{F}\cdot\mathbf{n}dS, \tag{3-3}$$

the normal can be thought as the cross product of two basis vectors within the surface. Function on the order by which the cross product between the two basis vectors is done the sign to the normal, $\mathbf{n}$, is assigned.

If an antisymmetric product - *wedge* product $\wedge$ - is introduced, such that the cross product between the basis vectors is given by,

$$dx \wedge dy = -dy \wedge dx. \tag{3-4}$$

This automatically gives the right orientation to the surface. Similarly, the volume element can be written as,

$$dV = dx \wedge dy \wedge dz, \tag{3-5}$$

which will automatically encode orientation, i.e. if any pair of these basis forms are changed the sign changes. Furthermore,

$$dx \wedge dx = dy \wedge dy = dz \wedge dz = 0.$$

At this point, this concept can be extended to the full integrand,

$$\alpha^1 = A_x dx + A_y dy + A_z dz, \tag{3-6}$$

this object is called a 1-form. A summary of the available k-forms in $\mathbb{R}^3$ and their respective connection with geometry is summarized in Table 3-2.

Table 3-2: Forms available in $\mathbb{R}^3$

0-form	$\alpha^0 = A(x,y,z)$	$\mathcal{M}^n$	Points
1-form	$\alpha^1 = A(x,y,z)dx + B(x,y,z)dy + C(x,y,z)dz$		Lines
2-form	$\alpha^2 = A(x,y,z)dydz + B(x,y,z)dzdx + C(x,y,z)dxdy$		Surfaces
3-form	$\alpha^3 = A(x,y,z)dxdydz$		Volumes

Clearly, differential forms come in different flavors. A 1-form can be integrated over a 1D-manifold, $\mathcal{M}^1$, i.e a smooth curve,

$$\int_{\mathcal{M}^1} \alpha^1 = \int_{\mathcal{M}^1} A(x,y,z)dx + B(x,y,z)dy + C(x,y,z)dz. \tag{3-7}$$

Table 3-3 summarizes the equivalent duality pairing for all forms in $\mathbb{R}^3$. Functions, line, surface and volume elements are called $0, 1, 2$ and 3-forms, respectively. The main difference to standard vector calculus is that not only the *vector proxies*, $A(x,y,z)$, $B(x,y,z)$ and $C(x,y,z)$, are taken into account but also the basis forms, dx, dy and dz. The basis forms in the object indicates the type of form.

Table 3-3: Duality paring for k-forms in $\mathbb{R}^3$

0-form	$\langle \alpha^0, \mathcal{M}^0 \rangle = \alpha(\mathcal{M}^0)$
1-form	$\langle \alpha^1, \mathcal{M}^1 \rangle = \int_{\mathcal{M}^1} \alpha^1$
2-form	$\langle \alpha^2, \mathcal{M}^2 \rangle = \int_{\mathcal{M}^2} \alpha^2$
3-form	$\langle \alpha^3, \mathcal{M}^3 \rangle = \int_{\mathcal{M}^3} \alpha^3$

A more formal definition for differential forms is that they are anti-symmetric k-tensors acting on vectors in the tangent space to a manifold, $T_{\mathbf{x}}\mathbb{R}^n$. Translating this to a more engineering approach, k-forms are the objects found “underneath“ the integral sign. They are of extreme importance because of their ability to capture the geometric nature of the local quantities.

Addition and subtraction of differential forms are exactly as expected,

$$\begin{aligned}\alpha^1 &= A_1(x,y,z)dx;\\ \beta^1 &= A_2(x,y,z)dx + B_2(x,y,z)dy;\\ \alpha^1+\beta^1 &= \left(A_1(x,y,z)+A_2(x,y,z)\right)dx + B_2(x,y,z)dy.\end{aligned} \tag{3-8}$$

Table 3-4 summarizes common examples of the connection between k-forms and physical variables. It is clear that the physics has inherently a geometric character.

Table 3-4: Example of physical variables associated with k-forms

Temperature	$\alpha^0 = T(x,y,z)$
Velocity	$\alpha^1 = u(x,y,z)dx + v(x,y,z)dy + w(x,y,z)dz$
Vorticity	$\alpha^2 = w_z(x,y,z)dxdy + w_y(x,y,z)dzdx + w_x(x,y,z)dydz$
Density	$\alpha^3 = \rho(x,y,z)dxdydz$

3-2-2 The wedge product between forms

The wedge product is a product between k-forms and l-forms and the result is a $(k+l)$-form. Let the space of k-forms in Ω be denoted by $\Lambda^k(\Omega)$ and the space of l-forms be given by $\Lambda^l(\Omega)$,

$$\wedge \quad : \quad \Lambda^k(\Omega)\times\Lambda^l(\Omega)\to\Lambda^{k+l}(\Omega) \tag{3-9}$$

The wedge product, $\wedge$, as the following properties:

- Associative: $(a\wedge b)\wedge c = a\wedge(b\wedge c)$;
- Multi-linear: $(\alpha a+\beta b)\wedge(\gamma c+\delta d) = \alpha\gamma(a\wedge c)+\alpha\delta(a\wedge d)+\beta\gamma(b\wedge c)+\beta\delta(b\wedge d)$;
- Anti-symmetry: $a\wedge b = (-1)^{kl} b\wedge a$.

Consider the following examples of the action of the wedge product,

$$\begin{aligned}\alpha^1 &= Adx\\ \beta^2 &= Bdy\wedge dz.\end{aligned} \tag{3-10}$$

Then the wedge product is,

$$\begin{aligned}\alpha^1\wedge\beta^2 &= (Adx)\wedge(Bdy\wedge dz)\\ &= ABdx\wedge dy\wedge dz\\ &= (Bdy\wedge dz)\wedge(Adx)\\ &= \beta^2\wedge\alpha^1.\end{aligned} \tag{3-11}$$

However, considering two 1-forms,

$$\begin{aligned} \alpha^1 &= Adx \\ \beta^1 &= Bdy + Cdz, \end{aligned} \tag{3-12}$$

then the wedge is given by,

$$\begin{aligned} \alpha^1 \wedge \beta^1 &= (Adx) \wedge (Bdy + Cdz,) \\ &= ABdx \wedge dy + ACdx \wedge dz \\ &= -Bdy \wedge Adx - Cdz \wedge Adx \\ &= -\beta^1 \wedge \alpha^1. \end{aligned} \tag{3-13}$$

It can be shown that the wedge product of a 1-form, in $\mathbb{R}^3$, behaves just like the cross product in vector calculus. Consider the following example,

$$\begin{aligned} \alpha^1 &= a_1dx + a_2dy + a_3dz; \\ \beta^1 &= b_1dx + b_2dy + b_3dz; \\ \alpha^1 \wedge \beta^1 &= (a_1dx + a_2dy + a_3dz) \wedge (b_1dx + b_2dy + b_3dz) \\ &= (a_1b_2 - a_2b_1)dx \wedge dy + (a_1b_3 - a_3b_1)dx \wedge dz + (a_2b_3 - a_3b_2)dy \wedge dz. \end{aligned} \tag{3-14}$$

The coefficients are the same that would appear in a vector cross product of α and β. The advantage of using differential forms is that the metric dependence, i.e the orthogonality between vectors, does not emerge when using the wedge product. Furthermore, the wedge product generalizes the cross product to $\mathbb{R}^n$. It is common practice to rewrite $dx \wedge dy$ simply as $dxdy$.

Other example is the volume of a parallelepiped spanned by the vector a, b and c that can be determined,

$$\begin{aligned} \gamma^1 &= c_1dx + c_2dy + c_3dz; \\ \alpha^1 \wedge \beta^1 \wedge \gamma^1 &= (a_1dx + a_2dy + a_3dz) \wedge (b_1dx + b_2dy + b_3dz) \wedge (c_1dx + c_2dy + c_3dz) \\ &= (a_1b_2c_3 - a_3b_2c_1 + a_2b_3c_1 - a_3b_1c_2 + a_2b_3c_2 - a_2b_1c_3)dx \wedge dy \wedge dz. \end{aligned} \tag{3-15}$$

3-2-3 Exterior derivative

The exterior derivative is a generalization of the differential of a function. It maps k-forms to $(k+1)$-forms.

$$d \quad : \quad \Lambda^k(\Omega) \rightarrow \Lambda^{k+1}(\Omega) \tag{3-16}$$

The exterior derivative has the following properties

- Leibniz's rule: $d(a \wedge b) = da \wedge b + (-1)^k a \wedge db$;
- $d \circ d = 0$.

Let α^0 be a 0-form given by $\alpha^0 = A(x, y, z)$. Then the exterior derivative, $d\alpha^0$ is given by

$$d\alpha^0 = \frac{\partial A}{\partial x}dx + \frac{\partial A}{\partial y}dy + \frac{\partial A}{\partial z}dz. \tag{3-17}$$

The vector proxy of the 1-form, $d\alpha^0$, resembles the gradient in vector calculus. The physical meaning, for example α^0 is a temperature representation, computing $d\alpha^0$ corresponds to determining the temperature gradient.

Consider, the 1-form, $\alpha^1 = A(x.y, z)dx + B(x, y, z)dy + C(x, y, z)dz$, the exterior derivative is given by

$$d\alpha^1 = \left(\frac{\partial C}{\partial y} - \frac{\partial B}{\partial z}\right)dydz + \left(\frac{\partial A}{\partial z} + \frac{\partial C}{\partial x}\right)dzdx + \left(\frac{\partial B}{\partial x} - \frac{\partial A}{\partial y}\right)dxdy. \tag{3-18}$$

Again, the vector proxy of the 2-form, $d\alpha^1$, resembles the rotational operation from vector calculus, $\nabla\times$.

At last, applying the exterior derivative to the 2-form, $\alpha^2 = A(x, y, z)dydz + B(x, y, z)dzdx + C(x, y, z)dxdy$,

$$d\alpha^2 = \left(\frac{\partial A}{\partial x} + \frac{\partial B}{\partial y} + \frac{\partial C}{\partial x}\right)dxdydz. \tag{3-19}$$

The vector proxy of the 3-form, $d\alpha^2$, corresponds to the divergence, $\nabla\cdot$. Table 3-5 summarizes the action of the exterior derivative for different k-forms in $\mathbb{R}^3$.

Table 3-5: Relation between the exterior derivative and vector calculus operations

$d\alpha^0$	Gradient: ∇
$d\alpha^1$	Curl: $\nabla\times$
$d\alpha^2$	Divergence: $\nabla\cdot$

It should be clear now that the fact that $d\,(d\alpha) = 0$ translates the identities $curl \circ grad = 0$ and $div \circ grad = 0$.

$$\begin{tikzcd} \mathbb{R} \arrow[r] & \Lambda^0(\Omega) \arrow[r, "d", "\nabla"'] & \Lambda^1(\Omega) \arrow[r, "d", "\nabla\times"'] & \Lambda^2(\Omega) \arrow[r, "d", "\nabla\cdot"'] & \Lambda^3(\Omega) \arrow[r, "d"] & 0 \end{tikzcd} \tag{3-20}$$

3-2-4 Transformation

A transformation of a k-form, α^k can be written using the so-called pullback operator. Suppose there is a mapping defined by, $\phi : (x, y, z) \to (u, v, w)$, a differential form, α^k given in terms of (u, v, w) integrated in a manifold, $\mathcal{M}$, then

$$\int_{\phi(\mathcal{M}^k)} \alpha^k = \int_{\mathcal{M}^k} \phi^\star \alpha^k. \tag{3-21}$$

Equivalently,

$$\left\langle \phi(\mathcal{M}^k), \alpha^k \right\rangle = \left\langle \mathcal{M}^k, \phi^\star \alpha^k \right\rangle. \tag{3-22}$$

Therefore, the pullback operator takes a k-form defined in (u, v, w) to a k-form defined in (x, y, z), i.e. $\phi^\star : \Lambda^k(\Omega) \to \Lambda^k(\Omega')$. The pullback commutes both with the wedge product and the exterior derivative,

- $\phi^\star d\alpha^k = d\phi^\star \alpha^k$;
- $\phi^\star \left(\alpha^k \wedge \beta^l\right) = \left(\phi^\star \alpha^k\right) \wedge \left(\phi^\star \beta^l\right)$.

Table 3-6: Pull-back action on k-forms in $\mathbb{R}^3$

$\alpha^0 = f(\mathbf{y})$	$\phi^\star \alpha^0 = f(\phi(\mathbf{x}))$
$\alpha^1 = \sum\limits_{i=1}^{3} f_i(\mathbf{y}) dy^i$	$\phi^\star \alpha^1 = \sum\limits_{j=1}^{3} \sum\limits_{i=1}^{3} f_i(\phi(\mathbf{x})) \frac{\partial \phi^i}{\partial x^j} dx^j$
$\alpha^2 = \sum\limits_{1 \leq i < j \leq 3} f_{ij}(\mathbf{y}) dy^i \wedge dy^j$	$\phi^\star \alpha^2 = \sum\limits_{1 \leq k < l \leq n} \sum\limits_{1 \leq i < j \leq m} f_{ij}(\phi(\mathbf{x})) det \begin{pmatrix} \frac{\partial \phi^i}{\partial x^k} & \frac{\partial \phi^i}{\partial x^l} \\ \frac{\partial \phi^j}{\partial x^k} & \frac{\partial \phi^j}{\partial x^l} \end{pmatrix} dx^k \wedge dx^l$
$\alpha^3 = f(\mathbf{y}) dy^1 \wedge dy^2 \wedge dy^3$	$\phi^\star \alpha^3 = f(\phi(\mathbf{x})) det \begin{pmatrix} \frac{\partial \phi^1}{\partial x^1} & \frac{\partial \phi^1}{\partial x^2} & \frac{\partial \phi^1}{\partial x^3} \\ \frac{\partial \phi^2}{\partial x^1} & \frac{\partial \phi^2}{\partial x^2} & \frac{\partial \phi^2}{\partial x^3} \\ \frac{\partial \phi^3}{\partial x^1} & \frac{\partial \phi^3}{\partial x^2} & \frac{\partial \phi^3}{\partial x^3} \end{pmatrix} dx^1 \wedge dx^2 \wedge dx^3$

The use of a parametric map allows to differentiate and integrate without need of metric information. A common example is the computation of the work required to move a charge through an electric field. Let the electric field intensity be given by, $E^1 = 2xydx + x^2dy - dz$. A charge of $q = 1C$ is transported over the path P given by ($x = t^2$, $y = t$, $z = 1 - t^3$) from $t = 0$ to $t = 1$. The work required is given by,

$$\begin{aligned} W &= -q \int_P 2xydx + x^2dy - dz \\ &= -q \int\limits_{t=0}^{t=1} P^\star E, \end{aligned} \tag{3-23}$$

Table 3-7: Connection between the integral theorems in vector calculus and differential geometry

0-Forms	$\int_{\mathcal{M}^1} d\alpha^0 = \alpha^0(b) - \alpha^0(a)$	Stokes	$\int_{\mathcal{M}^1} \nabla\psi \cdot d\overrightarrow{s} = \psi(b) - \psi(a)$
1-Forms	$\int_{\mathcal{M}^2} d\alpha^1 = \int_{\partial\mathcal{M}^2} \alpha^1$	Kelvin-Stokes	$\int_{\mathcal{M}^2} \left(\nabla \times \overrightarrow{A}\right) \cdot \overrightarrow{n} dS = \int_{\partial\mathcal{M}^2} \overrightarrow{A} \cdot d\overrightarrow{s}$
2-Forms	$\int_{\mathcal{M}^3} d\alpha^2 = \int_{\partial\mathcal{M}^3} \alpha^2$	Gauss	$\int_{\mathcal{M}^3} \left(\nabla \cdot \overrightarrow{A}\right) dV = \int_{\partial\mathcal{M}^3} \overrightarrow{A} \cdot \overrightarrow{n} dS$

where $P^{\star}E$ is the pullback of the field 1-form to the path P,

$$\begin{aligned} P^{\star}E &= 2(t^2)(t)2tdt + (t^2)^2dt - (-3t^2)dt \\ &= (5t^4 + 3t^2)dt. \end{aligned} \tag{3-24}$$

Integrating this 1-form in t over the interval $[0, 1]$,

$$W = -\int_{t=0}^{t=1} (5t^4 + 3t^2)dt = -2J, \tag{3-25}$$

this is the total work required to move the charge along P.

3-2-5 Generalized Stokes theorem

Differential forms are natural objects to be integrated over a k-dimensional manifold. As shown in the previous sections the vector operations, **grad**, **curl** and **div** can be generalized depending on the space Λ^k where the exterior derivative, d, acts. Therefore, the integral theorems from vector calculus, i.e. Stokes, Kelvin-Stokes and Gauss can also be re-interpreted.

Consider a k-form α^k and an $k + 1$-manifold, $\mathcal{M}^{k+1}$ with boundary $\partial\mathcal{M}^k$, the generalized Stokes theorem is given by

$$\int_{\mathcal{M}^{k+1}} d\alpha^k = \int_{\partial\mathcal{M}^{k+1}} \alpha^k \tag{3-26}$$

Table 3-7 together with Figure 3-1 summarize the connection between the integral theorems in vector calculus and differential geometry.

The integration can also be seen as the duality pairing between a k-form and a k-manifold. Thus, the generalized Stokes theorem can be written as

$$\left\langle d\alpha^{(k-1)}, \mathcal{M}^k \right\rangle = \left\langle \alpha^{(k-1)}, \partial\mathcal{M}^k \right\rangle \tag{3-27}$$

This representation highlights that the exterior derivative, d, is the formal adjoint of the boundary operator ∂.

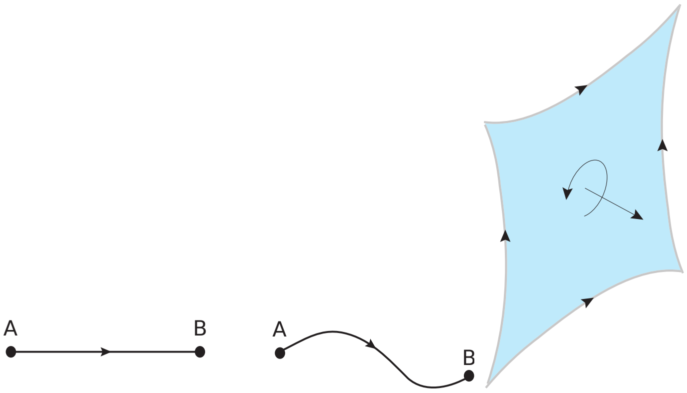

(a) Stokes

(b) Kelvin-Stokes

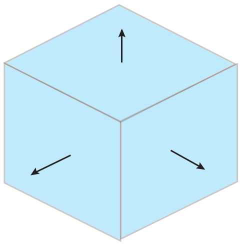

(c) Gauss

Figure 3-1: Geometric interpretation of the generalized Stokes theorem

3-2-6 Hodge-$\star$

Lets return to the Poisson equation $\Delta\phi = f$. In terms of differential geometry, it was already shown that **div** corresponds to the action of the exterior derivative in 2-forms, thus

$$d\alpha^2 = f^3 \tag{3-28}$$

The action of the exterior derivative in 0-forms corresponds to action of the **grad**, thus

$$d\alpha^0 = \beta^1 \tag{3-29}$$

The assumptions done in Chapter 1 Section 1-1, are clearly wrong, because, $\beta^1 \neq \alpha^2$. Between (3-28) and (3-29) there is link missing that connects both equations. It is necessary to create an operator that changes the geometric object. Lets define the Hodge-$\star$ operator, which maps k-forms onto $(n-k)$-forms, where n is the dimension of the ambient space. This operator is based in the inner product. Consider a manifold, $\mathcal{M}$, the inner product $\langle\cdot,\cdot\rangle$ be defined by

$$\langle\alpha,\beta\rangle := \int_{\mathcal{M}} \alpha\wedge\star\beta. \tag{3-30}$$

It should be clear that the Hodge-$\star$ does not alter the scalar field or vector field but changes the orientation of the geometric object where this field acts,

$$\alpha^1 = u(x,y,z)dx + v(x,y,z)dy + w(x,y,z)dz; \tag{3-31}$$
$$\star\alpha^1 = u(x,y,z)dydz + v(x,y,z)dzdx + w(x,y,z)dxdy. \tag{3-32}$$

This operator is a crucial operation in differential geometry and much attention has been devoted to it [32].

Some examples of the action of the Hodge-$\star$,

$$\begin{aligned} \star 1 = dxdydz, \quad \star dxdydz = 1, \\ \star dx = dydz, \quad \star dy = dzdx, \quad \star dz = dxdy \\ \star(dydz) = dx, \quad \star(dzdx) = dy, \quad \star(dxdy) = dz. \end{aligned} \tag{3-33}$$

3-2-7 de Rham complex

It became clear in the previous sections that the exterior derivative maps k-forms to $(k+1)$-forms while the Hodge-$\star$ changes the orientation of the k-form. Hence, it becomes possible to build a sequence called the double deRham Complex.

$$\begin{tikzcd}
\mathbb{R} \arrow[r] & \Lambda^0(\Omega) \arrow[r, "d", "Grad"'] \arrow[d, leftrightarrow, "\star"] & \Lambda^1(\Omega) \arrow[r, "d", "Curl"'] \arrow[d, leftrightarrow, "\star"] & \Lambda^2(\Omega) \arrow[r, "d", "Div"'] \arrow[d, leftrightarrow, "\star"] & \Lambda^3(\Omega) \arrow[r, "d"] \arrow[d, leftrightarrow, "\star"] & 0 \\
0 & \widetilde{\Lambda}^3(\Omega) \arrow[l, "d"'] & \widetilde{\Lambda}^2(\Omega) \arrow[l, "d"', "Div"] & \widetilde{\Lambda}^1(\Omega) \arrow[l, "d"', "Curl"] & \widetilde{\Lambda}^0(\Omega) \arrow[l, "d"', "Grad"] & \mathbb{R} \arrow[l]
\end{tikzcd} \tag{3-34}$$

The exactness of this differential complex plays an important role in the design and stability of numerical methods for PDE [33]. In computational electromagnetism this has been widely used, [7, 32].

3-2-8 Codifferential

In contrast to the exterior derivative, the operator $d^\star$ maps a k-form to a $(k-1)$-form. The coderivative is given by

$$d^\star := (-1)^{n(k+1)+1} \star d \star \tag{3-35}$$

For the codifferential also holds $d^\star \circ d^\star = 0$.

3-2-9 Laplace-deRham

Lets define a new operator that generalizes the Laplacian operator. This operator maps k-forms into k-forms defined as

$$\Delta = (d + d^\star)^2 = d \circ d^\star + d^\star \circ d \tag{3-36}$$

The Laplace-deRham operator has the following properties

- Self-adjoint: $\langle \Delta\alpha, \beta \rangle = \langle \alpha, \Delta\beta \rangle$;
- Non negative: $\langle \Delta\alpha, \alpha \rangle \geq 0$;
- $\Delta\alpha = 0$ if and only if $d\alpha = 0$ and $d^\star\alpha = 0$.

Table 3-8 summarizes the action of the Laplace-deRham operator in k-forms. An example of a physical application of this operator is in the modeling of diffusion.

Table 3-8: Action of the Laplace-deRham onto forms in $\mathbb{R}^2$

0-forms	$\Delta\alpha^0 = d^\star d\alpha^0$
1-forms	$\Delta\alpha^1 = d^\star d\alpha^1 + dd^\star\alpha^1$
2-forms	$\Delta\alpha^2 = dd^\star\alpha^2$

3-2-10 Connection between forms and vector fields

Operators such as the flat, $\flat$, and the sharp, $\sharp$, are important because they allow to connect vector fields with differential forms. First define the $\flat$,

$$\flat \quad : \quad \mathbf{v}(\Omega) \rightarrow \Lambda^1(\Omega) \tag{3-37}$$

The inverse is given by the $\sharp$,

$$\sharp \quad : \quad \Lambda^1(\Omega) \rightarrow \mathbf{v}(\Omega) \tag{3-38}$$

The sharp and the flat operator connect as,

$$\sharp \circ \flat = \flat \circ \sharp = 1. \tag{3-39}$$

Examples of the action of the, $\sharp$ and $\flat$ are,

$$\begin{array}{ll} \sharp dx = \frac{\partial}{\partial x}, & \flat \frac{\partial}{\partial x} = dx, \\ \sharp dy = \frac{\partial}{\partial y}, & \flat \frac{\partial}{\partial y} = dy. \end{array}$$

3-2-11 Interior product & Extrusion

As described in [34] the interior product is the removing of the surfaces of the first form from the those of the second one. The interior product $\iota_{dx}dy = 0$ since there are no dx surface to remove from dy. On the other hand, the $\iota_{dx}dx = 1$. This operator allows a combination between vector fields and differential forms. If $\mathbf{v}$ is a vector and α is a k-form, their interior product or contraction,

$$\iota_v \quad : \quad \Lambda^{k+1}(\Omega) \to \Lambda^k(\Omega) \tag{3-40}$$

given by

$$\iota_v\alpha(v_1, \dots, v_k) = \alpha(v, v_1, \dots, v_k). \tag{3-41}$$

Thus, this operator does not depend on the metric. Furthermore, for smooth manifolds, [11] proves that interior product can also be defined as

$$\iota_v\alpha = (-1)^{k(n-k)} \star (\star\alpha \wedge v^\flat). \tag{3-42}$$

The properties of the interior product are:

- $\iota_{A+B} = \iota_A + \iota_B$;
- $\iota_{aA} = a\iota_A$;
- $\iota_v(\alpha^p \wedge \beta^q) = [\iota_v\alpha^p] \wedge \beta^q + (-1)^p\alpha^p \wedge [\iota_v\beta^q]$;
- $\iota_v(\alpha^j \wedge \star\beta^k) = \iota_v\alpha^j \wedge \star\beta^k + (-1)^{j+k}\alpha^j \wedge (-1)^k\iota_v \star \beta^k$.

The interior product of arbitrary 1-forms can be found by linearity from the following relationships,

$$\begin{array}{lll}
\iota_{\frac{\partial}{\partial x}} dx = 1 & \iota_{\frac{\partial}{\partial x}} dy = 0 & \iota_{\frac{\partial}{\partial x}} dz = 0 \\
\iota_{\frac{\partial}{\partial y}} dx = 0 & \iota_{\frac{\partial}{\partial y}} dy = 1 & \iota_{\frac{\partial}{\partial y}} dx = 0 \\
\iota_{\frac{\partial}{\partial z}} dx = 0 & \iota_{\frac{\partial}{\partial z}} dy = 0 & \iota_{\frac{\partial}{\partial x}} dy = 1
\end{array}$$

The interior product of a 1-form and a 2-form can be found

$$\begin{array}{ccc}
\iota_{\frac{\partial}{\partial x}} dy \wedge dz = 0 & \iota_{\frac{\partial}{\partial x}} dz \wedge dx = -dz & \iota_{\frac{\partial}{\partial x}} dx \wedge dy = dy \\
\iota_{\frac{\partial}{\partial y}} dy \wedge dz = dz & \iota_{\frac{\partial}{\partial y}} dz \wedge dx = 0 & \iota_{\frac{\partial}{\partial y}} dx \wedge dy = -dx \\
\iota_{\frac{\partial}{\partial z}} dy \wedge dz = -dy & \iota_{\frac{\partial}{\partial z}} dz \wedge dx = dx & \iota_{\frac{\partial}{\partial z}} dx \wedge dy = 0
\end{array}$$

On the other hand, the dual concept to the interior product is the extrusion operator [35]. Figure 3-2 represents a geometric interpretation of extrusion. Imagine that 1-manifold, $\mathcal{M}^1$ being transported by the flow, $\mathbf{v}$, from time t_0 to t_1. The resultant 2-manifold is then a surface, $\mathcal{M}^2_{Ext}$.

The connection between the interior product and the extrusion is established by,

$$\int_\Omega \iota_X\alpha = \left.\frac{d}{dt}\right|_{t=0} \int_{Ext(\Omega,t)} \alpha \tag{3-43}$$

$$\int_0^{\Delta t} \left[\int_{\Omega(t)} \iota_X\alpha\right] dt = \int_{Ext(\Omega,t)} \alpha \tag{3-44}$$

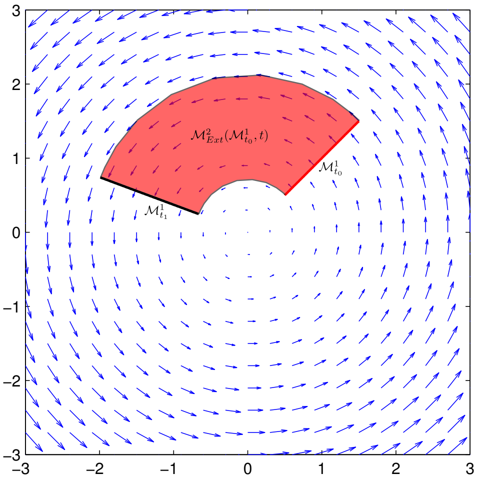

Figure 3-2: Geometric interpretation of the extrusion concept

3-2-12 Lie Derivative

The Lie derivative, also called by Arnold [36] as the Fisherman derivative, i.e. *the flow carries all possible differential-geometric objects past the fisherman, and the fisherman, sits there and differentiates them.* The Lie derivative is a representation of the convective part of the flow, a directional derivative.

The interior product operator together with the exterior derivative forms the Lie derivative, by means of Cartan's magic formula,

$$\pounds_X := \iota_X \circ d + d \circ \iota_X. \tag{3-45}$$

The properties of the Lie derivative are:

- Leibniz rule: $\pounds_X(\alpha^p \wedge \beta^q) = (\pounds_X \alpha^p) \wedge \beta^q + \alpha^p \wedge (\pounds_X \beta^q)$;
- $\iota_X d\alpha^0 = \pounds_X \alpha^0$;
- d $\iota_X \alpha^n = \pounds_X \alpha^n$;
- $\pounds_{fX} \alpha^p = f \pounds_X \alpha^p + df \wedge \iota_X \alpha^p$.

It is easy to show that the Lie derivative commutes with the exterior derivative,

$$d\pounds_{\mathbf{v}}\alpha^k = d\left(\iota_{\mathbf{v}} d\alpha^k + d\iota_{\mathbf{v}}\alpha^k\right) = d\iota_{\mathbf{v}} d\alpha^k = \left(d\iota_{\mathbf{v}} + \iota_{\mathbf{v}} d\right) d\alpha^k = \pounds_{\mathbf{v}} d\alpha^k. \tag{3-46}$$

This can be summarized in the following commuting diagram,

$$\begin{tikzcd}
\Lambda^k(\Omega) \arrow[r, "d"] \arrow[d, "\pounds_{\mathbf{v}}"] & \Lambda^{k+1}(\Omega) \arrow[d, "\pounds_{\mathbf{v}}"] \\
\Lambda^k(\Omega) \arrow[r, "d"] & \Lambda^{k+1}(\Omega)
\end{tikzcd} \tag{3-47}$$

The consequence of this commutation is that the advection of a closed form, i.e. $d\alpha^k = 0$, remains closed. The concept of closed form is deeply connected to the concept of conservative force in physics. For example in the case of a scalar field α^0 the advection of the correspondent gradient field, i.e. $d\alpha^0 = \beta^1$ is given by,

$$\pounds_{\mathbf{v}}\beta^1 = d\pounds_{\mathbf{v}}\alpha^0, \tag{3-48}$$

where the left hand side correspond to the advection of the gradient field itself and the right hand side the advection of scalar field and then differentiated. However, both sides of the equation lead to a gradient field.

On the other hand, the Lie derivative can also be defined in a more dynamic way,

$$\pounds_{\mathbf{v}}\alpha^k = \left.\frac{d}{dt}\right|_{t=0}\int_{\Omega_t}\alpha^k = \left.\frac{d}{dt}\right|_{t=0}\Phi_t^{\star}\alpha^k. \tag{3-49}$$

For example, consider the vector field X,

$$X = v^1(x,y)\frac{\partial}{\partial x^1} + v^2(x,y)\frac{\partial}{\partial x^2}.$$

It is possible to construct a 1-parameter family of maps, ϕ_t, that takes the molecule located at p when t=0 to the position of the same molecule at t seconds later.

$$\begin{aligned}\frac{dx^1}{dt} &= v^1(x^1(t), x^2(t));\\ \frac{dx^2}{dt} &= v^2(x^1(t), x^2(t)).\end{aligned}$$

For example, let's consider the $\pounds_X vol^n$. In this case, the Lie derivative measures how volumes are changing under the flow generated by X. Figure 3-3 represents the advection of a 2-form by a divergence free velocity field and in this case the area of the surface is kept constant.

A more concrete example of the action of the Lie derivative is if a vector field, $\mathbf{v} =< x, y >$ that gives a flow $\Phi_t(x,y) = (e^t x, e^t y)$ acts on a 1-form, $\alpha^1 = (x^2+y^2)dx$. Thus

$$\begin{aligned}\left(\Phi_t^{\star}\alpha\right)(x,y) &= \left((e^t x)^2 + (e^t y)^2\right)\phi_t^{\star}dx\\ &= e^{2t}(x^2+y^2)d(x\circ\Phi_t)\\ &= e^{2t}(x^2+y^2)(e^t dx)\\ &= e^{3t}\alpha^1\end{aligned} \tag{3-50}$$

Thus,

$$\pounds_{\mathbf{v}}\alpha^1 = \left.\frac{d}{dt}\right|_{t=0} e^{3t}\alpha^1 = 3\alpha^1 \tag{3-51}$$

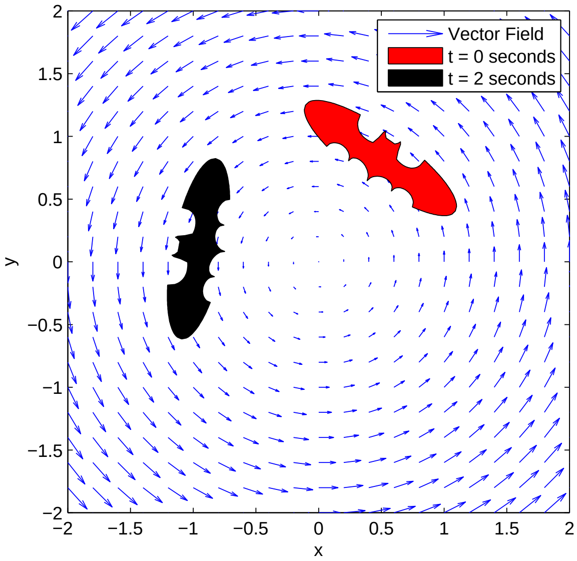

Figure 3-3: Advection of a 2-form by a divergence-free vector field

This can also be confirmed by the algebraic approach,

$$\begin{aligned} d\alpha^1 &= -2ydxdy \\ \iota_{\mathbf{v}} d\alpha^1 &= (-1)^{2(2-2)} \star \left(\star d\alpha^1 \wedge \mathbf{v}^\flat\right) \\ &= \star\left(-2y \wedge (xdx + ydy)\right) \\ &= \star\left(-2yxdx - 2y^2dy\right) \\ &= -2yxdy + 2y^2dx \end{aligned} \tag{3-52}$$

$$\begin{aligned} \iota_{\mathbf{v}} \alpha^1 &= (-1)^{1(2-1)} \star \left(\star\alpha^1 \wedge \mathbf{v}^f lat\right) \\ &= -\star\left((x^2+y^2)dy \wedge (xdx + ydy)\right) \\ &= -\star\left(-(x^2+y^2)xdxdy\right) \\ &= (x^2+y^2)x \\ d\iota_{\mathbf{v}} \alpha^1 &= \left(3x^2 + y^2\right) dx + 2xydy \end{aligned} \tag{3-53}$$

Therefore, combining (3-52) and (3-53) the Lie derivative is given by,

$$\begin{aligned} \pounds_{\mathbf{v}} \alpha^1 &= \left(3x^2 + y^2 + 2y^2\right) dx + (2xy - 2yx)\, dy \\ \pounds_{\mathbf{v}} \alpha^1 &= 3\alpha^1 \end{aligned} \tag{3-54}$$

Obviously, both approaches lead to the same result.

Table 3-9: Algebraic and dynamic definition of the Lie derivative and the interior product

Algebraic	$\pounds_{\mathbf{v}} = \iota_{\mathbf{v}} d\alpha + d\iota_{\mathbf{v}}\alpha$	$\iota_{\mathbf{v}}\alpha = (-1)^{k(n-k)} \star (\star\alpha \wedge \mathbf{v}^{\flat})$
Dynamic	$\pounds_{\mathbf{v}}\alpha = \frac{d}{dt}\Big\vert_{t=0} \int_{\Omega_t} \alpha$	$\int_{\Omega} \iota_{\mathbf{v}}\alpha = \frac{d}{dt}\Big\vert_{t=0} \int_{Ext(\Omega,t)} \alpha$

The Lie derivative is a concept that emerges in several areas of mechanics, e.g. the rate of strain tensor in elasticity, the magnetic diffusion-advection and the vorticity advection equation in fluid dynamics. Table 3-9 summarizes both algebraic and dynamic definitions for the interior product and the Lie derivative.

Table 3-10: Connection between differential geometry operators and vector calculus in $\mathbb{R}^3$

	$d\alpha^k$	$\iota_{\mathbf{v}}\alpha^k$	$\pounds_{\mathbf{v}}\alpha^k = d\iota_{\mathbf{v}}\alpha^k + \iota_{\mathbf{v}}d\alpha^k$
0-forms	$\mathbf{grad}\alpha$		$\mathbf{v} \cdot \mathbf{grad}\alpha$
1-forms	$\mathbf{curl}\alpha$	$\mathbf{v} \cdot \alpha$	$\mathbf{grad}\,(\mathbf{v} \cdot \alpha) + \mathbf{curl}\,(\mathbf{v} \times \alpha)$
2-forms	$\mathbf{div}\alpha$	$\mathbf{v} \times \alpha$	$\mathbf{curl}\,(\mathbf{v} \times \alpha) + \mathbf{v}\mathbf{div}\alpha$
3-forms		$\mathbf{v}\alpha$	$\mathbf{div}\,(\alpha\mathbf{v})$

The action of the Lie derivative can also be summarized in the following diagram,

$$\begin{tikzcd}
\widetilde{\Lambda}^0(\Omega) & \widetilde{\Lambda}^0(\Omega) \arrow[l, dashed, "\pounds_{\mathbf{v}}"'] \arrow[r, leftrightarrow, "\star"] \arrow[dl, "d"] & \Lambda^3(\Omega) \arrow[r, dashed, "\pounds_{\mathbf{v}}"] \arrow[d, "\iota_{\mathbf{v}}"] & \Lambda^3(\Omega) \arrow[d, "\iota_{\mathbf{v}}"] \\
\widetilde{\Lambda}^1(\Omega) \arrow[u, "\iota_{\mathbf{v}}"] & \widetilde{\Lambda}^1(\Omega) \arrow[l, dashed, "\pounds_{\mathbf{v}}"'] \arrow[r, leftrightarrow, "\star"] \arrow[u, "\iota_{\mathbf{v}}"] \arrow[dl, "d"] & \Lambda^2(\Omega) \arrow[r, dashed, "\pounds_{\mathbf{v}}"] \arrow[ur, "d"] \arrow[d, "\iota_{\mathbf{v}}"] & \Lambda^2(\Omega) \arrow[d, "\iota_{\mathbf{v}}"] \\
\widetilde{\Lambda}^2(\Omega) \arrow[u, "\iota_{\mathbf{v}}"] & \widetilde{\Lambda}^2(\Omega) \arrow[l, dashed, "\pounds_{\mathbf{v}}"'] \arrow[r, leftrightarrow, "\star"] \arrow[u, "\iota_{\mathbf{v}}"] \arrow[dl, "d"] & \Lambda^1(\Omega) \arrow[r, dashed, "\pounds_{\mathbf{v}}"] \arrow[ur, "d"] \arrow[d, "\iota_{\mathbf{v}}"] & \Lambda^1(\Omega) \arrow[d, "\iota_{\mathbf{v}}"] \\
\widetilde{\Lambda}^3(\Omega) \arrow[u, "\iota_{\mathbf{v}}"] & \widetilde{\Lambda}^3(\Omega) \arrow[l, dashed, "\pounds_{\mathbf{v}}"'] \arrow[r, leftrightarrow, "\star"] \arrow[u, "\iota_{\mathbf{v}}"] & \Lambda^0(\Omega) \arrow[r, dashed, "\pounds_{\mathbf{v}}"] \arrow[ur, "d"] & \Lambda^0(\Omega)
\end{tikzcd} \tag{3-55}$$

The Lie derivative has also proven to be a key ingredient in understand symmetries [37]. This approach might be consider in future to develop a full space-time approach to the discretization of the Lie derivative.

Chapter 4

Algebraic Topology - The discrete world of differential forms

Finding a proper discrete notion to differential forms is a crucial step. If the differential forms were approximated using their coordinate values and the exterior derivative by finite differences, the fundamental integration theorems would not hold numerically. Thus, the goal of this Chapter is to present proper discretization of differential forms. Furthermore, the geometric discretization hereafter presented as the advantage to be well suited for computational purposes.

In Chapter 3 it was mentioned that physical variables can be associated with different geometrical concepts. Thus, it is natural to search for a mathematical branch that is mainly concerned with the fundamental properties of the space. Algebraic topology is this branch. Topological concepts are inherently metric-free, i.e. the computations do not depend on norm, angles, inner-product, etc. Specifically, the concepts of chain and cochain from algebraic topology can be used to mimic differential geometry of finite grids. The collection of values on vertices, edges, surfaces and volumes are a proper discrete version of pointwise functions, line, surface and volume integrals, respectively.

First of all, in Section 4-1 a topological description of geometry for $\mathbb{R}^2$ and $\mathbb{R}^3$ is introduced, i.e. point, line, surface and volume complexes. Afterwards, in Section 4-2 the notion of chain and the boundary operator are introduced. In Section 4-3 the natural discrete equivalent of a differential form, the cochain, is introduced. It will also be shown that the exterior derivative, d, as a natural topological discrete version, the coboundary operator. Finally, in Section 4-4 de Rham complex is rewritten in terms of the discrete world. A more mathematical detailed presentation of this concepts can be found in [38, 39]

4-1 Cell Complexes

The domain of interest Ω is going to be divided into a set of discrete sub domains, cells. Consider p-cells, where $p = 0, 1, 2, 3$ for $\mathbb{R}^3$. 0-cells represent points, 1-cells represents lines, 2-cells surfaces and 3-cells volumes. Figure 4-1 represents all available cell complexes for 3D and 2D.

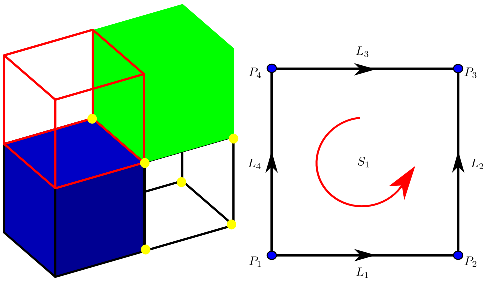

(a) 3D **(b)** 2D

Figure 4-1: Cell complex for $\mathbb{R}^3$ and $\mathbb{R}^2$

Furthermore, in order to perform operations in the cells they require a numbering and orientation. The numbering can be done freely, Figure 4-5 shows an example for a cell complex in $\mathbb{R}^2$. Analogous to the differential geometry, where forms could be associated with inner and outer oriented infinitesimal geometric objects, cells can also be associated with these two types of orientation. Figure 4-2 represents the different type of cells that can be associated with inner and outer oriented objects in 2D.

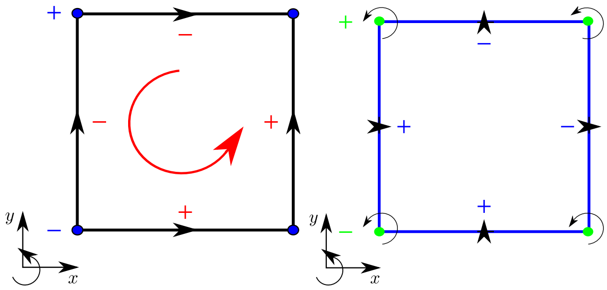

(a) Inner orientation **(b)** Outer orientation

Figure 4-2: Different orientations for the cell complex in $\mathbb{R}^2$

It is obvious if points, 0-cell, are connected a 1-cell is obtained. Moreover, a 2-cell is a surface bounded by 1-cells, obviously, a 3-cell is a volume bounded by 2-cells. Thus, it is possible to create a mesh with chains. However, it is not clear if these lines are straight, curved, self-intersection or with any other special feature. Although there is an orthogonal cell complex in Figure 4-1 and Figure 4-2 nothing change if it was highly curved for instance. The reason for this is that in topological space only the relation between objects is important.

4-2 Chains and boundary operator

If there are a finite number of cells and each is labeled with P_i, $i = 1 \cdots n_P$, the following chain can be formed,

$$C_p = \sum_{i}^{n_p} m_{p_i} c_{p_i}, \tag{4-1}$$

the weight m_{p_i} gives information about the cell orientation. If $m_{p_i} = +1$ the cell is positive oriented and if $m_{p_i} = -1$ the cell is negatively oriented with respect to the coordinate axes.

Figure 4-1 shows a 2D oriented cell-complex. Moreover, each p-chain, where $p = 0, 1, 2, 3$, forms a collection of points, lines, surfaces and volumes, respectively. As mentioned before, there is a connection between different oriented and labeled p-chains. The boundary operator, ∂ emerges naturally out of this formalism establishing this connections.

The boundary operator connects different p-chains. It maps p-chains to $(p-1)$-chains.

$$\partial \quad : \quad C_p \rightarrow C_{p-1}. \tag{4-2}$$

In $\mathbb{R}^3$ it is possible to construct the following exact sequence,

$$\begin{tikzcd} 0 & C_0 \arrow[l] & C_1 \arrow[l, "\partial"'] & C_2 \arrow[l, "\partial"'] & C_3 \arrow[l, "\partial"'] & 0 \arrow[l] \end{tikzcd} \tag{4-3}$$

In this sequence C_0 represents the set of all ordered vertices. The ordering of the vertices induces orientation in the edges C_1, the faces C_2 and the cells C_3. For example looking at the 2D oriented and labeled 1-cell complex of Figure 4-1, the following can be established,

$$\partial \begin{pmatrix} L_1 \\ L_2 \\ L_3 \\ L_4 \end{pmatrix} = \begin{pmatrix} \partial L_1 \\ \partial L_2 \\ \partial L_3 \\ \partial L_4 \end{pmatrix} = \begin{pmatrix} -1 & 1 & 0 & 0 \\ 0 & -1 & 1 & 0 \\ 0 & 0 & 1 & -1 \\ -1 & 0 & 0 & 1 \end{pmatrix} \begin{pmatrix} P_1 \\ P_2 \\ P_3 \\ P_4 \end{pmatrix} \tag{4-4}$$

Equation (4-4) shows that the boundary operator consists only in an incidence matrix, $\mathbb{E}_{(1,0)}$ (subscript indicating a change from 1-cells to 0-cells) with -1, 0 and 1 entries, reflecting if the cell as a positive or negative sense of direction.

Other example of the action of the boundary operator,

$$\partial S_1 = \mathbb{E}_{(2,1)} L_i = \begin{pmatrix} 1 & 1 & -1 & -1 \end{pmatrix} \begin{pmatrix} L_1 \\ L_2 \\ L_3 \\ L_4 \end{pmatrix}. \tag{4-5}$$

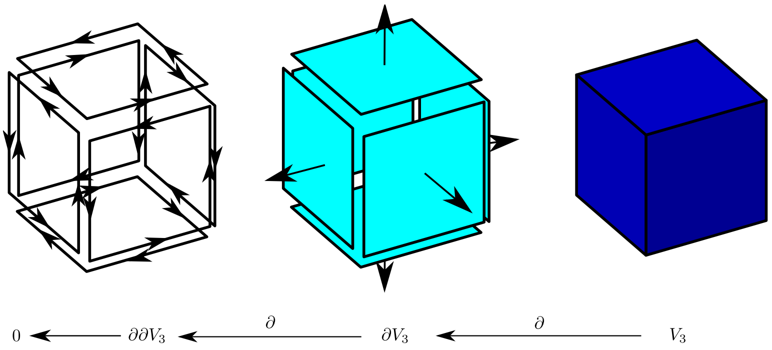
0
$\partial\partial V_3$
∂
∂V_3
∂
V_3

(a) Boundary operator in 3D

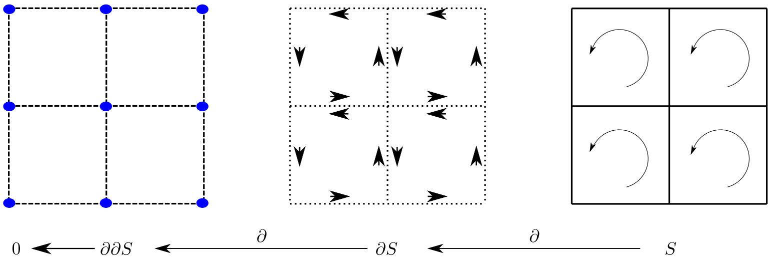
0
$\partial\partial S$
∂
∂S
∂
S

(b) Boundary operator in 2D

Figure 4-3: Boundary operator action in $\mathbb{R}^2$ and $\mathbb{R}^3$

In a more general framework,

$$\partial \sum_{i}^{n_p} m_{p_i} c_{p_i} = \sum_{i}^{n_p} m_{p_i} \partial c_{p_i}. \tag{4-6}$$

Another important property is that the boundary of the boundary is always empty,

$$\partial \circ \partial = 0 \tag{4-7}$$

Figure 4-3 represents the action of the boundary operator. It is clear that when the boundary operator acts twice opposed orientations are obtained. This is clear for the 3D case where the 1-cells, edges, are oppositely oriented. Thus, there is a cancel out of all terms.

Along Chapter 3 it was defined, through the generalized Stokes Theorem, that the exterior derivative was the formal adjoint of the boundary operator.

4-3 Cochains and coboundary operator

Consider a 1-chain, c_1, where a 1-form, α^1 is going to be integrated,

$$\int_{c_1} \alpha^1 = \sum_{i=1}^{n_l} m_i \int_{c_1^i} \alpha^1 \tag{4-8}$$

this is called 1-cochain. This is the dual of the 1-chain. This operation assigns discrete numbers representing the integral value to the 1-chain, c_1, just like 1-forms assigns numbers to vectors. In more general terms, consider a p-cochain, as a list of numbers, associated to a p-chain by means of pairing,

$$\langle C^{(p)}, C_{(p)} \rangle = \sum_{i=1}^{n_p} \sum_{j=1}^{n_p} a_i^{(p)} m_{(p)} \langle c_i^{(p)}, c_{(p),j} \rangle \tag{4-9}$$

Knowing that $\langle c_i^{(p)}, c_{(p),j} \rangle = \delta_{ij}$

$$\langle C^{(p)}, C_{(p)} \rangle = \sum_{i=1}^{n_p} a_i^{(p)} m_{(p)} \tag{4-10}$$

Equation (4-10) resembles $\left\langle \alpha^k, \mathcal{M}^k \right\rangle$, in which the p-cochain plays the role of the k-form and the p-chain is relate to the k-manifold.

Analogous, to the exterior derivative which maps k-forms to $k+1$-forms the coboundary operator does the same for the p-cochains mapping them into $(p+1)$-cochains.

$$\delta \quad : \quad C^p \rightarrow C^{p+1} \tag{4-11}$$

This operator is the formal adjoint of the boundary operator, ∂,

$$\langle \delta C^p, C_{p+1} \rangle := \langle C^p, \partial C_{p+1} \rangle \tag{4-12}$$

In $\mathbb{R}^3$ it is possible to construct the following exact sequence,

$$\begin{tikzcd} 0 \arrow[r] & C^0 \arrow[r, "\delta"] & C^1 \arrow[r, "\delta"] & C^2 \arrow[r, "\delta"] & C_3 \arrow[r] & 0 \end{tikzcd} \tag{4-13}$$

Comparing (4-12) with the generalized Stokes theorem,

$$\left\langle d\alpha^{(k-1)}, \mathcal{M}^k \right\rangle = \left\langle \alpha^{(k-1)}, \partial \mathcal{M}^k \right\rangle \tag{4-14}$$

The coboundary applied to cochains plays the same role as the exterior derivative applied to a k-form. Therefore, the coboundary represents the discrete version of the exterior derivative operator and can also be associated with the vector calculus operations, **grad**, **curl** and **div**.

Thus, the relations established from the generalized Stokes theorem can be stated exactly in terms of chains and cochains. It is important to keep in mind that all these operators are metric-free.

Figure 4-4 shows an example of the action of the coboundary operator.

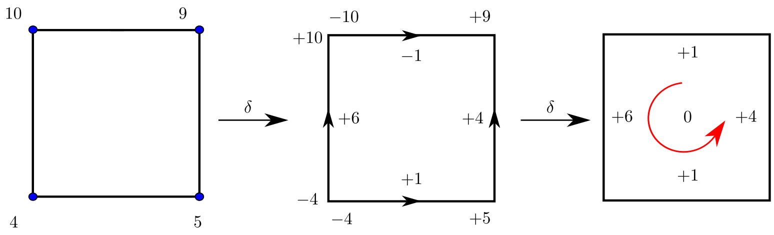

Figure 4-4: Coboundary operator example

In a more general framework,

$$\delta C^0 = C^1 = \begin{pmatrix} -1 & 1 & 0 & 0 \\ 0 & -1 & 1 & 0 \\ 0 & 0 & 1 & -1 \\ -1 & 0 & 0 & 1 \end{pmatrix} \begin{pmatrix} 4 \\ 5 \\ 9 \\ 10 \end{pmatrix} = \begin{pmatrix} 1 \\ 4 \\ -1 \\ 6 \end{pmatrix} \tag{4-15}$$

Similarly, to the boundary operator the coboundary consists in an incidence matrix $\mathbb{D}^{(1,0)}$ (subscript indicating a connection between from 1-cochains to 0-cochains).

$$\delta C^1 = \begin{pmatrix} 1 & 1 & -1 & -1 \end{pmatrix} \begin{pmatrix} 1 \\ 4 \\ -1 \\ 6 \end{pmatrix} = \begin{pmatrix} 0 \\ 0 \\ 0 \\ 0 \end{pmatrix} \tag{4-16}$$

Furthermore, as the double action of the exterior derivative, the coboundary operator also

$$\delta \circ \delta = 0. \tag{4-17}$$

This is a consequence of the fact that,

$$\left\langle \delta\delta C^{(p)}, C_{(p+2)} \right\rangle = \left\langle C^{(p)}, \partial\partial C_{(p+2)} \right\rangle = \left\langle C^{(p)}, 0 \right\rangle = 0. \tag{4-18}$$

Figure 4-5 shows a numbered and oriented primal cell complex for $\mathbb{R}^2$.

The coboundary operators for the numbered and labeled primal complex of Figure 4-5 are given in Tables 4-1 and 4-2.

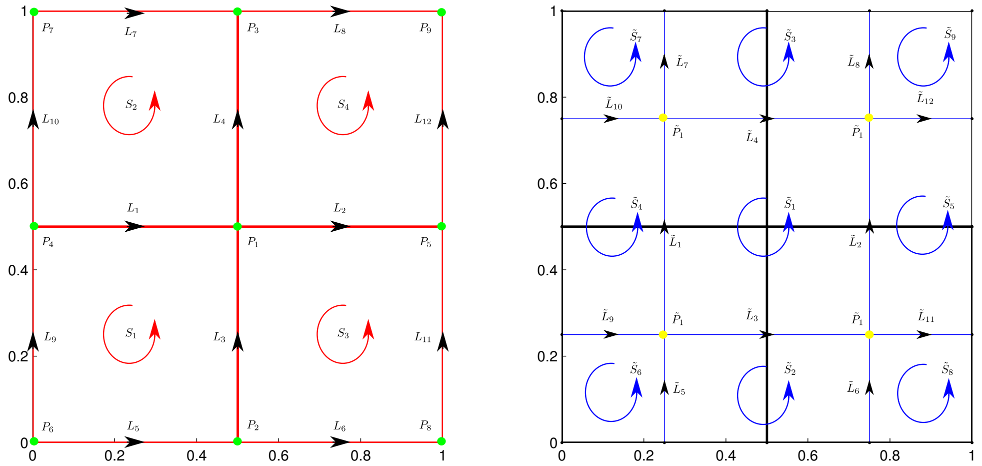
P_7
L_7
P_3
L_8
P_9
S_2
L_{10}
L_4
S_4
L_{12}
L_1
L_2
P_4
P_1
P_5
S_1
L_9
L_3
S_3
L_{11}
P_6
L_5
P_2
L_6
P_8
$\tilde{S}_7$
$\tilde{L}_7$
$\tilde{S}_3$
$\tilde{L}_8$
$\tilde{S}_9$
$\tilde{L}_{10}$
$\tilde{L}_{12}$
$\tilde{P}_1$
$\tilde{L}_4$
$\tilde{S}_4$
$\tilde{S}_1$
$\tilde{S}_5$
$\tilde{L}_1$
$\tilde{L}_2$
$\tilde{L}_9$
$\tilde{L}_3$
$\tilde{L}_{11}$
$\tilde{S}_6$
$\tilde{L}_5$
$\tilde{S}_2$
$\tilde{L}_6$
$\tilde{S}_8$
0
0.2
0.4
0.6
0.8
1

(a) Primal **(b)** Dual

Figure 4-5: Numbered primal and dual cell complex in $\mathbb{R}^2$

Table 4-1: Coboundary operator $\mathbb{D}^{(1,0)}$ for the labeled cochain complex of Figure 4-5

		Points								
		1	*2*	*3*	*4*	*5*	*6*	*7*	*8*	*9*
Edges	*1*	1	0	0	-1	0	0	0	0	0
	2	-1	0	0	0	1	0	0	0	0
	3	1	-1	0	0	0	0	0	0	0
	4	-1	0	1	0	0	0	0	0	0
	5	0	1	0	0	0	-1	0	0	0
	6	0	-1	0	0	0	0	0	1	0
	7	0	0	1	0	0	0	-1	0	0
	8	0	0	-1	0	0	0	0	0	1
	9	0	0	0	1	0	-1	0	0	0
	10	0	0	0	-1	0	0	1	0	0
	11	0	0	0	0	1	0	0	-1	0
	12	0	0	0	0	-1	0	0	0	1

Table 4-2: Coboundary operator $\mathbb{D}^{(2,1)}$ for the labeled cochain complex of Figure 4-5

		Edges											
		1	*2*	*3*	*4*	*5*	*6*	*7*	*8*	*9*	*10*	*11*	*12*
Surfaces	*1*	-1	0	1	0	1	0	0	0	-1	0	0	0
	2	1	0	0	1	0	0	-1	0	0	-1	0	0
	3	0	-1	-1	0	0	1	0	0	0	0	1	0
	4	0	1	0	-1	0	0	0	-1	0	0	0	1

The same analysis done for the primal complex can be extended to the dual complex. The coboundary operator in the dual complex can be constructed using the boundary operator. Consider the same initial example used in the primal complex the dual boundary operator can be defined,

$$\mathbb{F}_{(1,0)} = \begin{pmatrix} 1 \\ 1 \\ -1 \\ -1 \end{pmatrix} \quad \textit{and} \quad \mathbb{F}_{(2,1)} = \begin{pmatrix} -1 & 0 & 0 & -1 \\ 1 & -1 & 0 & 0 \\ 0 & 1 & 1 & 0 \\ 0 & 0 & -1 & 1 \end{pmatrix} \tag{4-19}$$

It should be clear that in the example of Figure 4-5 the incidence matrix $\mathbb{F}_{(1,0)} = \mathbb{E}^T_{(2,1)}$ and $\mathbb{F}_{(2,1)} = \mathbb{E}^T_{(1,0)}$. Figure 4-6 shows a cell complex for $\mathbb{R}^3$.

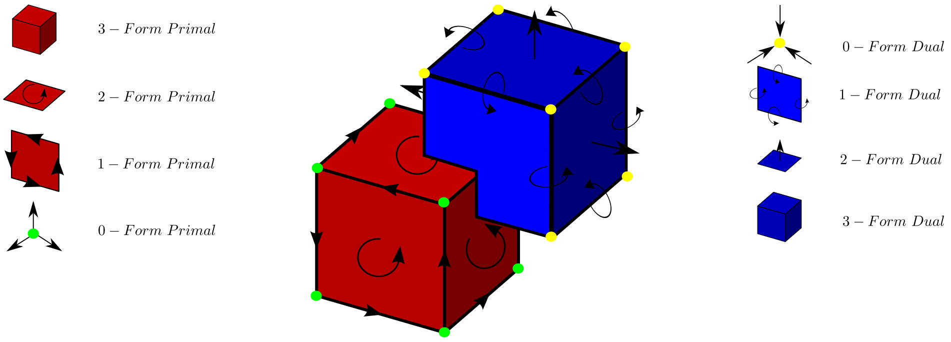

Figure 4-6: Primal and dual cell complex in $\mathbb{R}^3$

4-4 Discrete de Rham complex

The interaction between differential forms and manifolds with cochains and a cell complex is crucial. The connection between differential geometry and topology is established by the de Rham map. The top part of the de Rham complex can be rewritten in terms of the p-cochains

$$\begin{tikzcd} 0 \arrow[r] & C^0 \arrow[r, "\delta", "\nabla"'] & C^1 \arrow[r, "\delta", "\nabla\times"'] & C^2 \arrow[r, "\delta", "\nabla\cdot"'] & C^3 \arrow[r, "\delta"] & 0 \end{tikzcd} \tag{4-20}$$

Unfortunately, there isn't any analogues operation to the Hodge-$\star$ operator in algebraic topology that allows a connection between cell complexes.

$$\begin{tikzcd} \mathbb{R} \arrow[r] & C^0(K) \arrow[r, "\delta", "Grad"'] \arrow[d, "\star_h"] & C^1(K) \arrow[r, "\delta", "Curl"'] \arrow[d, "\star_h"] & C^2(K) \arrow[r, "\delta", "Div"'] \arrow[d, "\star_h"] & C^3(K) \arrow[r] \arrow[d, "\star_h"] & 0 \\ 0 & \widetilde{C}^3(K) \arrow[l] & \widetilde{C}^2(K) \arrow[l, "\delta", "Div"'] & \widetilde{C}^1(K) \arrow[l, "\delta", "Curl"'] & \widetilde{C}^0(K) \arrow[l, "\delta", "Grad"'] & \mathbb{R} \arrow[l] \end{tikzcd} \tag{4-21}$$

Chapter 5

Numerical implementation

The goal of this chapter is to establish a connection between continuous differential forms and discrete cochains. All discrete structures in our framework will be defined by using two basic operators.

Reduction, Section 5-1, of a physical model assures that the model behaves in the same way both in the full infinite dimensional and in the discrete system. Basically, this consists of mapping k-forms to k-cochains, meaning that even in the discrete world the generalized Stokes theorem is satisfied. This is given by the de Rham mapping.

On the other hand, reconstruction (Section 5-1) maps k-cochains into k-forms. This translates how local information is obtained from global representation. The choice of this operator is less restrictive and is in here that finite difference [40], finite volume [12], finite element [1] or something else can be chosen. Particularly, in the remainder of this thesis piecewise polynomial reconstructions common in spectral element methods, [13, 41, **?**, 42, 43] are used. Recently, experiments using isogeometric reconstruction were used [44, 45, 46]. In Section 5-3 and Section 5-4 the action of the reduction and reconstruction is generalized from one-dimensional to multi-dimensional, respectively.

5-1 Reduction operator

A crucial step is to correctly map differential forms to their discrete version, cochains. Lets consider a cell-complex, such that all p-chains, $C_{(p)}$, the reduction operation is the de Rham mapping,

$$\mathcal{R} \quad : \quad \Lambda^k(\Omega) \to C^k(D) \tag{5-1}$$

defined as,

$$\langle \mathcal{R}\alpha^p, C_{(p)} \rangle := \int_{C_{(p)}} \alpha^p \tag{5-2}$$

Knowing that $C_{(p)} = \sum_{i=1}^{n_p} m_{(p),i} c_{(p),i}$

$$\sum_{i=1}^{n_p} m_{(p),i} \langle \mathcal{R}\alpha^p, c_{(p)} \rangle = \sum_{i=1}^{n_p} m_{(p),i} \int_{c_{(p)}} \alpha^p \tag{5-3}$$

The reduction operator is completely determined by integration over all individual p-cells. Table 5-1 summarizes the action of the reduction operator in k-forms in $\mathbb{R}^3$.

Table 5-1: Connection between differential forms and co-chains established by the Reduction operator

0-Forms	Point values - $\sum_{i=1}^{n_P} \alpha^0(P_i)c_i^0$
1-Forms	Line integrals - $\sum_{i=1}^{n_L} [\int_{L_i} \alpha^1]c_i^1$
2-Forms	Surface integrals - $\sum_{i=1}^{n_S} [\int_{S_i} \alpha^2]c_i^2$
3-Forms	Volume integrals - $\sum_{i=1}^{n_V} [\int_{V_i} \alpha^3]c_i^3$

The reduction operator has a commuting property with respect to continuous and discrete differentiation,

$$\mathcal{R}d = \delta\mathcal{R}. \tag{5-4}$$

This is summarized in the following diagram,

$$\begin{tikzcd}
\Lambda^k \arrow[r, "d"] \arrow[d, "\mathcal{R}"] & \Lambda^{k+1} \arrow[d, "\mathcal{R}"] \\
C^k \arrow[r, "\delta"] & C^{k+1}
\end{tikzcd} \tag{5-5}$$

This is easily proved by the using the Stokes theorem,

$$\langle \mathcal{R}d\alpha^p, C_{(p)} \rangle = \int_{C_{(p)}} d\alpha^p = \int_{\partial C_{(p)}} \alpha^p = \langle \mathcal{R}\alpha^p, \partial C_{(p)} \rangle = \langle \delta\mathcal{R}\alpha^p, C_{(p)} \rangle \tag{5-6}$$

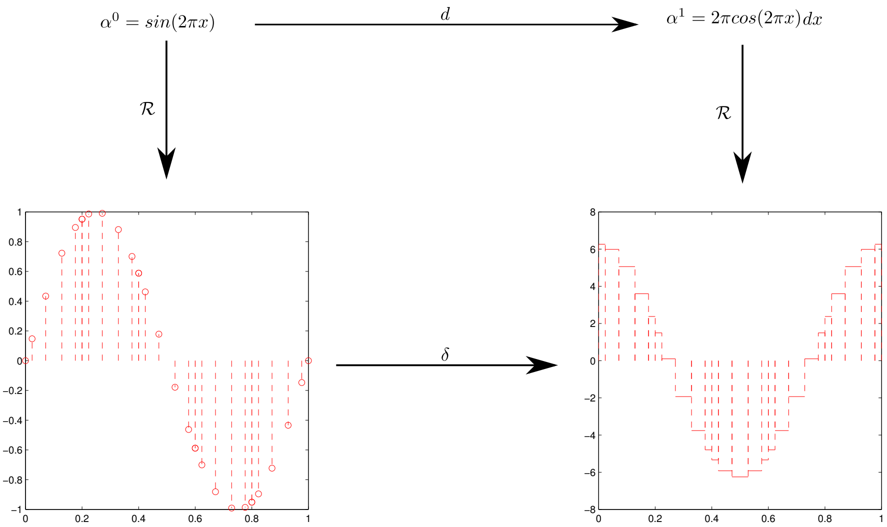

Figure 5-1: Reduction and exterior derivative of a 0-form for $sin(2\pi x)$

5-2 Reconstruction operator

The operator acting in the opposite direction to the reduction is the reconstruction operator, i.e. it maps cochains to k-forms.

$$\mathcal{L} \quad : \quad C^k(D) \to \Lambda^k(\Omega) \tag{5-7}$$

Opposite to the reduction where a natural candidate emerges naturally there is more flexibility to choose the reconstruction operator because the de Rham map is not invertible. This operator maps p-cochains to k-forms, in such a way that the reduction of all reconstruction p-forms gives the original cochains,

$$\mathcal{R} \circ \mathcal{L} = id \tag{5-8}$$

Similarly, to the reduction the reconstruction also commutes with respect to differentiation,

$$\begin{tikzcd}
\Lambda^k \arrow[d, "d"] & C^k \arrow[l, "\mathcal{L}_k"'] \arrow[d, "\delta"] \\
\Lambda^{k+1} & C^{k+1} \arrow[l, "\mathcal{L}_{k+1}"']
\end{tikzcd} \tag{5-9}$$

Furthermore, the reconstruction operator needs to be linear, i.e. for all p-cochains $C^{(p)}$ and $D^{(p)}$ defined on the same cell complex, and all γ and $\beta \in \mathbb{R}$,

$$\mathcal{L}(\gamma C^{(p)} + \beta D^{(p)}) = \gamma \mathcal{L}(C^{(p)}) + \beta \mathcal{L}(D^{(p)}) \tag{5-10}$$

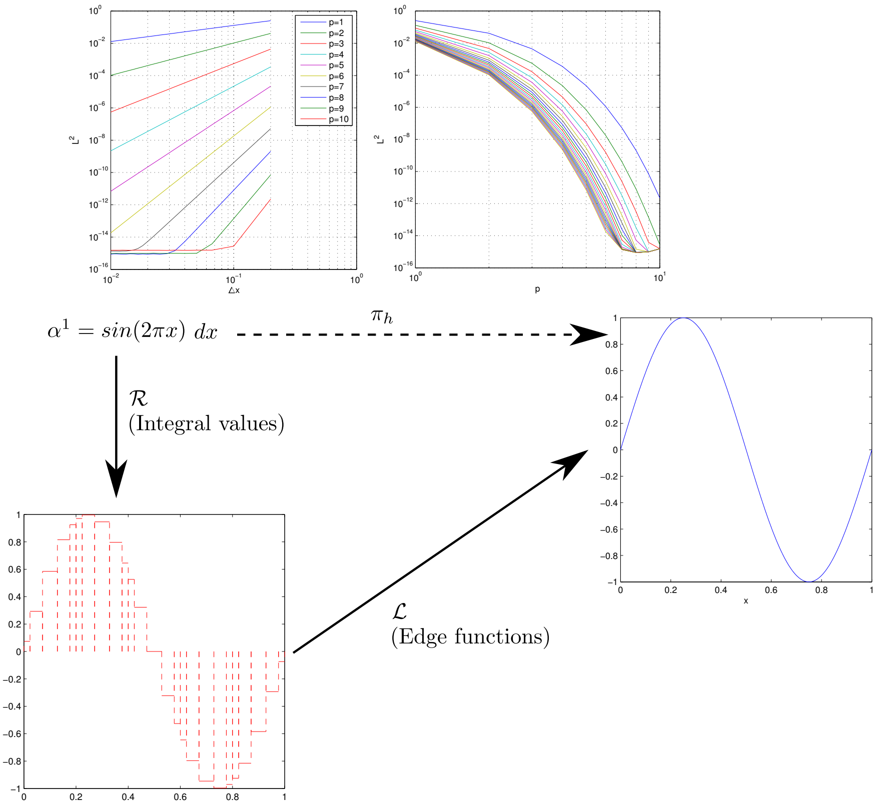

Figure 5-2: Reduction and Reconstruction of a 1-form for $sin(2\pi x)$

However, de Rham map is not invertible the approximation property should be defined, i.e. $\mathcal{L} \circ \mathcal{R} = id + O(h^p)$, where h denotes the size of the p-chains and p the polynomial order of the reconstruction. Therefore, a projection operator can be constructed, $\pi := \mathcal{L} \circ \mathcal{R}$,

$$\begin{tikzcd}
\Lambda^k \arrow[r, dashed, "\pi_h"] \arrow[d, "\mathcal{R}"] & \Lambda^k_h \\
C^k \arrow[ur, "\mathcal{L}"'] &
\end{tikzcd} \tag{5-11}$$

Furthermore, the projection operator also commutes with respect to differentiation both continous and finite dimensional,

$$\begin{tikzcd}
\Lambda^k \arrow[r, "d"] \arrow[d, "\pi_h"] & \Lambda^{k+1} \arrow[d, "\pi_h"] \\
\Lambda^k_h \arrow[r, "d"] & \Lambda^{k+1}_h
\end{tikzcd} \tag{5-12}$$

5-3 Reduction and reconstruction of k-forms

In the previous sections a general framework was derived giving general indications on how to choose the reduction, $\mathcal{R}$, and the reconstruction, $\mathcal{L}$, operators. From this point onwards, the use of polynomial discrete representation of k-forms is going to be explained with examples for 1D, 2D and 3D. More formal definitions can be found in [43, 47].

5-3-1 0-forms

Assume a partitioning of the interval, $[a, b]$ given by $a = x_0 < x_1 < \cdots < x_N = b$. Consider a 0-form $\alpha^0(x) = f(x)$. The 0-chain is a collection of the nodal points, $x_0, \cdots, x_N$, and the 0-cochain the value of the function at each nodal point. The reduction operator of 0-forms,

$$\alpha_i^0(x) = \int_{x_i} \alpha^0(x) = \left\langle \alpha^0, x_i \right\rangle \tag{5-13}$$

this consist in computing the the value of the 0-form in each point. By integrating over all 0-cells the 0-cochain is obtained. A continuous representation of the 0-cochain is given by,

$$\alpha^0(x) = \sum_{i=0}^{N} f(x_i) h_i(x) \tag{5-14}$$

where $h_i(x)$ is the Lagrange polynomial through the points x_i, i.e. $h_i(x)$ is a polynomial of degree $n_p - 1$ such that,

$$h_i(P_j) = \begin{cases} 1 & if\ i = j \\ 0 & if\ i \neq j \end{cases} \tag{5-15}$$

The reconstruction of the 0-cochain, $C^{(0)} = \sum_{i=1}^{n_p} a_i c_i^{(0)}$ is given by,

$$a_h^{(0)}(x) = \mathcal{L}(C^{(0)}) = \sum_{i=1}^{n_p} a_i h_i(x) \tag{5-16}$$

This is no more than the usual nodal interpolation.

5-3-2 1-forms

This stage is a crucial point in the development of the mimetic discretization. Equivalent, to the reduction of 0-forms, the 1-cochain is computed by means of integration. Thus, 1-cochains consist of a line integrals over a collection of 1-chains. Consider the 1-form, α^1 and the 1-cell, (x_{i-1}, x_i), then the 1-cochain is given by,

$$\alpha_i^1 = \int_{x_{i-1}}^{x_i} \alpha^1(x) = \left\langle \alpha^1(x), (x_{i-1}, x_i) \right\rangle . \tag{5-17}$$

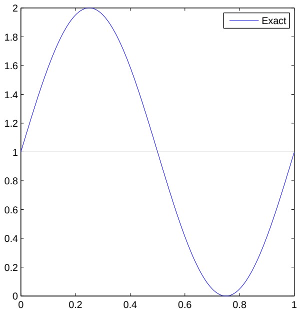

(a) Exact solution

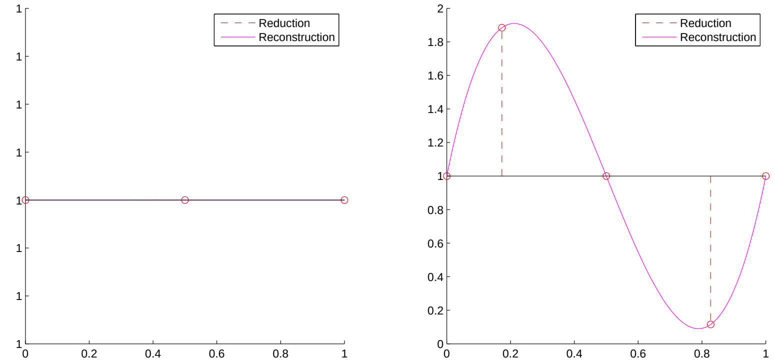

(b) $p = 2$ **(c)** $p = 4$

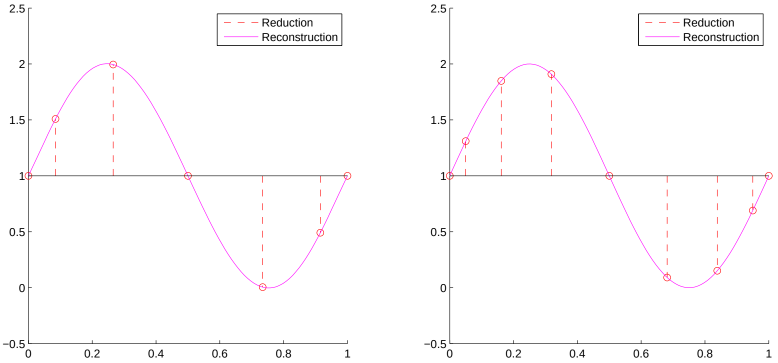

(d) $p = 6$ **(e)** $p = 8$

Figure 5-3: Reduction and reconstruction of a 0-form for $sin(2\pi x) + 1$

At this stage, its crucial to define a consistent procedure that allows to interpolate the values such that after reduction the same values are retrieved. The standard Lagrange nodal interpolation is not sufficient. So, knowing that an exterior derivative can be applied to a 0-form and a 1-form is obtained,

$$a_h^{(1)}(x) = d\sum_{i=1}^{n_p} a_i h_i(x) = \sum_{i=1}^{n_p} a_i dh_i(x). \tag{5-18}$$

Therefore, a 1-form can thus be expanded as

$$a_h^{(1)}(x) = \sum_{i=1}^{n_l} \overline{a_i} e_i(x). \tag{5-19}$$

Therefore, the edge functions, introduced in [48], needs to satisfy

$$\int_{L_j} e_i(x) = \begin{cases} 1 & if\ i = j \\ 0 & if\ i \neq j \end{cases} \tag{5-20}$$

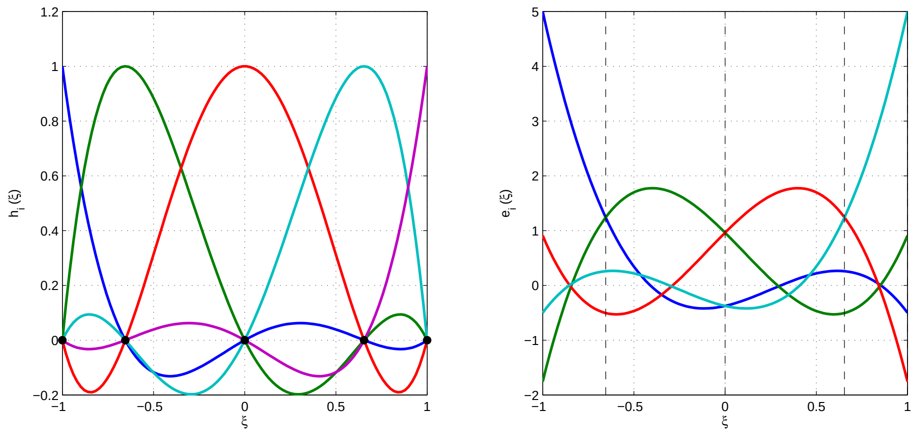

(a) Lagrange interpolation **(b)** Edge interpolation

Figure 5-4: Reconstruction basis functions on Gauss-Lobatto nodes

These are polynomials, $e_i(x)$ of degree $n_e - 1$, a detailed derivation can be found in Appendix A. Therefore, its possible to reconstruct the 1-form, α^1,

$$\alpha^1(x) = \sum_{i=1}^{N} \alpha_i^1 e_i(x). \tag{5-21}$$

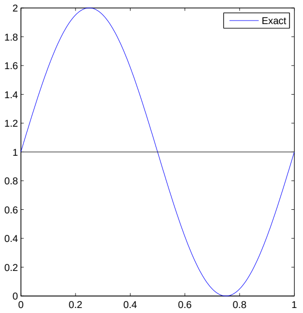

(a) Exact solution

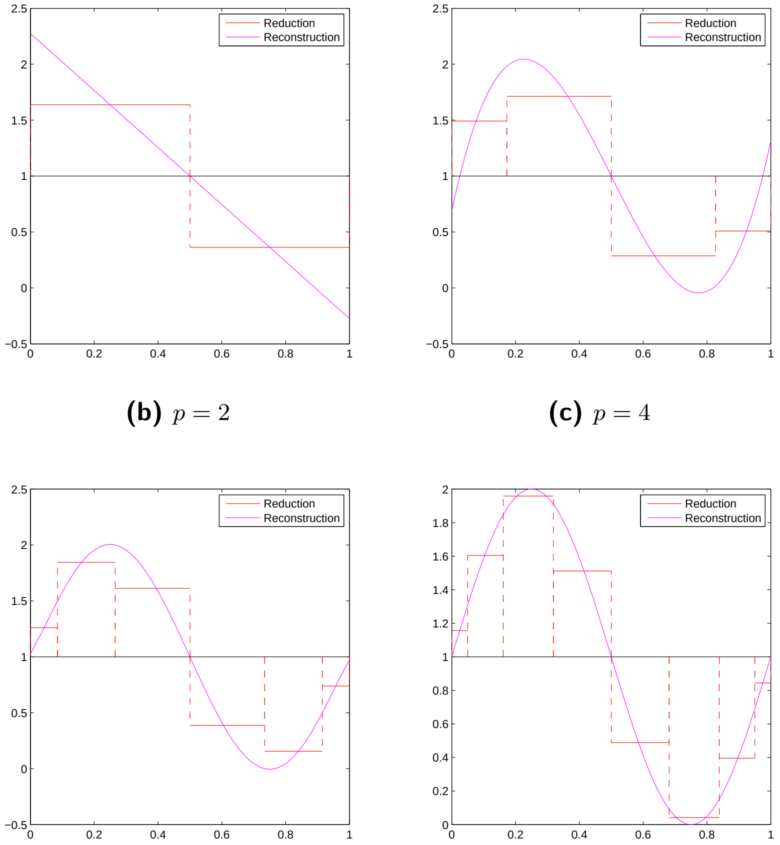

(b) $p = 2$

(c) $p = 4$

(d) $p = 6$

(e) $p = 8$

Figure 5-5: Reduction and reconstruction of a 1-form for $sin(2\pi x) + 1$

5-4 Multidimensional problems

Until this point, only discretization in $\mathbb{R}^1$ were discussed. However, this concepts can be easily generalized by means of tensor products, this is summarized in Table 5-2. As mentioned before a correct discretization of the de Rham complex has several advantageous. The use of of a proper reduction and reconstruction allows to construct the following commuting diagram,

$$\begin{tikzcd}
\mathbb{R} \arrow[r] & \Lambda^0(\Omega) \arrow[r, "d", "Grad"'] \arrow[d, bend right, "\mathcal{R}^0"'] & \Lambda^1(\Omega) \arrow[r, "d", "Curl"'] \arrow[d, bend right, "\mathcal{R}^1"'] & \Lambda^2(\Omega) \arrow[r, "d", "Div"'] \arrow[d, bend right, "\mathcal{R}^2"'] & \Lambda^3(\Omega) \arrow[d, bend right, "\mathcal{R}^3"'] \\
\mathbb{R} \arrow[r] & C^0(\Omega) \arrow[r, "\delta"] \arrow[u, bend right, "\mathcal{L}^0"'] & C^1(\Omega) \arrow[r, "\delta"] \arrow[u, bend right, "\mathcal{L}^1"'] & C^2(\Omega) \arrow[r, "\delta"] \arrow[u, bend right, "\mathcal{L}^2"'] & C^3(\Omega) \arrow[u, bend right, "\mathcal{L}^3"']
\end{tikzcd} \tag{5-22}$$

Table 5-2: Reconstruction of k-forms for $\mathbb{R}^3$

$0-Forms$	$\alpha_h^0(x,y,z)$	$=$	$\sum_{i=1}^{N_{px}}\sum_{j=1}^{N_{py}}\sum_{k=1}^{N_{pz}}\alpha_{i,j,k}h_i(x)h_j(y)h_k(z)$
$1-Forms$	$\alpha_h^1(x,y,z)$	$=$	$\sum_{i=1}^{N_{lx}}\sum_{j=1}^{N_{py}}\sum_{k=1}^{N_{pz}}\alpha_{i,j,k}^x e_i(x)h_j(y)h_k(z)+$
			$\sum_{i=1}^{N_{px}}\sum_{j=1}^{N_{ly}}\sum_{k=1}^{N_{pz}}\alpha_{i,j,k}^y h_i(x)e_j(y)h_k(z)+$
			$\sum_{i=1}^{N_{px}}\sum_{j=1}^{N_{py}}\sum_{k=1}^{N_{lz}}\alpha_{i,j,k}^z h_i(x)h_j(y)e_k(z)$
$2-Forms$	$\alpha_h^2(x,y,z)$	$=$	$\sum_{i=1}^{N_{px}}\sum_{j=1}^{N_{ly}}\sum_{k=1}^{N_{lz}}\alpha_{i,j,k}^x h_i(x)e_j(y)e_k(z)+$
			$\sum_{i=1}^{N_{lx}}\sum_{j=1}^{N_{py}}\sum_{k=1}^{N_{lz}}\alpha_{i,j,k}^y e_i(x)h_j(y)e_k(z)+$
			$\sum_{i=1}^{N_{lx}}\sum_{j=1}^{N_{ly}}\sum_{k=1}^{N_{pz}}\alpha_{i,j,k}^z e_i(x)e_j(y)h_k(z)$
$3-Forms$	$\alpha_h^3(x,y,z)$	$=$	$\sum_{i=1}^{N_{vx}}\sum_{j=1}^{N_{vy}}\sum_{k=1}^{N_{vz}}\alpha_{i,j,k}e_i(x)e_j(y)e_k(z)$

Table 5-3: Reconstruction of k-forms for $\mathbb{R}^2$

$0-Forms$	$\phi_h^0(x,y)$	$=$	$\sum_{i=1}^{N_{px}}\sum_{j=1}^{N_{py}}\phi_{i,j}^0 h_i(x)h_j(y)$
$1-Forms$	$\alpha_h^1(x,y)$	$=$	$\sum_{i=1}^{N_{lx}}\sum_{j=1}^{N_{py}}{}^x\alpha_{i,j}^x e_i(x)h_j(y)+\sum_{i=1}^{N_{px}}\sum_{j=1}^{N_{ly}}{}^y\alpha_{i,j}^y h_i(x)e_j(y)$
$2-Forms$	$\rho_h^2(x,y)$	$=$	$\sum_{i=1}^{N_{lx}}\sum_{j=1}^{N_{ly}}\rho_{i,j}^2 e_i(x)e_j(y)$

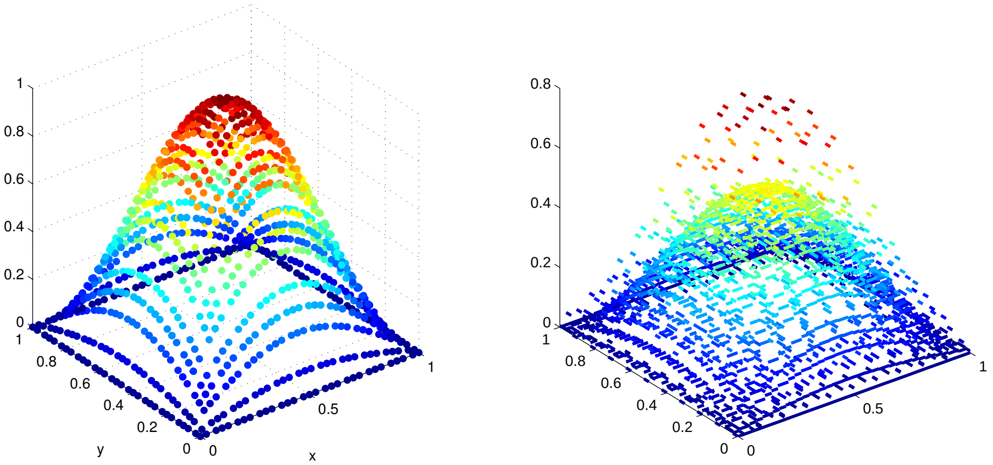

(a) $sin(2\pi x)sin(2\pi y)$ Reducted

(b) $sin(2\pi x)sin(2\pi y)dx$ + $sin(2\pi x)sin(2\pi y)dy$ Reducted

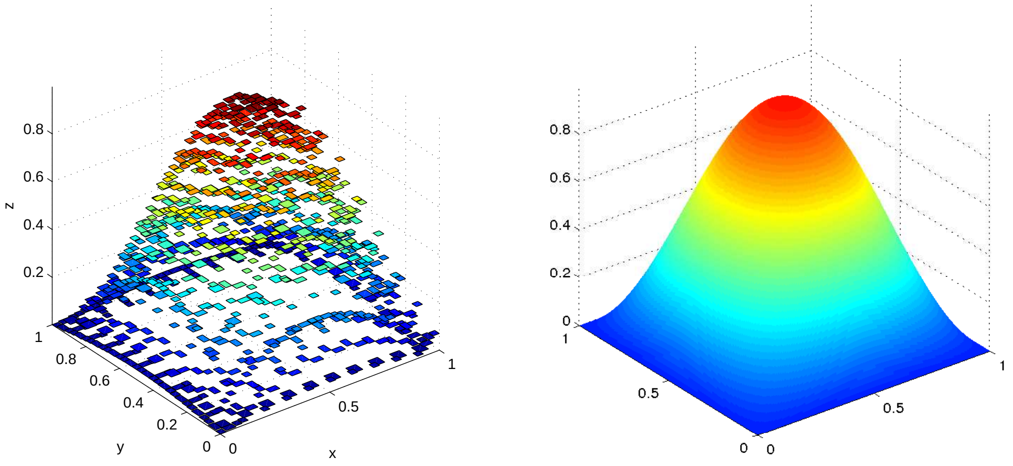

(c) $sin(2\pi x)sin(2\pi y)dxdy$ Reducted

(d) Reconstructed

Figure 5-6: Reduction and reconstruction of a k-form in $\mathbb{R}^2$

Chapter 6

Geometric integration

The topic of this chapter is the construction of structure-preserving numerical integrators for ordinary differential equations (ODEs). ODEs are ubiquitous, appearing from particle accelerators, molecular dynamics to structural analysis. In Chapter 3 it was shown that the Lie derivative can be computed in a dynamic perspective by determining the integral curve from a velocity field. For example, for a vector field, $\mathbf{v} = (x, y)$ there is an analytical solution for the flow given by $\phi_t(x, y) = (e^t x, e^t y)$. However, analytical solution for this ODE system are not always possible.

Important continuous symmetries are not unique to PDE's they are also also a feature in ODE's. Besides the common structures, e.g mass, momentum and volume, there is one which is less obvious, the symplectic form for Hamiltonian systems. Non-dissipative phenomena are often modeled by Hamiltonian systems of differential equations. Integrators for Hamiltonian systems that preserve a discrete notion of the symplectic form are named symplectic integrators. The concept of Hamiltonian is very often connected with the total energy of the system, and therefore the conservation of the symplectic structure implies energy conservation. They were first introduced by Vogelaere [49]. Later on, Ruth [50] constructed symplectic integrators while researching particle accelerators. After this the range of applications increased exponentially, ranging from stock market modeling to celestial mechanics. A detail review of the available symplectic integrators [2].

Section 6-1 gives a brief overview of qualitative inherent physical structures. In section 6-2 the construction of Hamiltonian systems is explained. Section 6-3 reviews known symplectic algorithms and the a new arbitrary order mimetic symplectic integrator is introduced. In section 6-4 all the previous integrators are tested in a set of benchmark test cases.

6-1 Why preserve structure?

Before detailing the advantageous of preserving the structures of a differential equation it is important to describe what these structures are. It is well know, that for any mechanical system the total energy should be preserved. Thus, this is a structure inherent to the differential equation. Furthermore, the principle that in nature *Nothing is created, nothing is lost, everything is transformed* reflects the conservation of mass which is also a structure of a differential system. As previously mentioned, in the case of rigid body dynamics the linear momentum should be preserved, this is also an invariant of the system. Further details can be found in [50].

Standard numerical methods for differential equations tend to focus their analysis in the local truncation errors. However, as mentioned, minimizing the error does not imply that the physical structures are preserved. The main advantageous of preserving the inherent structures of the differential equations are:

- the discrete system has the same properties as the continuous
- excellent energy conservation properties
- can conserve angular momentum or even unknown structures
- accurate computation of singularities

The aim of this section is not to detail every possible structure, but, instead give a general overview. For more examples consult [2, 50].

6-2 Hamiltonian system

Consider the generalized coordinates $\mathbf{q} \in \mathbb{R}^d$, i.e. $\mathbf{q}$ represents the position of a mechanical system with d degrees of freedom described by,

$$\mathbf{q} = (q_1, \cdots, q_d)^T . \tag{6-1}$$

Consider the kinetic energy of the form,

$$T \equiv T(\mathbf{q}, \dot{\mathbf{q}}), \tag{6-2}$$

and the potential energy,

$$V \equiv V(\mathbf{q}). \tag{6-3}$$

Then the corresponding Lagrangian is given by,

$$L = T - V. \tag{6-4}$$

Thus, the the coordinates $\mathbf{q}$ obey the following set of differential equations

$$\frac{d}{dt}\left(\frac{\partial L}{\partial \dot{q}_k}\right) - \frac{\partial L}{\partial q_k} = 0, \quad \text{for } k = 1, \cdots d. \tag{6-5}$$

Therefore, the solution of these differential equations allows to predict the motion of the system. For example, let m be a mass point in $\mathbb{R}^3$ with Cartesian coordinates, $(x_1, x_2, x_3)^T$. The kinetic energy is given by,

$$T = \frac{1}{2}\left(\dot{x}_1^2 + \dot{x}_2^2 + \dot{x}_3^2\right). \tag{6-6}$$

Suppose the point is moving in a conservative force field, $F(x) = -\nabla U(x)$. Thus, the Lagragian leads to

$$m\ddot{x} = F(x), \tag{6-7}$$

which is Newton's second law.

Hamilton simplified the structure of Lagrange's equations. Consider the conjugate generalized momentum,

$$p = \frac{\partial L}{\partial \dot{\mathbf{q}}} \in \mathbb{R}^d, \tag{6-8}$$

and define the Hamiltonian expressing $\dot{q} = \dot{q}(p, q)$

$$H(\mathbf{p}, \mathbf{q}) = \mathbf{p}^T\dot{\mathbf{q}} - L(\mathbf{q}, \dot{\mathbf{q}}). \tag{6-9}$$

Lagrange's equations are equivalent to Hamilton's equations

$$\begin{aligned} \dot{\mathbf{p}} &= -\frac{\partial H}{\partial \mathbf{q}} \\ \dot{\mathbf{q}} &= \frac{\partial H}{\partial \mathbf{p}}. \end{aligned} \tag{6-10}$$

Assuming a quadratic kinetic energy,

$$T = \frac{1}{2}\dot{q}^T M(q)\dot{q}, \tag{6-11}$$

where $M(q)$ is symmetric and positive definitive matrix. For a fixed q,

$$p = M(q)\dot{q}. \tag{6-12}$$

Thus, the Hamiltonian can be defined,

$$\begin{aligned} H(p, q) &= p^T M^{-1}(q)p - L(q, M^{-1}(q)) \\ &= \frac{1}{2}p^T M^{-1}(q)p + U(q), \end{aligned} \tag{6-13}$$

which is the total energy of the system. Thus, for quadratic kinetic energies the Hamiltonian represents the total energy.

Besides, the conservation of the Hamiltonian a key feature of Hamiltonian systems is also the *symplecticity* of its flow. The solution of (6-9) induces a transformation ψ on the phase space $\mathbb{R}^{2d}$ with the associated Jacobian ψ'. Such a map is said to be symplectic if

$$\psi'^T J \psi' = J \tag{6-14}$$

6-3 Numerical integrators

In this section the standard integrators such as explicit and implicit Euler and mid-point are reviewed. Afterwards, special attention is given to symplectic integrators such as the symplectic Euler, Stormer/Verlet and the Gauss Runge Kutta method. Finally, the new mimetic integrator is introduced and its symplectic and symmetric nature is explained.

6-3-1 Explicit Euler

The simplest of all numerical methods. The method was formulated by Euler in 1768,

$$y_{n+1} = y_n + \Delta t f(y_n). \tag{6-15}$$

The method is called explicit because the approximation y_{n+1} is computed using an explicit evaluation of f at the already known value y_n.

6-3-2 Implicit Euler

The implicit Euler is given by

$$y_{n+1} = y_n + \Delta t f(y_{n+1}). \tag{6-16}$$

In contrast to (6-15) the approximation y_{n+1} is defined implicitly, i.e. $f(y_{n+1})$. The implementation requires a numerical solution of a nonlinear system of equations.

6-3-3 Implicit mid-point

The implicit mid-point takes a mean of y_n and y_{n+1},

$$y_{n+1} = y_n + \Delta t f\left(\frac{y_n + y_{n+1}}{2}\right). \tag{6-17}$$

6-3-4 Symplectic Euler

As shown by [51] a combination between explicit and implicit methods produces a symplectic method. For partitioned systems, i.e

$$\begin{cases} \dot{u} = a(u, v) \\ \dot{v} = b(u, v) \end{cases}$$

The symplectic Euler method is defined as

$$\begin{cases} u_{n+1} = u_n + \Delta t a(u_{n+1}, v_n) \\ v_{n+1} = v_n + \Delta t b(u_{n+1}, v_n) \end{cases} . \tag{6-18}$$

6-3-5 Stormer/Verlet

Consider a system of second order differential equations,

$$\ddot{q} = f(q), \tag{6-19}$$

where the right hand side, $f(q)$, does not depend on $\dot{q}$. Taking a step size, Δt, and the grid points, $t_n = t_0 + \Delta t n$, the most natural discretization of (6-19) is,

$$q_{n+1} - 2q_n + q_{n-1} = \Delta t^2 f(q_n). \tag{6-20}$$

This is simply a second-order central differencing. Geometrically, this consists in determining the interpolating parabola that has a second-order derivative in the mid-point determined by 6-19. This is a two-step formulation.

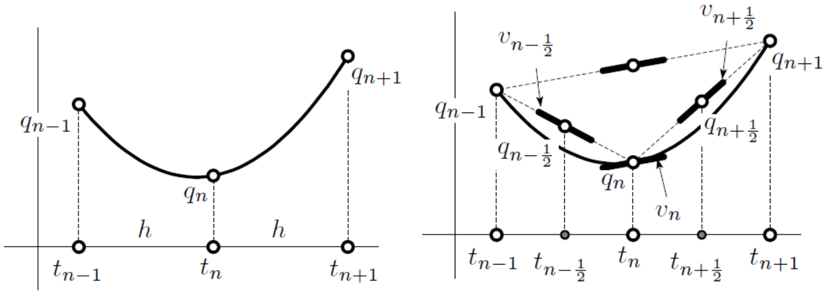

(a) Two step formulation **(b)** One step formulation

Figure 6-1: Geometric interpretation of the Stormer/Verlet method [2]

If the velocity, $\dot{q} = v$, is introduced into equation 6-19,

$$\dot{q} = v, \quad \dot{v} = f(q). \tag{6-21}$$

The discrete approximations for v and q are,

$$v_n = \frac{q_{n+1} - q_{n-1}}{2\Delta t}. \tag{6-22}$$

Introducing the velocity approximations at the midpoint, a one-step formulation is given by,

$$\begin{aligned} v_{n+1/2} &= v_n + \frac{\Delta t}{2} f(q_n), \\ q_{n+1} &= q_n + \Delta t v_{n+1/2}, \\ v_{n+1} &= v_{n+1/2} + \frac{\Delta t}{2} f(q_{n+1}). \end{aligned} \tag{6-23}$$

This is known as the Stormer/Verlet method. It has been proven to be a second order symplectic and symmetric method. In practical terms the conservation of the symplectic structure is associated with the accurate long energy behavior and the symmetric property with the non dissipative character of the integration scheme.

6-3-6 Runge-Kutta

Runge-Kutta methods form an important class of methods for the integration of differential equations. These are one-step methods for the numerical solution of initial value problems,

$$\dot{y} = f(y(x)), \quad y(x_0) = y_0, \quad y(x) \in \mathbb{R}^m. \tag{6-24}$$

The general form of a Runge-Kutta method is given by,

$$\begin{aligned} Y_i &= y_{n-1} + \sum_{j=1}^{s} a_{ij} \Delta t f(Y_j), \\ y_n &= y_{n-1} + \sum_{i=1}^{s} b_i \Delta t f(Y_i). \end{aligned} \tag{6-25}$$

It is also common in literature that $f(Y_i) = k_i$. The computed value, y_n, is an approximation of the exact solution, $y(x_n)$. Furthermore, the coefficients of a Runge-Kutta can be represented in a Butcher tableau,

Table 6-1: Genral Butcher tableau

c_1	a_{11}	$\dots$	a_{1s}
$\vdots$	$\vdots$		$\vdots$
c_s	a_{s1}	$\dots$	a_{ss}
	b_1	$\dots$	b_s

where b_i are called the weights of the method - $\sum_{i=1}^{s} b_i = 1$ - and $c_i = \sum_{j=1}^{s} a_{ij}$ for $i = 1, \cdots, s$ are the abscissas location at which the stages Y_i are computed. Figure 6-2 shows a geometric representation of the general Runge-Kutta method.

A Runge-Kutta method is explicit if $a_{ij} = 0$ for $i \leq j$. One main advantage of this is that the stages can be computed sequentially. Therefore, this is cheaper in terms of computational cost. However, explicit Runge-Kutta schemes are limited in their stability and are unable

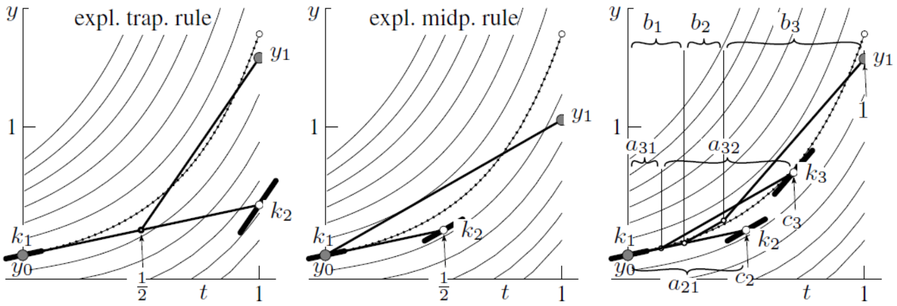

Figure 6-2: Geometric interpretation of Runge-Kutta method for $\dot{y} = t^2 + y^2$, $y_0 = 0.46$, $h = 1$; dotted: exact solution [2]

Table 6-2: Fourth order explicit Runge-Kutta

0				
1/2	1/2			
1/2	0	1/2		
1	0	0	1	
	1/6	1/3	1/3	1/6

to solve general Hamiltonian problems that are not separable. The classic 4th order explicit Runge-Kutta tableau is shown in Table 6-2.

On the other hand, Runge-Kutta schemes are implicit if $a_{ij} \neq 0$ for some $i \leq j$. Thus, for an s-stage implicit Runge-Kutta method it is necessary to solve a set of non-linear equations. It is common practice to use Netwon iterations to achieve this. To reduce the introduction of iterative errors on the solutions, it is convenient to reformulate the problem as

$$z = \Delta t A F(z), \tag{6-26}$$

where $z = (z_1, z_2, \ldots, z_s)^t$ with $z_i = y_0 - y_n$,

$$A = \begin{pmatrix} a_{11} & a_{12} & \ldots & a_{1s} \\ a_{21} & a_{22} & \ldots & a_{2s} \\ \vdots & \vdots & \ddots & \vdots \\ a_{s1} & a_{s2} & \ldots & a_{ss} \end{pmatrix}, and \quad F(z) = \begin{pmatrix} f(t_n + c_1\Delta t, z_1 + y_n) \\ f(t_n + c_2\Delta t, z_2 + y_n) \\ \vdots \\ f(t_n + c_s\Delta t, z_s + y_n) \end{pmatrix}. \tag{6-27}$$

If the matrix A^{-1} exists, (6-26) can be written as $\Delta t F(z) = A^{-1}z$ so the update formula can be simplified

$$y_{n+1} = y_n + (b_1, b_2, \ldots, b_s)\Delta t F(z) = y_n + (b_1, b_2, b_3, \ldots, b_s)A^{-1}z \tag{6-28}$$

This tends to be computationally expensive when compared to explicit methods. However, with fewer stages it is possible to achieve the same order of an explicit method. The better stability of these methods and the ability to preserve the structures underlying ODEs makes them very relevant. Inside the subclass of symplectic methods, that only exist for implicit

Runge-Kutta schemes, Gauss-Legendre schemes are the most important ones. These methods are constructed making the abscissa, $c_i = 0$ for the shifted Legendre polynomials, $P_S^\star$,

$$P_S^\star = \frac{s!}{2s} \sum_{k=0}^{s} (-1)^{s-k} \binom{s}{k} \binom{s+k}{k} x^k \tag{6-29}$$

For example, taking $s = 1$,

$$P_1^\star(x) = x - \frac{1}{2} \tag{6-30}$$

The zero of this polynomial is the abscissa of the 1-stage Gauss Runge-Kutta method, i.e. $c_1 = 1/2$, this is the second order implicit midpoint rule. Furthermore, taking $s = 2$,

$$P_2^\star(x) = x^2 - x + \frac{1}{6} \tag{6-31}$$

The zeros for this polynomion are, $c_1 = \frac{1}{2} - \frac{\sqrt{3}}{6}$ and $c_1 = \frac{1}{2} + \frac{\sqrt{3}}{6}$, the butcher tableau obtained is given in Table 6-3.

Table 6-3: Gauss-Legendre method of order 4 ($s = 2$)

$\frac{1}{2} - \frac{\sqrt{3}}{6}$	$\frac{1}{4}$	$\frac{1}{4} - \frac{\sqrt{3}}{6}$
$\frac{1}{2} + \frac{\sqrt{3}}{6}$	$\frac{1}{4} + \frac{\sqrt{3}}{6}$	$\frac{1}{4}$
	$\frac{1}{2}$	$\frac{1}{2}$

These methods have the maximum possible order for an s-stage, i.e. 2s order. Butcher tableaus for $s = 3$, $s = 4$ and $s = 5$ can be found in Appendix B. It has been proven that for a Runge-Kutta method to be symplectic the coefficients must satisfy [2],

$$b_i a_{ij} + b_j a_{ji} = b_i b_j \text{ for all } i, j = 1, \ldots, s \tag{6-32}$$

Other characteristics such as A-stability, B-Stability and L-Stability are also relevant in certain applications. Although, this are not subject of study hereafter, for more details see [52, 53].

6-3-7 Mimetic geometric integrator

Consider a system given by,

$$\dot{y} = f(y(t)). \tag{6-33}$$

Both sides can be integrated in time,

$$\int_{t_n}^{t_{n+1}} \frac{dy}{dt} dt = \int_{t_n}^{t_{n+1}} f(y(t)) dt. \tag{6-34}$$

Thus,

$$y_{n+1} = y_n + \int_{t_n}^{t_{n+1}} f(y(t))dt. \tag{6-35}$$

Applying a quadrature to the integral,

$$y_{n+1} = y_n + \Delta t \sum_i w_i f(y_{t_i}), \tag{6-36}$$

where $y_{t_i} = t(t_i)$, $ti \in [t_n, t_{n+1}]$. The values of y_{t_i} can be interpolated by using a Lagrange polynomial,

$$y_{n+1} = y_n + \Delta t \sum_i \sum_k w_i f\left(y(t_k)h_k(t)\right). \tag{6-37}$$

Instead of deriving a polynomial that at certain points is tangent to the curve, i.e. the velocity is known, the concept is to find a solution such that the integral of the curve is computed directly. Thus, this is the major difference for the Runge-Kutta methods previously presented. Figure 6-3 shows a geometric interpretation for the mimetic method with the same case used for the Runge-Kutta method.

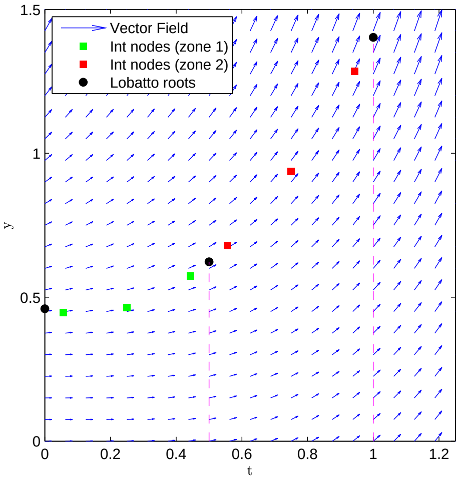

Figure 6-3: Mimetic integrator explained for $\dot{y} = t^2 + y^2$ with $\Delta t = 1$ and $y_0 = 0.46$

Figure 6-4 show the symmetric nature of the integrator. Consider a set of points that define the figure at image are transported. The symmetric nature, means that the transport by a vector field $v(x,t)$ after some Δt can be reverted by taking $v(x,-t)$. A more formal proof of the symplectic and symmetric nature of the integrator is left for future work.

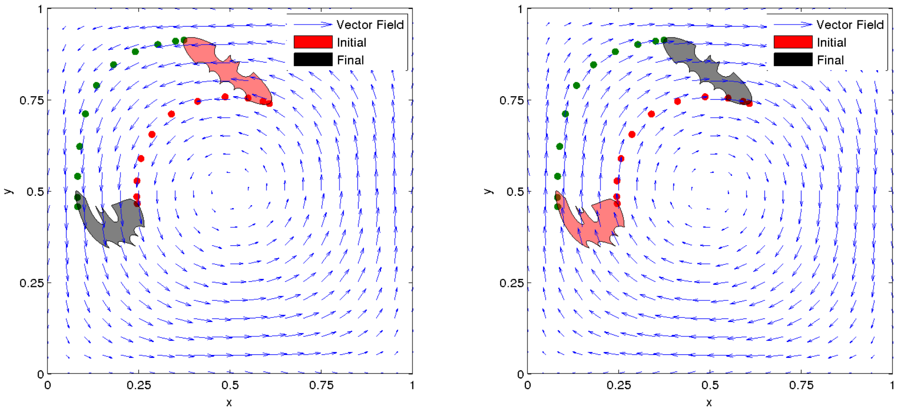

(a) Forward flow **(b)** Backward flow

Figure 6-4: Symmetry behavior of the mimetic integrator

6-4 Numerical Experiments

Along this section a set of numerical experiments are going to be performed. For all test cases the Hamiltonian is known and it should be preserved. Moreover, for the first test case the analytical solution for the position is also known.

6-4-1 Circle

A classical test is

$$H(p,q) = \frac{(q-q_0)^2}{2} + \frac{(p-p_0)^2}{2} \implies \begin{cases} \dot{p} = -q+1 \\ \dot{q} = p-1 \end{cases} \tag{6-38}$$

This has a known solution with a period of 2π given by,

$$p = \sqrt{R^2 sin(t + sin^{-1}\left(\frac{q_0-1}{R}\right)} + 1.0 \tag{6-39}$$

$$q = \sqrt{R^2 cos(t + cos^{-1}\left(\frac{p_0-1}{R}\right)} + 1.0 \tag{6-40}$$

where $R = (p_0-1)^2 + (q_0-1)^2$. Figure 6-5 shows a phase plot of the problem. Qualitatively it is clear that only the symplectic methods present a correct behavior.

Figure 6-6 shows the energy error for different time step and different orders of the method for a physical time of 100s, i.e. closely 16 turnovers. The solution is limit to time steps of the order of $\Delta t \leq 10^0$ for both methods. In this case, both method immediately converge to the exact energy.

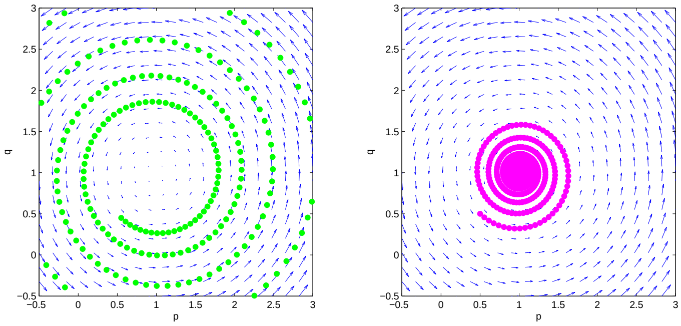

(a) Explicit Euler **(b)** Implicit Euler

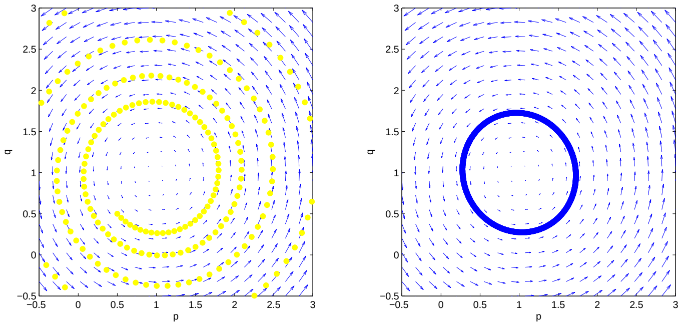

(c) 4th order explicit RK **(d)** Symplectic Euler

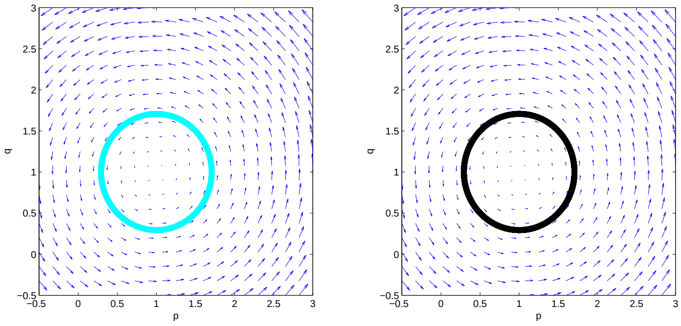

(e) Gauss ($s = 3$) **(f)** Mimetic ($p = 3$)

Figure 6-5: Circle phase plot for different integration schemes

Figure 6-7 shows the L^2 norm for the radius function of the time step and polynomial order after 100 seconds of simulation. In absolute values the mimetic method has always a lower error than the corresponding Gauss method. This difference increases when the order of the method increases. Furthermore, both methods present a spectral convergence.

Until this point all the analyses done concerned with the final result obtained after 100 seconds. Figure 6-8 shows the Hamiltonian and position error norm for the initial, final and

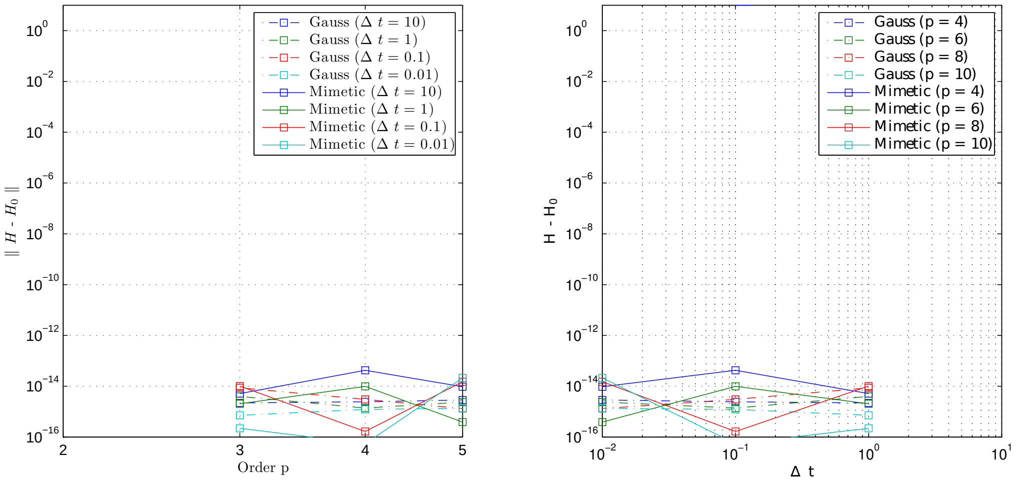

(a) Function of Order

(b) Function of Δt

Figure 6-6: Energy error of Gauss vs Mimetic for the circle problem

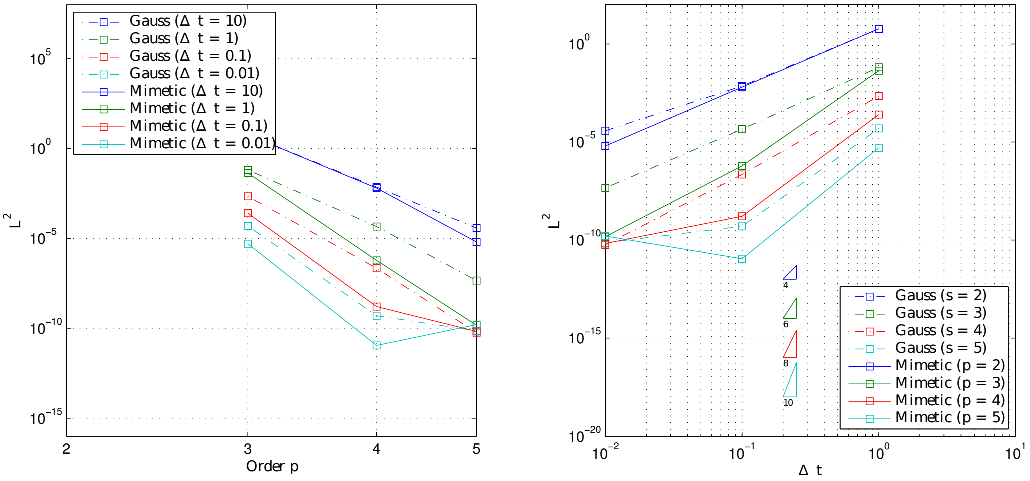

(a) Function of Order

(b) Function of Δt

Figure 6-7: L2 error of Gauss vs Mimetic for the circle problem

intermediate points were computations are performed for $\Delta t = 0.1$ and $s = p = 3$. Its clear that, although, for the initial and final time step the error is of the order of machine precision for both methods, this does not happen in the intermediate points in the case of the Gauss method. It is important to keep in mind that the intermediate points are not the same for both methods.

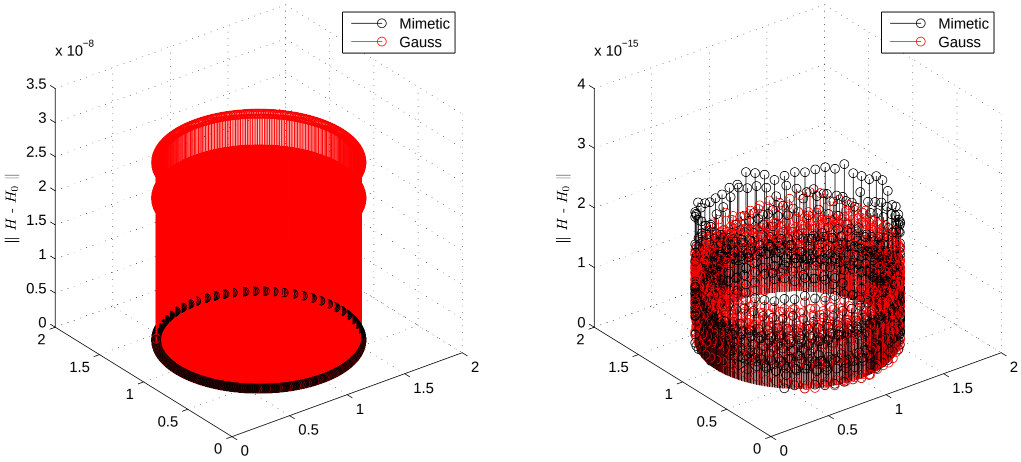

(a) All points **(b)** Final points

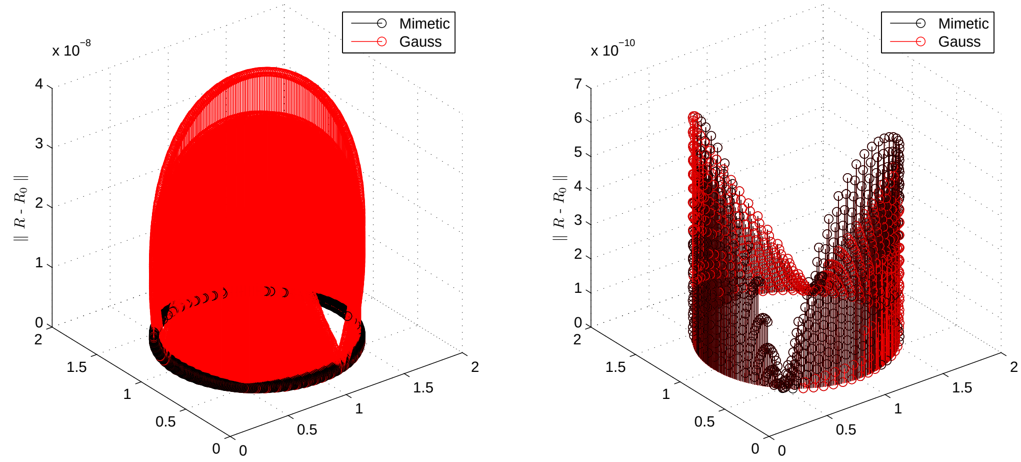

(c) All points **(d)** Final points

Figure 6-8: Hamiltonian and radius error of Gauss and mimetic method for the circle problem with $\Delta t = 0.1$ and $p = 3$

Figure 6-9 to Figure 6-11 shows the Hamiltonian and radius error function of the number of iterations for different polynomial order with time step respectively 0.01, 0.1 and 1. Although, the number of iterations for the Gauss method are higher this does not mean that the number of degrees of freedom correspond to this value, since the final points are computed based on the interior points. The high oscillatory nature of the figures is due to the fact that in the final points, i.e. the ones obtained after each time step, the Hamiltonian and the radius error are minimum. Moreover, as the time step decreases the absolute difference between the Gauss and Mimetic method decreases. However, it is clear that in the intermediate points the absolute error for the mimetic method is smaller than for the correspond Gauss method. This difference can be of two order of magnitude in the case of $\Delta t = 1$.

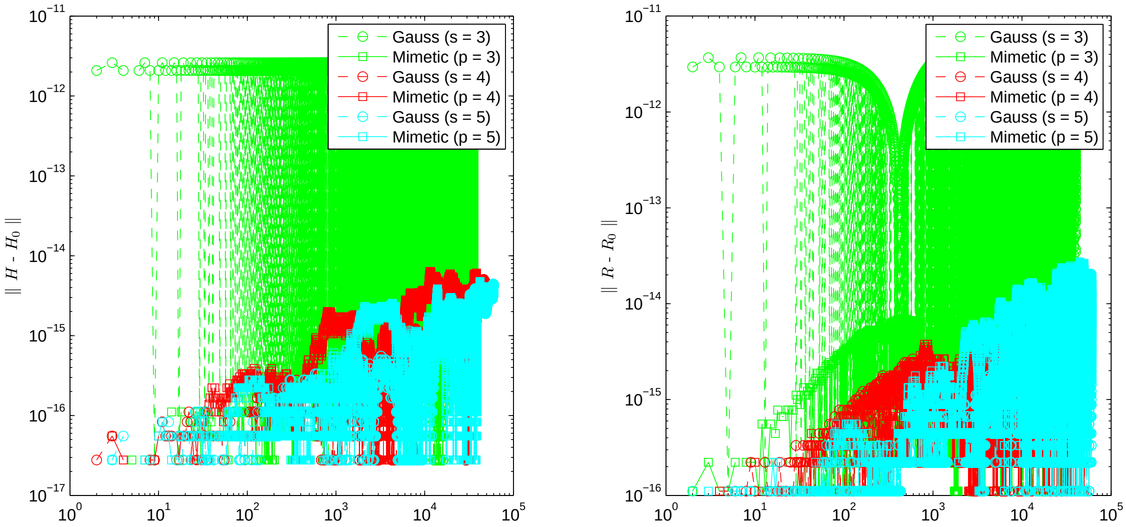

(a) Hamiltonian error

(b) Radius error

Figure 6-9: Hamiltonian and radius error of Gauss vs Mimetic for the circle with $\Delta t = 0.01$ for 100 seconds

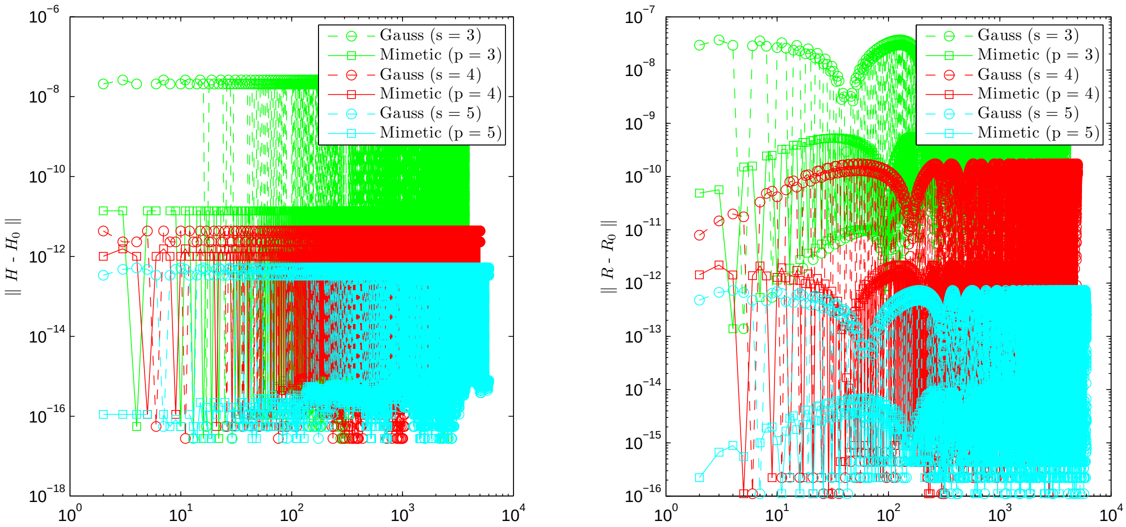

(a) Hamiltonian error

(b) Radius error

Figure 6-10: Hamiltonian and radius error of Gauss vs Mimetic for the circle with $\Delta t = 0.1$ for 100 seconds

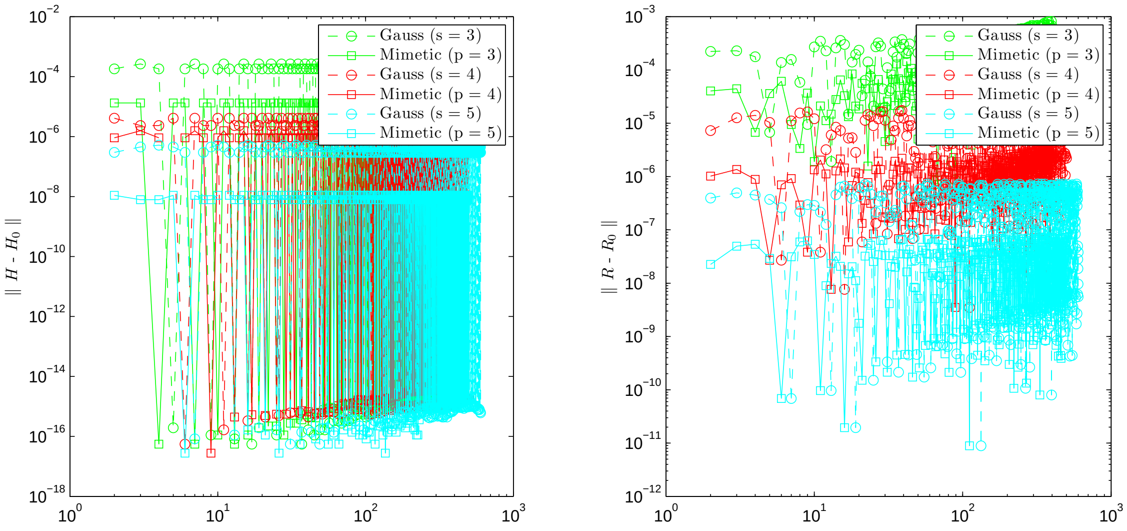

(a) Hamiltonian error **(b)** Radius error

Figure 6-11: Hamiltonian and radius error of Gauss vs Mimetic for the circle with $\Delta t = 1$ for 100 seconds

6-4-2 Harmonic oscillator

Taking the generalized coordinates α the Cartesian coordinates are given by

$$\begin{aligned} x &= lsin(\alpha) \\ y &= -lcos(\alpha). \end{aligned} \tag{6-41}$$

Then the kinetic and potential energy are given by,

$$\begin{aligned} T(x,y) &= \frac{1}{2}m(\dot{x}^2+\dot{y}^2) = \frac{1}{2}ml^2\dot{\alpha}^2 \\ U(x,y) &= mgy = -mglcos(\alpha). \end{aligned} \tag{6-42}$$

Thus, the Lagragian is given by,

$$ml^2\ddot{\alpha} + \frac{g}{l}sin(\alpha) = 0. \tag{6-43}$$

The mathematical pendulum (mass = 1, massless rod of length $l = 1$, gravitational acceleration $g = 1$) is a system of one degree of freedom having the Hamiltonian

$$H(p,q) = \frac{1}{2}p^2 - cos(q) \implies \begin{cases} \dot{p} = -sin(q) \\ \dot{q} = p \end{cases} \tag{6-44}$$

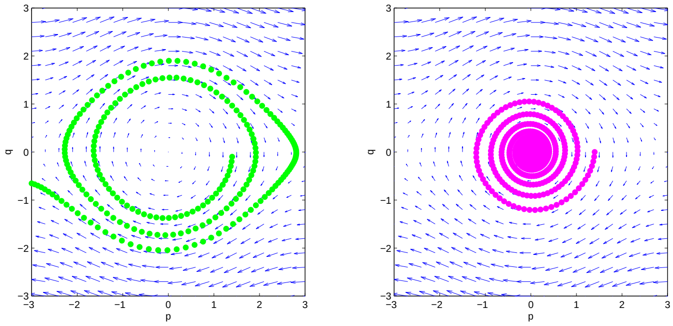

(a) Explicit Euler **(b)** Implicit Euler

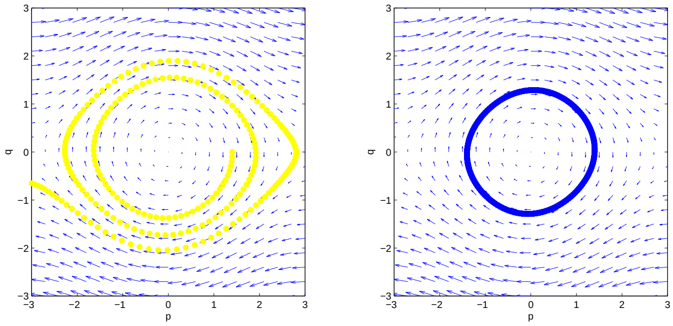

(c) 4th order explicit RK **(d)** Symplectic Euler

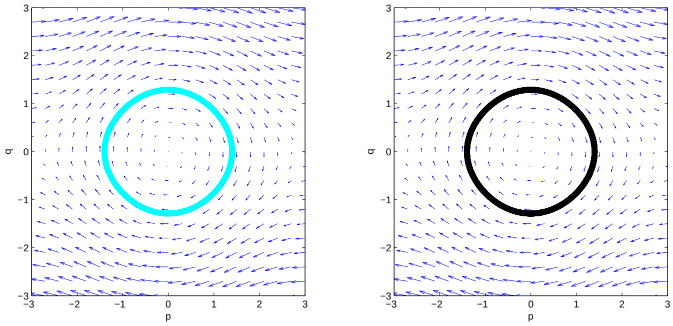

(e) Gauss ($s = 3$) **(f)** Mimetic ($p = 3$)

Figure 6-12: Phase plot of the pendulum problem for different integration schemes

Figure 6-12 is a phase-plot of the pendulum problem for the start point, $(x_0, y_0) = (0, 1.4)$. Qualitatively, the explicit Euler and the implicit Euler spirals outwards and inwards, respectively. The fourth order explicit Runge-Kutta does not conserve the total energy, therefore there is also a drift from the true value. On the other hand, it is clear that the symplectic Euler, Gauss and mimetic methods present a conservative behavior.

Figure 6-13 shows a comparison between different orders for the Gauss and the mimetic integrator after 100 seconds of simulation time. It is clear that with the same number of

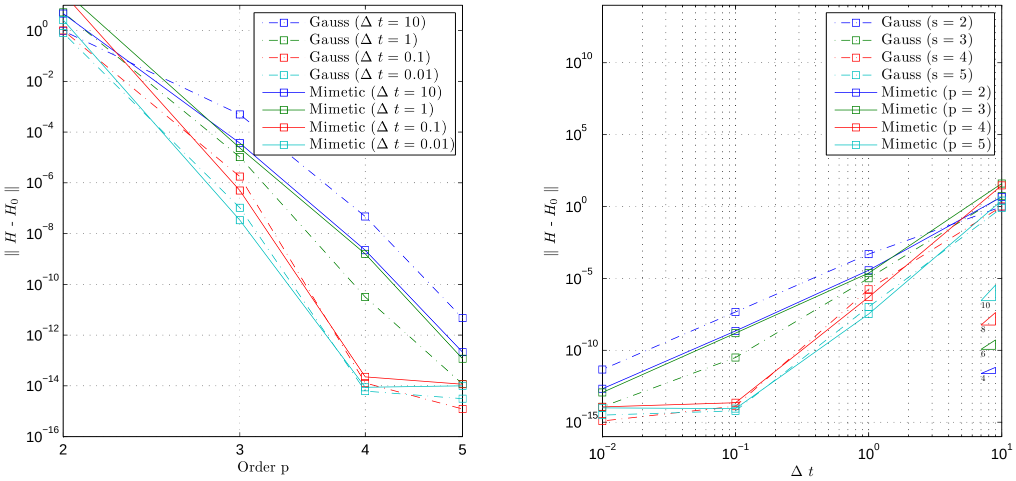

(a) Function of Order **(b)** Function of Δt

Figure 6-13: Gauss vs Mimetic for the pendulum problem after 10 seconds of physical time

degrees of freedom the mimetic method behaves has good as the gauss method in terms of energy error. Furthermore, both methods present a spectral convergence.

6-4-3 Lotka-Volterra model

This is a mathematical biology model that represents the growth of animal species. The real variable $u(t)$ represents the number of individuals of a certain specie at time t, the simplest assumption about its reproduction rate is $\frac{\partial u}{\partial t} = u\alpha$, where α leads to an exponential growth. In case of more species living together, the reproduction rates will also depend on the population numbers of the other species. For example, for two species, with $u(t)$ denoting the number of predators and $v(t)$ denoting the number of preys, the model relates then,

$$\dot{u} = u(v-2) \tag{6-45}$$

$$\dot{v} = v(1-u) \tag{6-46}$$

It turns out that dividing $\dot{u}$ by $\dot{v}$,

$$\frac{\dot{u}}{\dot{v}} = \frac{u(v-2)}{v(1-u)} \tag{6-47}$$

then by separation of variables [2],

$$\frac{1-u}{u}\dot{u} - \frac{v-2}{v}\dot{v} = 0, \tag{6-48}$$

or

$$\frac{d}{dt}I(u,v) = 0. \tag{6-49}$$

Integrating this equality the following invariant

$$I(u,v) = ln(u) - u + 2ln(v) - v, \tag{6-50}$$

where $I\left(u(t), v(t)\right) = cte$ for any time. Thus, every solution of the system lies on the this level curve. Furthermore, since these curves are closed all solutions are periodic. Until this point it might not be clear the Hamiltonian nature of the system. However, introducing the canonical coordinates $p = log(u)$ and $q = log(v)$ then the invariant $I(u,v)$ becomes,

$$H(p,q) = p - e^p + 2q - e^q. \tag{6-51}$$

Thus, the Lotka-Volterra equations become,

$$\begin{aligned} \dot{p} &= -u\frac{dH}{dq} = u(e^q - 2) = u(v-2) \\ \dot{q} &= v\frac{dH}{dp} = v(1-e^p) = v(1-u) \end{aligned} \tag{6-52}$$

Figure 6-14 shows a phase-plot with initial condition $(x_0, y_0) = (0.5, 0.5)$. It is clear that the model cycles through three stages. First, the number prey population increases, second, the predator population increases by feeding on the preys, and at last the predator population diminishes due to lack of food. The fourth order Runge-Kutta and the explicit and implicit Euler do not conserve "energy" has shown for the pendulum problem.

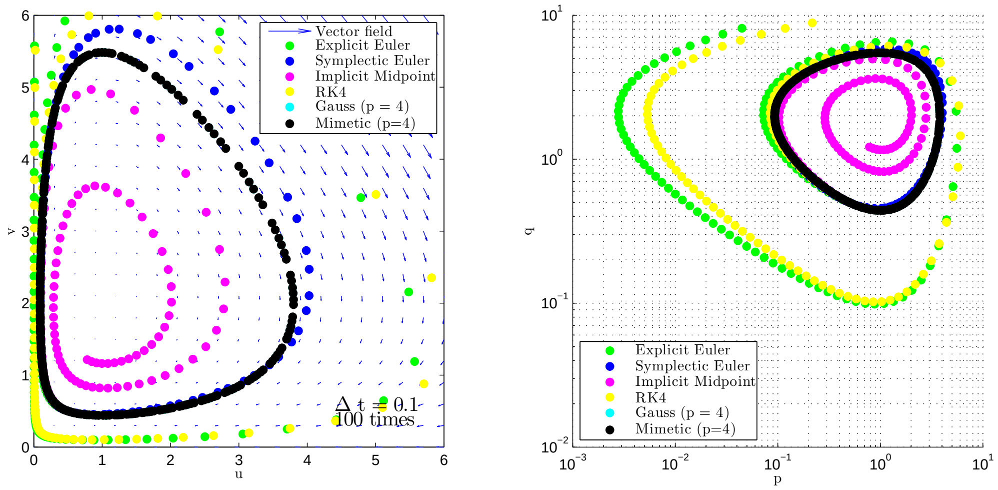

Figure 6-14: Lotka-Volterra phase plot

Figure 6-15 compares the Hamiltonian error for the mimetic and Gauss integrators function of the polynomial order and the time step for a simulation time of 100 seconds. As can be seen, the Gauss method does not converge when $\Delta t > 10^{-1}$. The reason for this might lie on the Newton iterative scheme used and future research might be done in this matter. However, using the same Newton scheme the mimetic method allows for larger time steps.

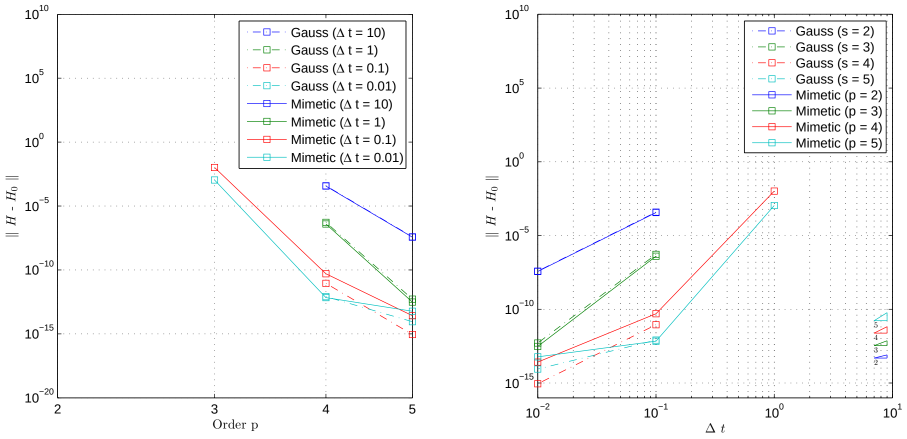

(a) Function of Order **(b)** Function of Δt

Figure 6-15: Gauss vs Mimetic for the Lotka-Volterra problem after 10 seconds

Figure 6-16 shows the energy error function of the number of iterations for the case with $\Delta t = 0.01$ after 100 seconds of physical time. Its observed that the error is bounded for all mimetic method and it is always smaller in absolute value than the corresponding order of the Gauss method. For the case where Gauss has $s = 2$ the error seems to be growing as a function of the number of iterations. This might be influenced by the Newton solver.

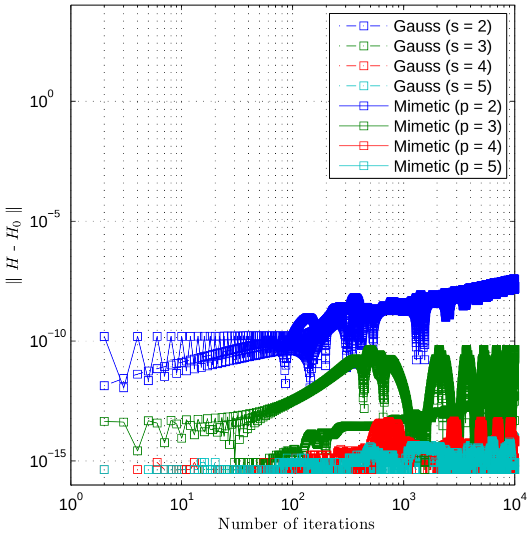

Figure 6-16: Hamiltonian error for the Lotka-Volterra problem function of number of iterations with $\Delta t = 0.01$

6-4-4 Rudman-Vortex

This Rudman-vortex is a vortical shearing vector field type. The velocity field is given by

$$u = Asin(\pi x)cos(\pi y) \quad v = -Acos(\pi x)sin(\pi y) \tag{6-53}$$

In all the following test cases $A = 1$. This velocity field will be used later when testing the 2D advection of differential forms. The Hamiltonian is given by,

$$H(x, y) = sin(\pi x)sin(\pi y) \tag{6-54}$$

Figure 6-17 shows the phase plot with initial position, $(x_0, y_0) = (0.8, 0.6)$. Besides the previous reported behavior for the explicit, implicit and fourth order Runge-Kutta, it is important to remark the difference between the symplectic Euler and the all other symplectic integrators shown. The exact path is a closer to the mimetic and the Gauss method than the symplectic Euler. Even thought, the Hamiltonian/energy is preserved. This translates that preserving energy does not mean that the solution for the position is correct.

Figure 6-18 represents a comparison between the Gauss and the mimetic integrator with respect to the Hamiltonian, i.e the energy error. Once again, both methods converge with spectral order $2p/2s$.

Figure 6-18c shows the error in energy function of the number of the number of iterations for, $\Delta t = 0.01$ after 100 seconds. The energy error is bounded for all cases. The mimetic method has always a smaller absolute error than the Gauss method. However, this difference decreases as the the order of the method increases.

6-4-5 Two-body Kepler problem

Kepler first law, predicts the motion of two bodies attracting to each other

$$r = \frac{d}{1 + ecos(\phi)} = a + aecos(E) \tag{6-55}$$

where a is the great axis, e the eccentricity, $b = a\sqrt{1-e^2}$, $d = b\sqrt{1-e^2} = a(1-e^2)$, E the eccentric anomaly and that $r^2\dot{\phi} = cte.$

For computing the motion of two bodies which attract to each other, one can use the two-dimensional coordinates $q = (q_1, q_2)$ and the following differential equations are obtained,

$$\ddot{q_1} = -\frac{q_1}{(q_1^2 + q_2^2)^{\frac{3}{2}}} \ , \ddot{q_2} = -\frac{q_2}{(q_1^2 + q_2^2)^{\frac{3}{2}}} \tag{6-56}$$

This is equivalent to a Hamiltonian system with the Hamiltonian,

$$H(p_1, p_2, q_1, q_2) = \frac{1}{2}(p_1^2 + p_2^2) - \frac{1}{\sqrt{q_1^2 + q_2^2}} \ , p_i = \dot{q}_i \tag{6-57}$$

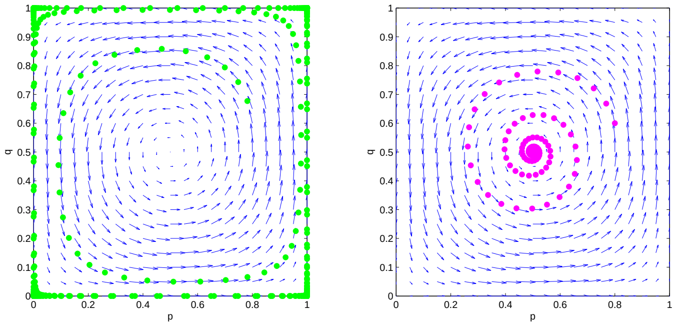

(a) Explicit Euler

(b) Implicit Euler

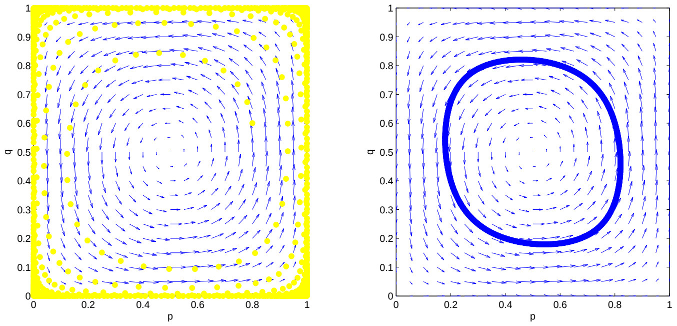

(c) 4th order explicit RK

(d) Symplectic Euler

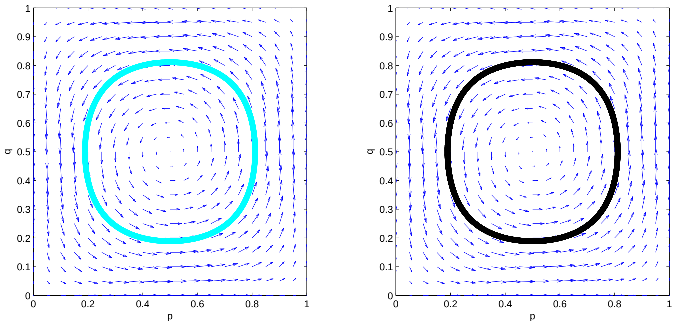

(e) Gauss $(s = 3)$

(f) Mimetic $(p = 3)$

Figure 6-17: Phase plot for the Rudman-Vortex problem with different integration schemes

The problem (6-56) will be computed with $0 \leq e \leq 1$, with the initial values

$$q_1(0) = 1 - e \ , \ q_2(0) = 0, \ , \ \dot{q}_1(0) = 0 \ , \ \dot{q}_2(0) = \sqrt{\frac{1+e}{1-e}}$$

This implies that

$$H_0 = -1/2 \ , \ L_0 = \sqrt{1-e^2} \ , \ d = 1 - e^2 \text{ and } Period = 2\pi$$

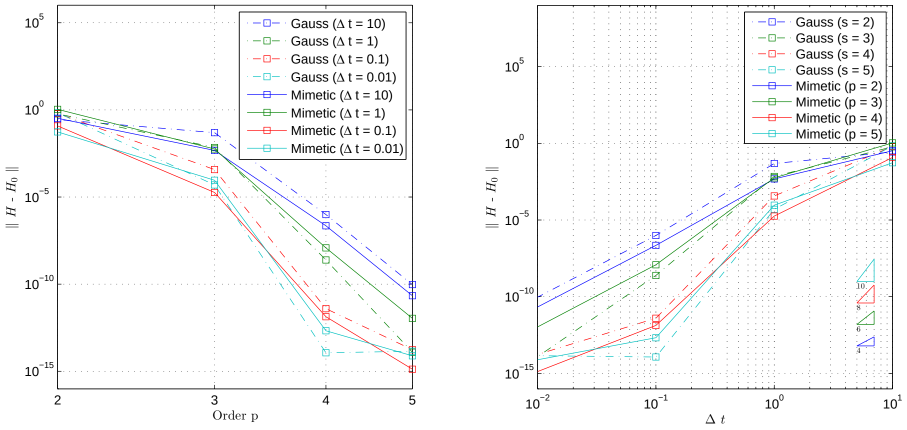

(a) Function of Order

(b) Function of Δt

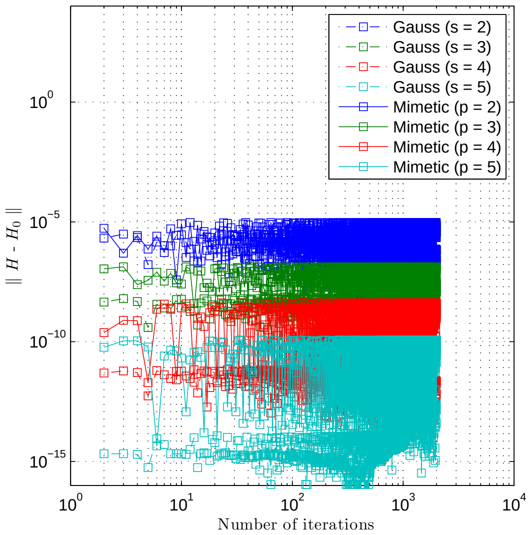

(c) Function of number of iterations

Figure 6-18: Gauss vs Mimetic for the Rudman-Vortex problem

Figure 6-19 represents the (q_1, q_2) plot for the Kepler problem with $e = 0.6$ after 200 seconds. The mimetic integrator performs as good as the Gauss method. Once again, the explicit Euler completely drifts from the exact solution. Furthermore, the symplectic Euler and the implicit mid-point have a precession effect that disturbs the solution clockwise and anti-clockwise, respectively.

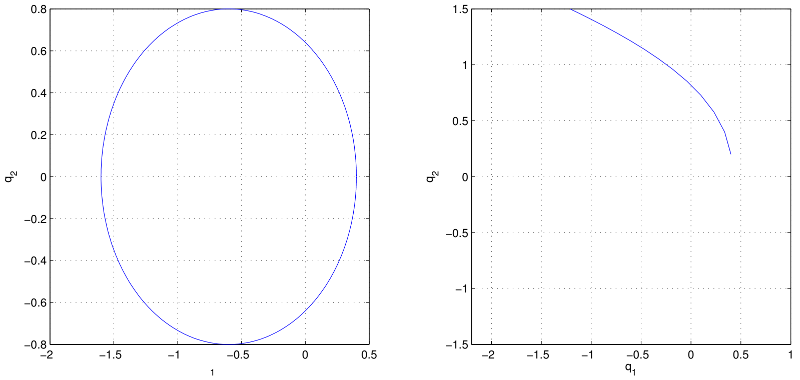

(a) Exact **(b)** Explicit Euler

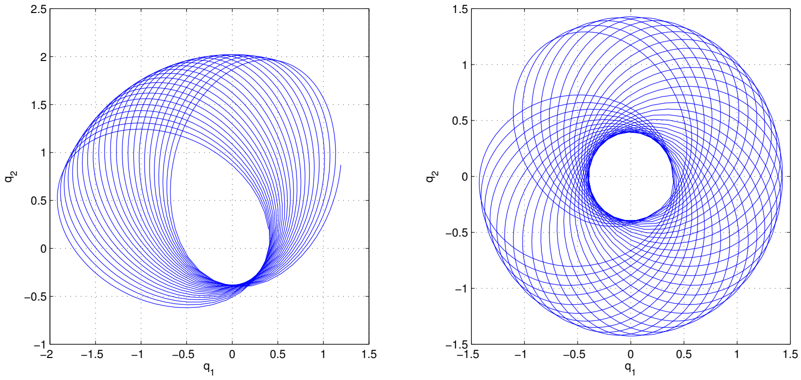

(c) Symplectic Euler **(d)** Stormer-Verlet

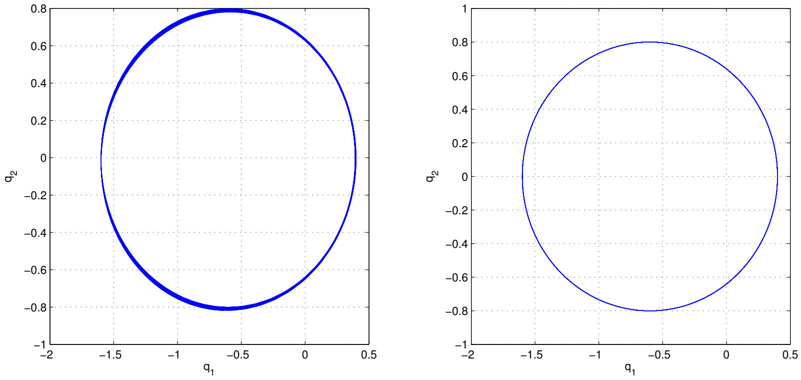

(e) Gauss **(f)** Mimetic

Figure 6-19: Kepler $(q_1.q_2)$ plot for 2000 $steps$ with $\Delta t = 0.1$

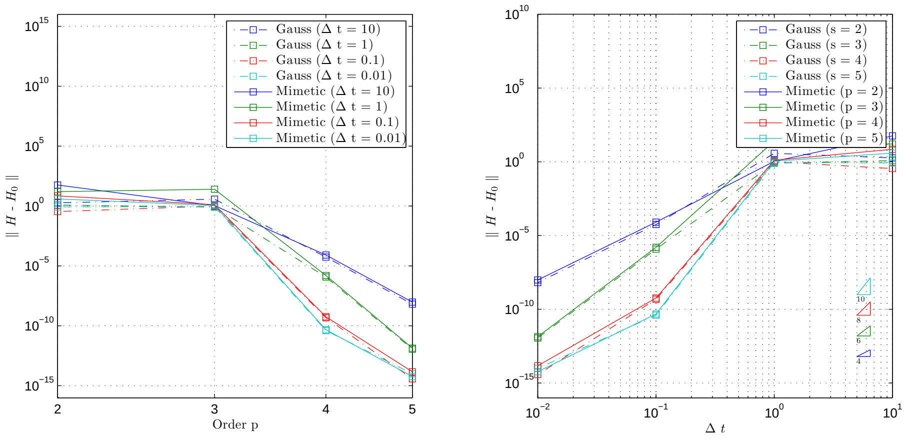

(a) Function of Order **(b)** Function of Δt

Figure 6-20: Energy error of Gauss vs Mimetic for the Kepler problem

6-4-6 Perturbed Kepler problem

Consider a perturbed Kepler problem with the following Hamiltonian,

$$H(p,q) = \frac{1}{2}(p_1^2 + p_2^2) - \frac{1}{\sqrt{q_1^2 + q_2^2}} - \frac{\mu}{3\sqrt{(q_1^2 + q_2^2)^3}} \tag{6-58}$$

where μ is the perturbation. Therefore, the system is represented by the following differential equations,

$$\begin{aligned} \dot{q}_1 &= p_1, & \dot{p}_1 &= -\frac{q_1}{(q_1^2 + q_2^2)^{3/2}} - \frac{\mu q_1}{(q_1^2 + q_2^2)^{5/2}} \\ \dot{q}_2 &= p_2, & \dot{p}_2 &= -\frac{q_2}{(q_1^2 + q_2^2)^{3/2}} - \frac{\mu q_2}{(q_1^2 + q_2^2)^{5/2}} \end{aligned} \tag{6-59}$$

The following numerical examples are computed with for a perturbation, $\mu = 0.015$ and with initial values,

$$q_1(0) = 1 - e, \quad q_2(0) = 0, \quad p_1(0) = 0, \quad p_2(0) = \sqrt{\frac{1+e}{1-e}}$$

where the eccentricity, $e = 0.6$.

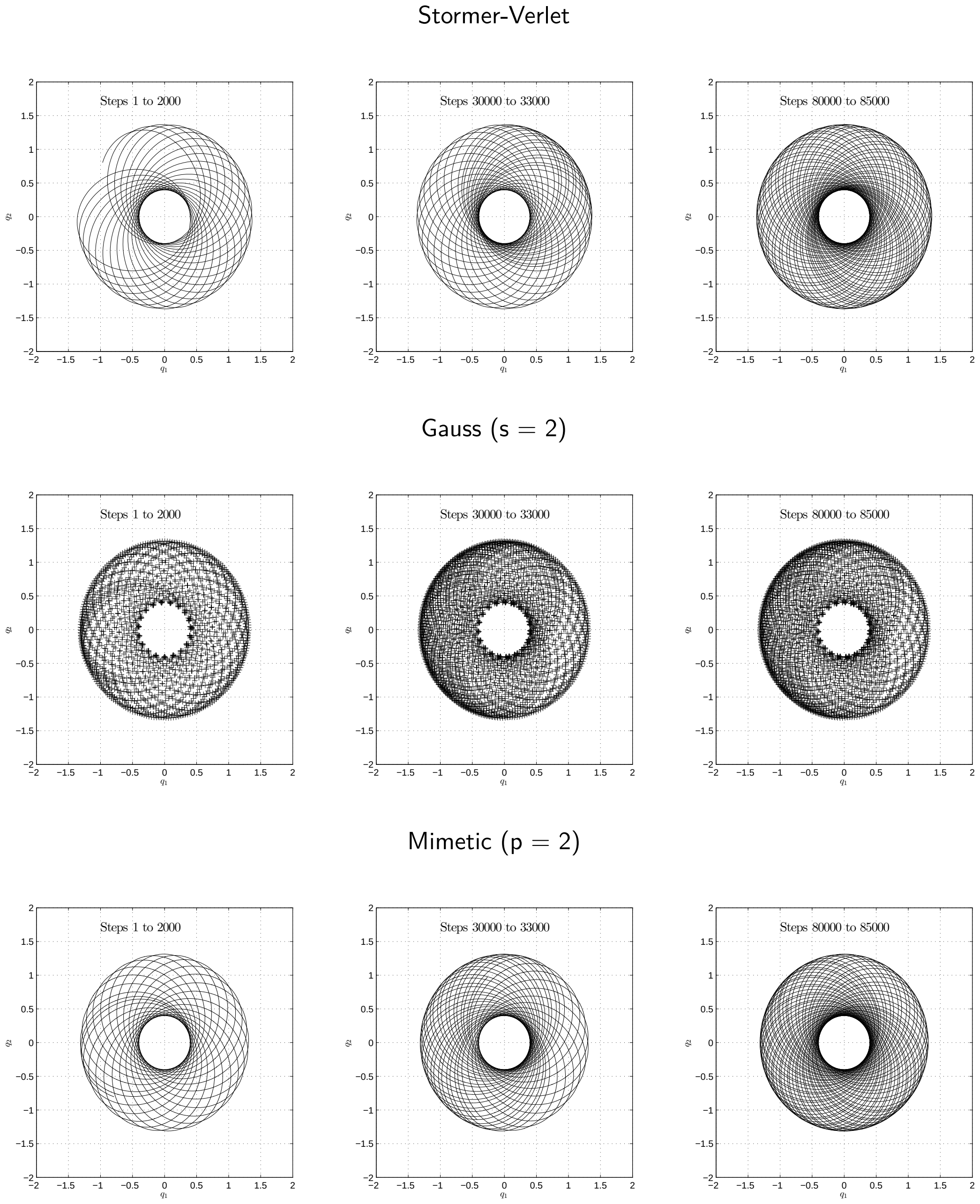

Figure 6-21: Plot (q_1, q_2) for the perturbed Kepler problems with constant step size, $\Delta t = 0.065$

Figure 6-21 shows the (q_1, q_2) plot of the perturbed Kepler problem for three different parts of the integration for the $\Delta t = 0.065$. Similar results for low order symplectic integrator were reported in [2].

6-4-7 Outer solar system

The same reasoning applied to the two-body Kepler problem can be extended to the motion of the five outer planets relative to the sun. The problem is an Hamiltonian system with,

$$H(p,q) = \frac{1}{2}\sum_{i=0}^{5}\frac{1}{m_i}p_i^T p_i - G\sum_{i=1}^{5}\sum_{j=0}^{i-1}\frac{m_i m_j}{||q_i - q_j||} \tag{6-60}$$

Here p and q are the vectors containing the momenta and positions respectively. The masses are relative to the sun, $m_0 = 1.00000597682$ to take into account the inner planets. The distances are in astronomical units. Time is taken in Earth days and the gravitational constant is $G = 2.95912208286\dot{1}0^{-4}$. The initial conditions are given in Appendix C.

Figure 6-22 shows a phase plot for the outer solar system. For the explicit Euler method the energy spirals outwards. On the other hand, for the implicit Euler method the planets fall into the sun and thrown far away. The rest of the integrators are symplectic and show the correct behavior.

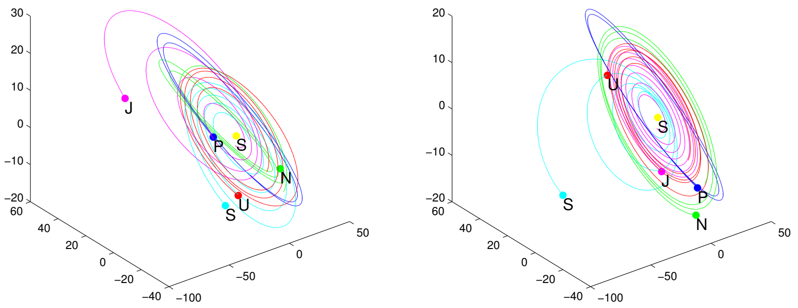

(a) Explicit Euler

(b) Implicit Euler

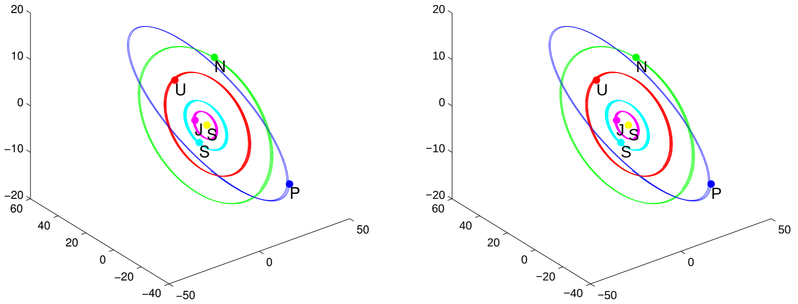

(c) Stormer/Verlet

(d) Symplectic Euler

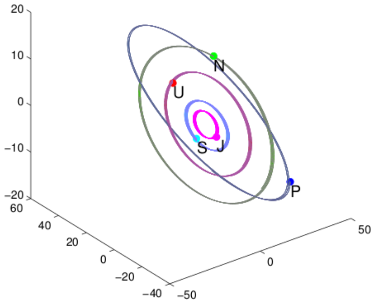

(e) Mimetic

Figure 6-22: Outer solar system phase plot. $\Delta t = 100$, $2000 steps$

Chapter 7

Discrete generalized advection

Several techniques have been proposed to solve the advection problem. These can be divided into three major groups: *Lagrangian*, *Eulerian* and *Semi-Lagrangian*. The first group, *Lagrangian*, have the coordinate system "attached" to the medium under consideration and move along with it. Particles (representing fluid molecules [54]) or a mesh (representing the surface of some object [55]) moving along the flow are examples of schemes derived based on this principle. On the other hand, *Eulerian* schemes, use a fixed coordinate system. Common schemes that use this ideas are for instance finite volume or finite element methods. The last group, *Semi-Lagrangian* or *Eulerian-Lagrangian*, combine a Lagrangian tracking algorithm along characteristic lines while keeping the convenience of a fixed computational grid.

Any of these method as advantageous and disadvantageous. For example, tracking of surfaces is easier with Lagrangian methods while Eulerian methods tend to introduce artificial diffusion due to the fixed nature of the computational mesh. On the other hand, large deformations in the mesh system can lead to numerical problems in the Lagrangian schemes. Furthermore, in the case of Eulerian methods it is necessary to derive a temporal discretization scheme that is able to geometrically preserve spatial quantities in time.

Along the previous Chapter it was mentioned that important symmetries and invariants, such as mass, volume, momentum, energy, etc, should be preserved independent of the order of the method used. Furthermore, in the case of Hamiltonian systems the symplectic structure plays an important role. Along this Chapter semi-Lagrangian and Eulerian methods combined with the mimetic integrator are derived for the generalized convection problem by discretizing the Lie derivative. Section 7-1 introduces the pure Lagrangian schemes. Afterwards, Section 7-2 will introduce advection through semi-Lagrangian methods based on the dynamic perspective of the Lie derivative. Finally, Section 7-3 introduces the Eulerian schemes for the discretization of the advection of differential forms using the algebraic definition of the Lie derivative.

7-1 Lagrangian

Theoretically, the Lagrangian methods are well suited for advection problems. But in practice, stretching and shearing of the original fluid particles distort the mesh after a few time steps. Thus, these methods are rarely used. Figure 7-1 shows a mesh of different polynomial order being advected by the Rudman-vortex velocity field. It is clear that after some time steps the mesh quality is completely deteriorated.

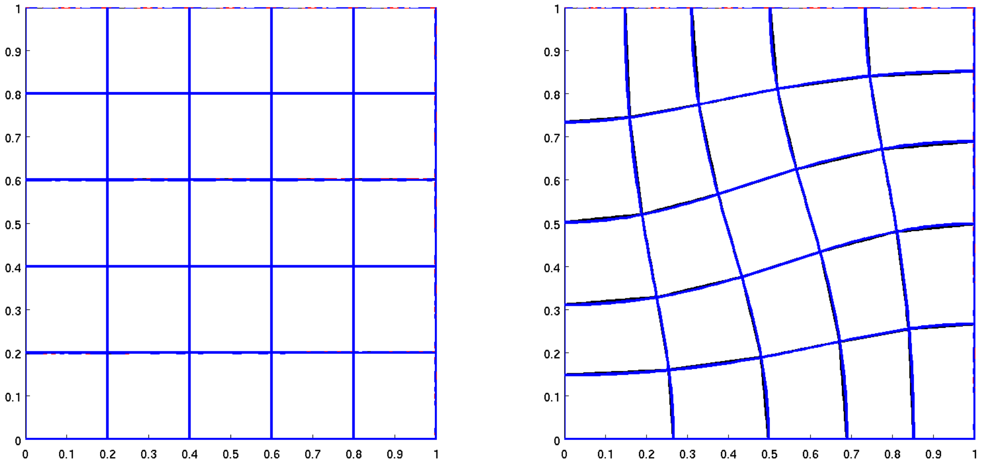

(a) t = 0 seconds **(b)** t = 1 second

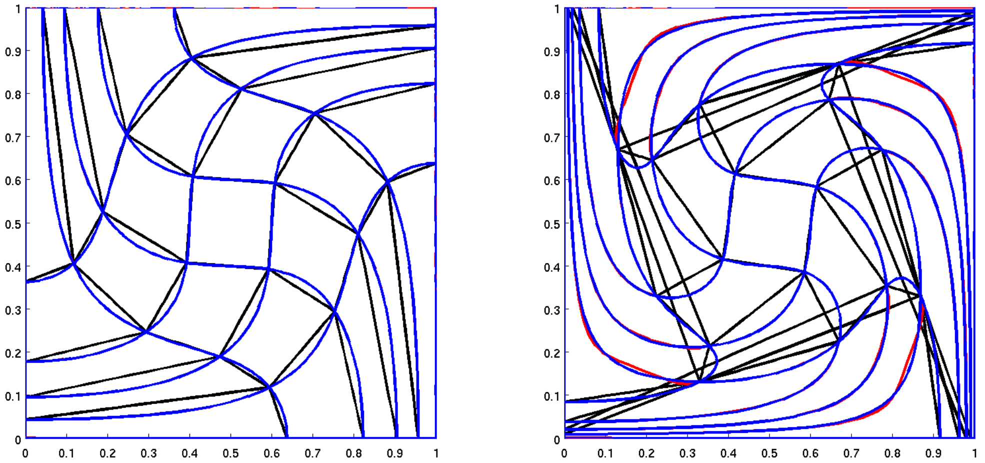

(c) t = 5 second **(d)** t = 10 second

Figure 7-1: Lagragian mesh movement (p = 1; p = 4; p = 30);

7-2 Semi-Lagrangian

Semi-Lagragian or Eulerian-Lagrangian schemes are a large class of methods applied in CFD. firstly introduced in the 50s and 60s to model weather forecasting [56]. They are based on a Lagrangian tracking algorithm along the characteristic lines. Points from within the Eulerian grid are tracked backward along the characteristic over the time step, forming a Lagrangian grid. Numerical information from the previous time level is projected from the background Eulerian grid onto the Lagrangian grid.

A clear advantage of these methods is the relaxation of the CFL restriction. Moreover, the intrinsic connection between spatial and temporal discretization is expectable to reduce the error significantly. Because of what they promise several semi-Lagragian schemes have been proposed [57, 58, 59, 60]. However these schemes mainly deal with scalar fields with the exception of the recent [21].

Recalling the dynamic definition of the Lie Derivative,

$$\pounds_{\mathbf{V}}\alpha = \left.\frac{d}{dt}\right|_{t=0} \int_{\Omega_t} \alpha = \left.\frac{d}{dt}\right|_{t=0} \Phi_t^{\star}\alpha^k, \tag{7-1}$$

where $\Phi_t^{\star}$ is the pullback induced by the flow of the velocity field $\mathbf{V}$. If the position of a fluid element at time t, which was (or will be) at $\mathbf{x}$ at time s, is denoted by $\mathbf{X}\left(\mathbf{x}, s; t\right)$. Then the characteristic curves of this equation, along which ρ remains constant, are defined by,

$$\frac{d\mathbf{X}}{dt}\left(\mathbf{x}, s; t\right) = \mathbf{V}\left(\mathbf{x}, s; t\right), \tag{7-2}$$

with $\mathbf{X}\left(\mathbf{x}, s; s\right) = \mathbf{x}$. After computing the characteristics from (7-2), the solution of the advection equation is given by

$$\rho\left(\mathbf{X}\left(\cdot, t; t+\tau\right), t+\tau\right) = c\left(\cdot, t\right), \tag{7-3}$$

where τ is a time interval. When discretized in time with a time step Δt, $t^n = n\Delta t$, the characteristics can used to define,

$$\mathbf{x} = \mathbf{X}\left(\mathbf{y}, t^{n+1}; t^n\right), \tag{7-4}$$

and

$$\mathbf{y} = \mathbf{X}\left(\mathbf{x}, t^n; t^{n+1}\right). \tag{7-5}$$

The points $\mathbf{x}$ and $\mathbf{y}$ represent the departure point at time t^n and the arrival point at time t^{n+1}, respectively. If a set of quadrature points are backtracked following this approach the values of the the respective integral can be computed. Two methods are proposed, the path tube and flux backtrack. For the first one the quadrature points are collocated at the t^{n+1} and then backtracked to t^n. For the flux backtrack the quadrature points are collocated along the common faces in time where the exchange between cells occurs. Figure 7-2 and Figure 7-3 give a geometric representation of the flux backtrack and the path tube method, respectively. It is clear that both methods are computationally expensive because they require the solution of a system of ODE for each integration point. However, each element or face is independent from its pairs so the method can be easily parallelized making it more efficient.

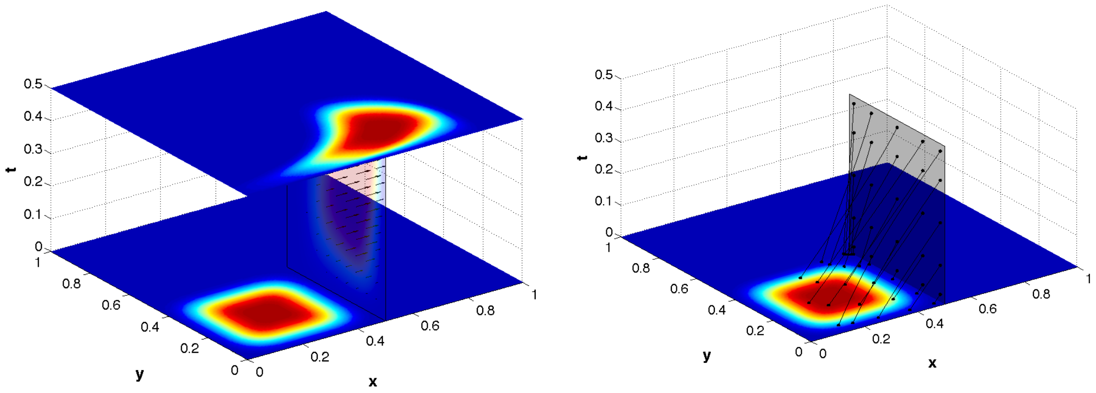

Figure 7-2: Flux backtrack method

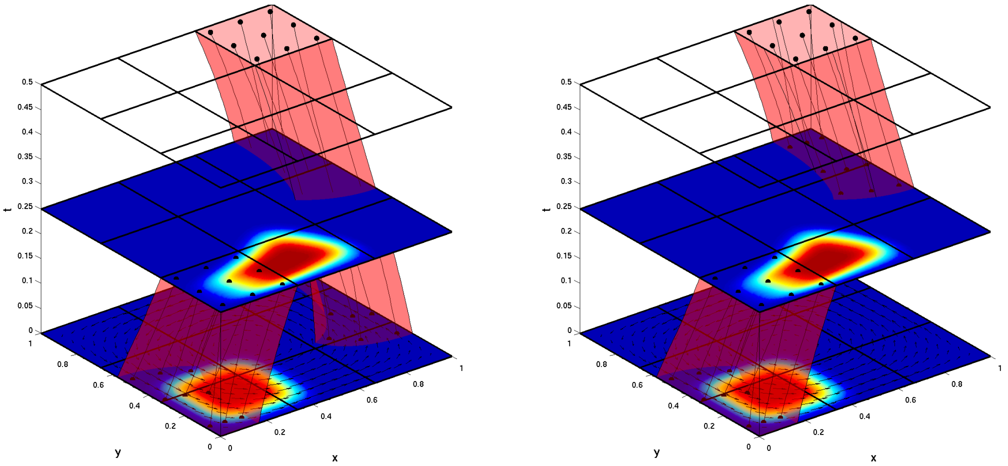

(a) No restart **(b)** Restart every time step

Figure 7-3: Path tube method

From this point on numerical experiments for both 1D and 2D test cases are presented for both methods. For the 1D test case a constant velocity vector field of, $\mathbf{v} = 1$, is considered with periodic boundary conditions and an initial 1-form $\rho^1 = sin\,(2\pi x) + 1dx$. The total physical time of simulation is of 10 seconds, which corresponds of 10 turns of the system.

The analytical solution is computed considering the equation,

$$\frac{\partial \rho}{\partial t} + \bar{u}\frac{\partial \rho}{\partial x} = 0 \quad \rho(0,x) = \rho_0(x). \tag{7-6}$$

The solution is given in the form,

$$\rho(t,x) = \rho_0(x - \bar{u}t). \tag{7-7}$$

Consider an auxiliary variable, $z = x - \bar{u}t$. Thus,

$$\begin{aligned} \frac{\partial \rho}{\partial z}\frac{\partial z}{\partial t} + \bar{u}\frac{\partial \rho}{\partial x} &= 0 \\ \rho_0'(x-\bar{u}t)(-\bar{u}) + \rho_0'(x-\bar{u}t) &= 0. \end{aligned} \tag{7-8}$$

Figure 7-4 presents the solution and the error for different physical times with $N = 100$ and $p_x = 10$, this is the best space space discretization computed and $\Delta t = 0.01$.

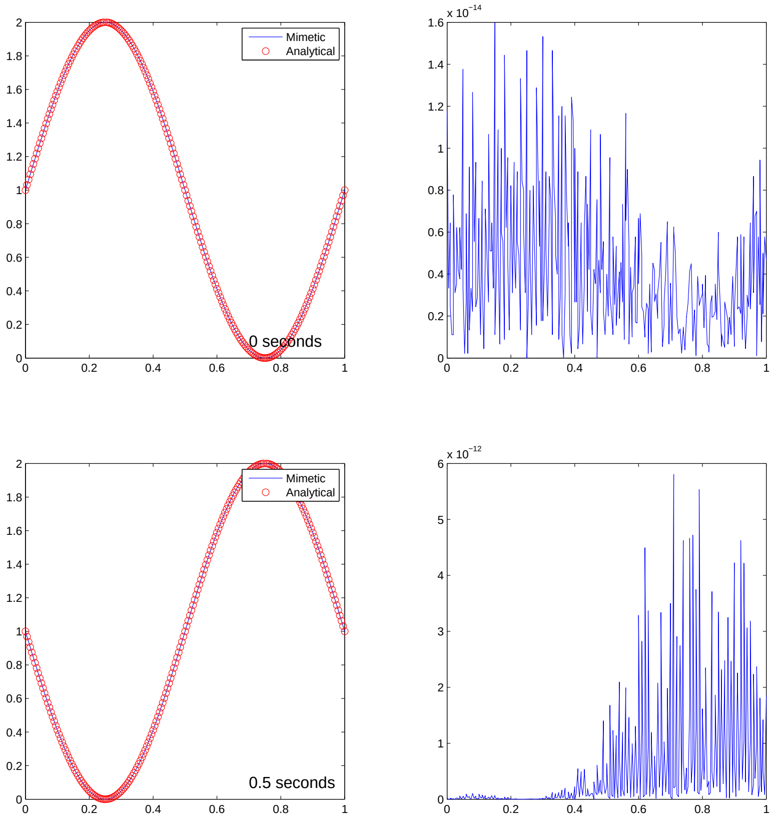

Figure 7-4: Comparison between the 1D advection of a 1-form, $sin(2\pi x) + 1dx$, with the analytical solution for the path tube method

First of all, Figure 7-5 and Figure 7-6 show the space time advection of the solution and the error for the flux backtrack and the path tube method with $N = 100$ and $p_x = 10$, respectively.

Both methods, qualitatively, present a long term accurate behavior. Furthermore, looking at the error it is clear that the path tube method as a slightly better performance.

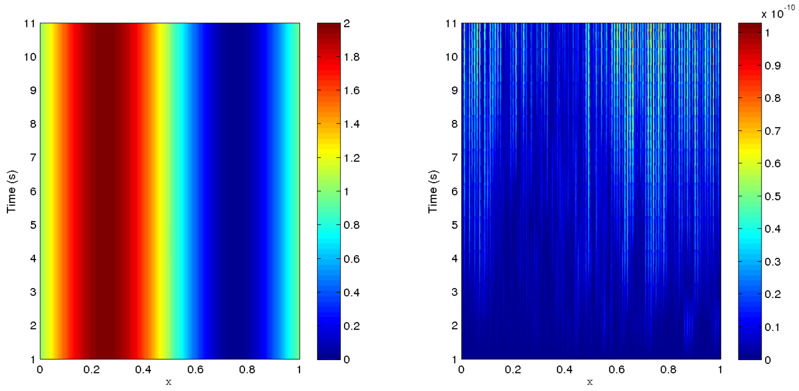

(a) $\Delta t = 1$

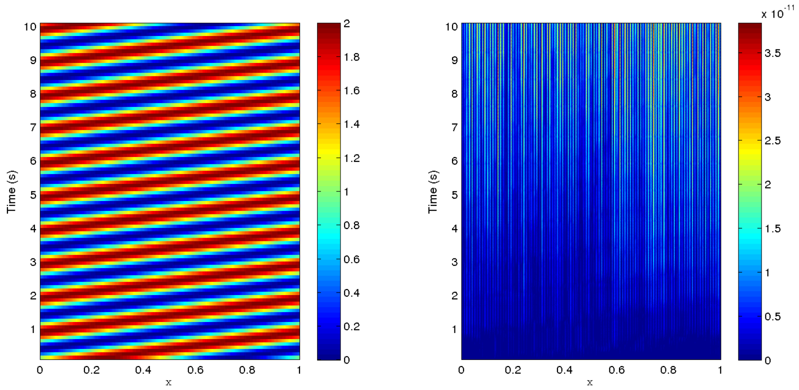

(b) $\Delta t = 10^{-1}$

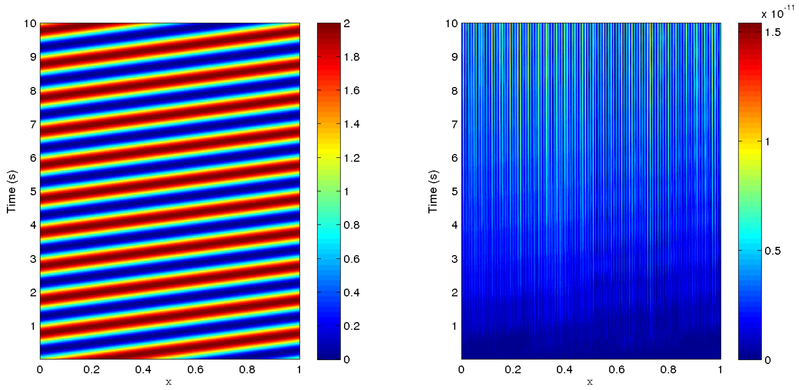

(c) $\Delta t = 10^{-2}$

Figure 7-5: Space-time 1D advection of a 1-form, $sin(2\pi x) + 1dx$ by the flux backtrack method

Figure 7-7 shows the L^2 error for the path tube method selecting $N = 100$ and a polynomial order in space of $p_x = 10$. The goal is to minimize the spatial error and only evaluated the

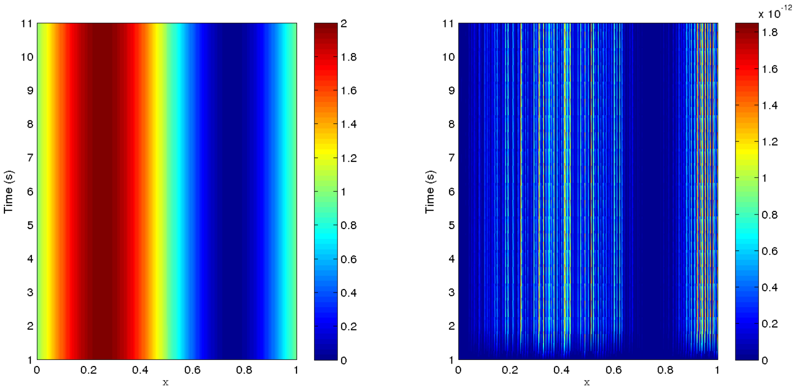

(a) $\Delta t = 1$

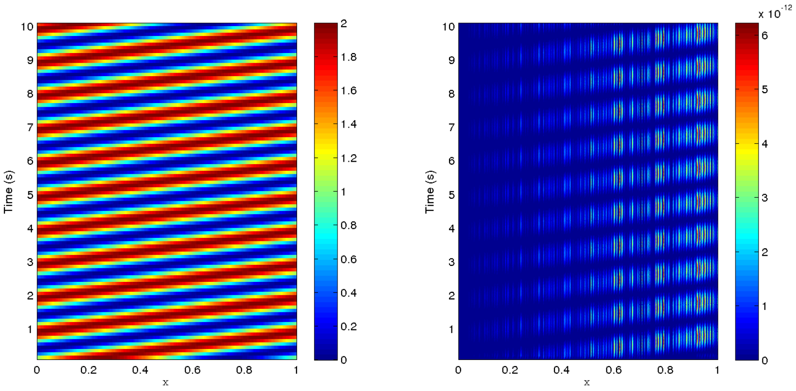

(b) $\Delta t = 10^{-1}$

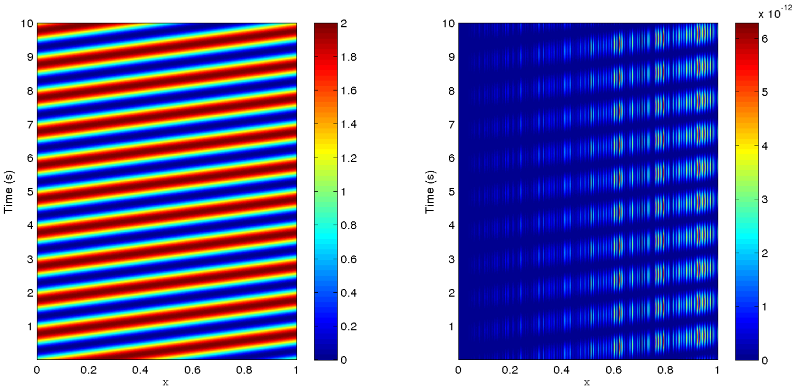

(c) $\Delta t = 10^{-2}$

Figure 7-6: Space-time 1D advection of a 1-form, $sin(2\pi x) + 1dx$ by the path tube method

contributions from the influence of the change of Δt and the polynomial order in time. It is clear that for the 1D case the contribution of this to factor is practically non existent since the L^2 error is constant around 10^{-11}. Although, the L^2 error is small it does not reach the zero machine.

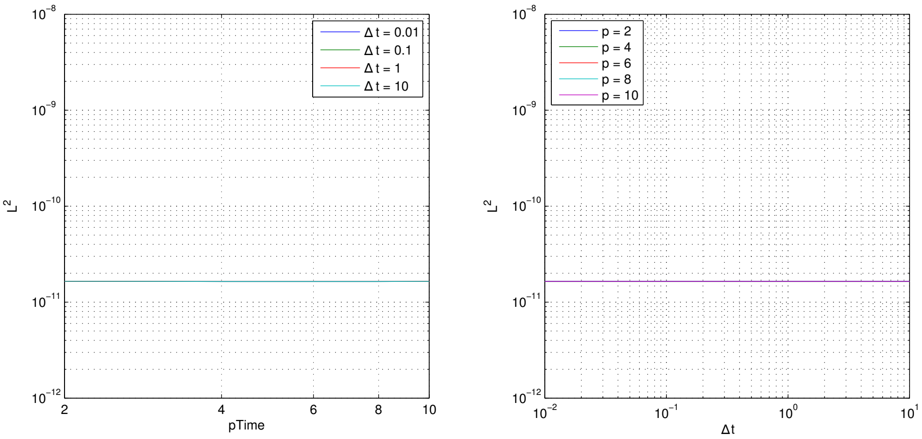

Figure 7-7: L^2 error of the path tube method for $N = 100$ with $p_x = 10$

The reason for that is the accumulation of error from integration between discontinuous functions, i.e. some integrations points are in one element other in the adjacent one something that quadrature does not tolerate properly, because of the discontinuity among adjacent elements. An example is given in Figure 7-8. This effect will have more profound consequences in 2D.

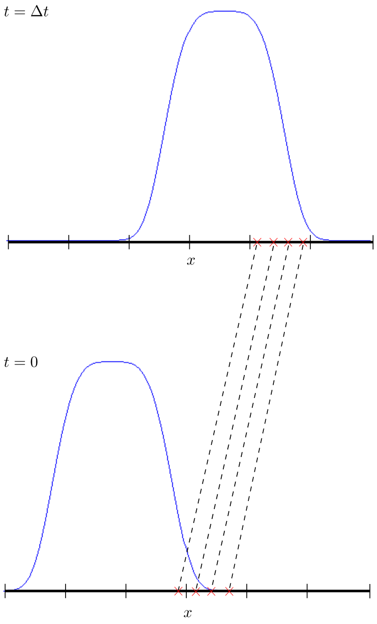

Figure 7-8: Integration error for semi-Lagrangian methods in 1D

Figure 7-9 shows the the L^2 error for $\Delta t = 0.01$ (this is the smallest time step computed) and a polynomial order for the ODE solver of $p_t = 10$. The aim is to reduce the time contribution for the error. It is clear that as the mesh size is decreased, i.e. the number of elements increases, spectral convergence with the space polynomial order is obtained.

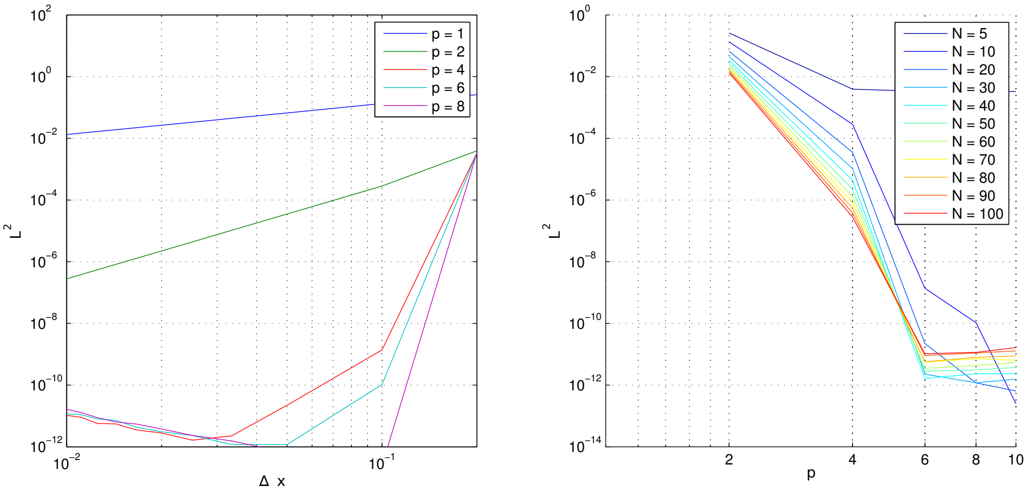

Figure 7-9: L^2 error of the path tube method for 10 seconds with $\Delta t = 0.01$

At this point it is important to do the same analysis for in the case of the flux backtrack method. Figure 7-10 plots the L^2 error for the case with the best spacial conditions computed, i.e $N = 100$ and $p_x = 10$. One clear difference to the path tube method, is that the backtrack flux does not cope a $\Delta t = 10$. Moreover, the absolute L^2 error is in the order of 10^{-10} slightly higher than the path tube method, this once again regards an integration error. On the other hand, as seen in the path tube method there is no convergence function of the Δt or the polynomial order in time.

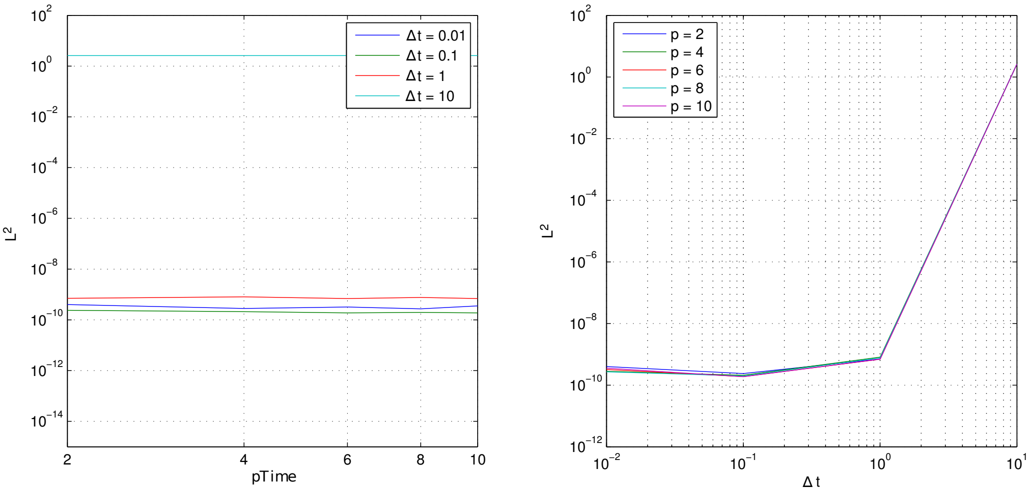

Figure 7-10: L^2 error of the flux backtrack method for $N = 100$ with $p_x = 10$

Figure 7-11 represents the L^2 error for the backtrack flux method with the best time discretization available, i.e. $\Delta t = 0.01$ and $p_t = 10$. It is clear that as the mesh size decreases the L^2 error decreases with spectral convergence with space polynomial order. However, the absolute value for which the convergence is obtained is around 10^{-10}. The reason for this is once again the integration error that occurs and pollutes the solution.

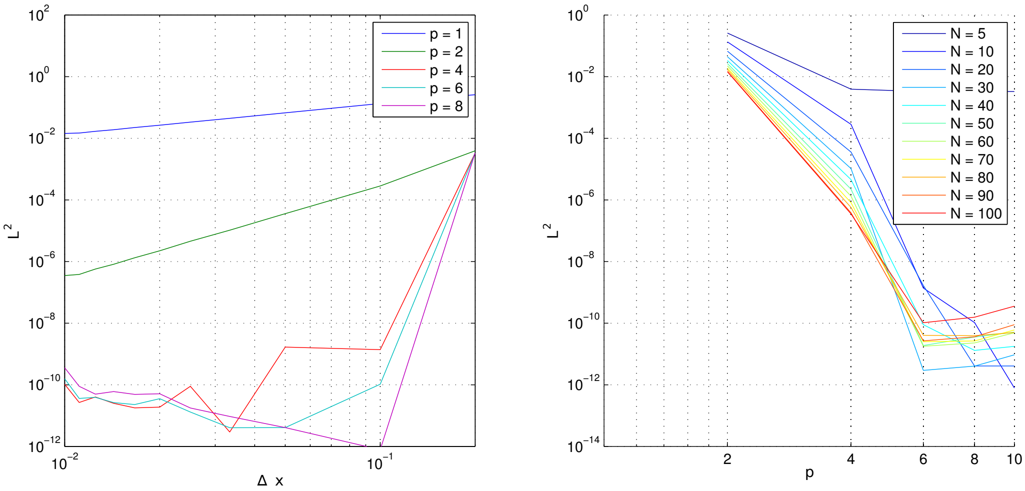

Figure 7-11: L^2 error of the flux backtrack method for $\Delta t = 0.01$

At this stage it is important to analyze the results obtained for 2D. The velocity vector field used is the Rudman-vortex, presented along Chapter 6, given by,

$$\mathbf{u} = sin(\pi x)cos(\pi y) \quad \mathbf{v} = -cos(\pi x)sin(\pi y). \tag{7-9}$$

An interesting feature of this vector field is that there are no normal components along the boundary, i.e. there is no in/out flow across the boundaries. Therefore, the initial mass that is in the system should be preserved. Furthermore, the initial 2-form is a Gaussian bell given by,

$$\rho^2 = e^{-\frac{(x-x_0)^4}{h_x}} e^{-\frac{(y-y_0)^4}{h_y}} dxdy, \tag{7-10}$$

where $(x_0, y_0) = (0.3, 0.3)$ and $h_x = h_y = 0.001$. Figure 7-12 shows the advection of the Gaussian bell 2-form, with $\Delta x = \Delta y = 0.25$ and space polynomial of order 9, for different times.

Figure 7-13 shows the the backtrack of the mesh grid after 1 second of physical time with different mesh size. It is clear that the backtrack of the quadrature points can lead to points between two different elements. As discussed in Chapter 5 the edge functions are discontinuous among elements. Thus, it can happen that integration is done between two discontinuous functions, something that quadrature rule do not handle properly.

Figure 7-14 shows the global mass error function of the number of elements. Opposite to what expected, as the number of elements increases the global mass error increases. This happens because as the number of elements increases the integration error increases.

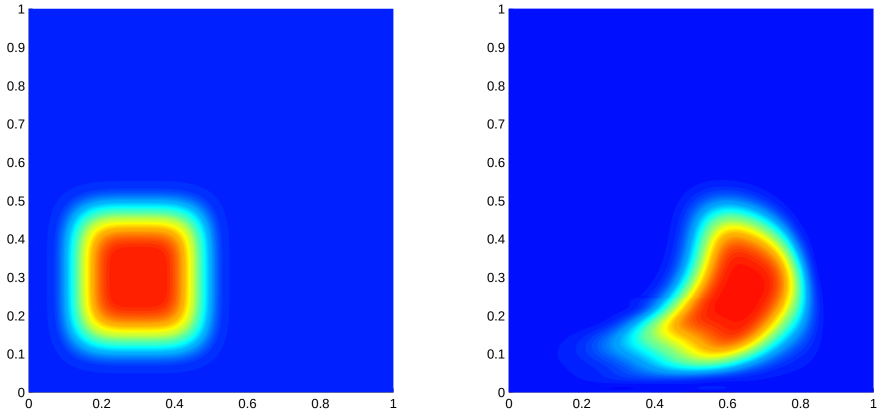

(a) t $= 0$ **(b)** t $= 0.05$s

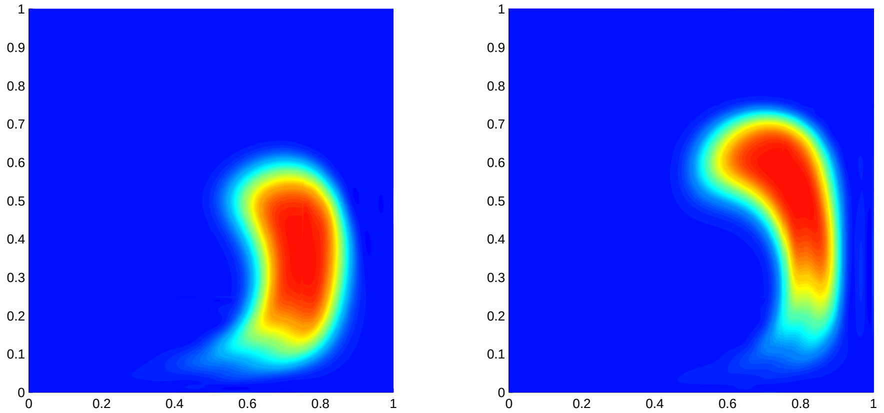

(c) t $= 0.075$s **(d)** t $= 1$ s

Figure 7-12: 2D advection of a 2-form Gaussian bell with $N_x = N_y = 4$ and $p_x = p_y = 9$

One simple alternative is to determine where both the backtracked and the initial mesh intersect and create different integration regions. This linear clipping idea is compared with the standard quadrature in Figure 7-14. For $p_x = 1$ the error from this different quadrature is numerically zero. However, has the space polynomial order increases, even with this different quadrature, the error increases because the linear intersection is not able to cope with curved meshes. Major drawback of this is the algorithm complexity. Figure 7-15 shows a geometric interpretation of this clipping idea.

Figure 7-3 shows two ideas for the path tube method with and without restart. This can also be extended to the backtrack flux approach. The major advantage of this approach is the reducing the computational time required. However, before solving the influence the integration error this approach will only amplify the error every time step.

It is left for future research the advection of 1-forms in 2D, although the implementation

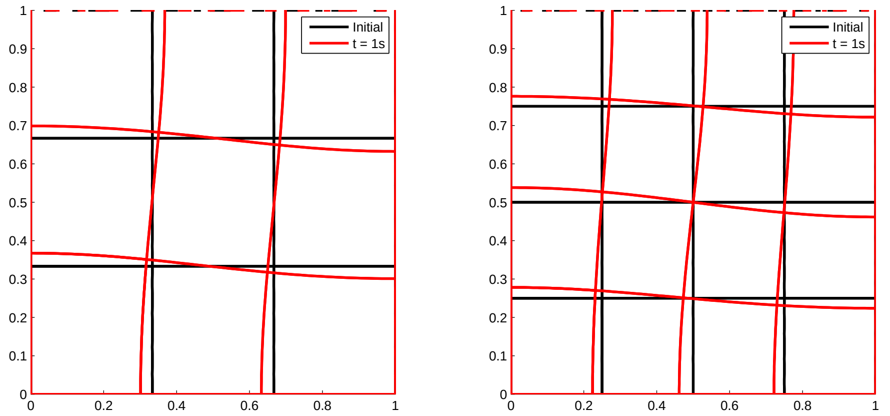

(a) $N_x = N_y = 3$ **(b)** $N_x = N_y = 4$

Figure 7-13: 2D backtrack of the integration points for $p = 9$ after 1 second of simulation time (the origin of quadrature errors)

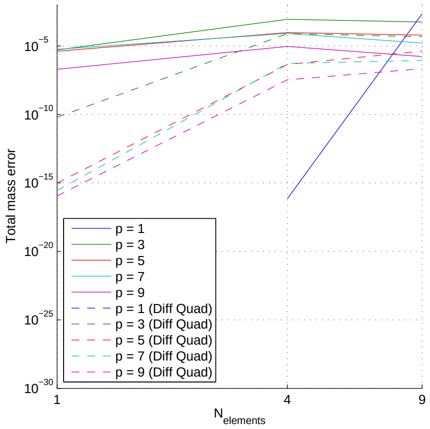

Figure 7-14: Mass error for the 2D path tube method

must be straightforward because instead of backtracking volumes or points it is the edge elements that should be backtracked. Dealing with boundary conditions is also left for future work. Traditionally, characteristic-based algorithms are applied to open boundary problems (e.g. in groundwater applications) or to problems with periodic boundary conditions (like meteorological problems on a sphere). However, the characteristic-based schemes can be applied in problems with closed boundaries by stopping the characteristic lines where they cross the inlet boundaries, Figure 7-16 shows an idea proposed in the context of ELLAM method [3]. Furthermore, alternatives to quadrature have been proposed [61].

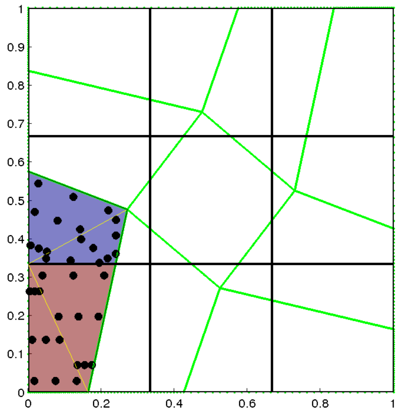

Figure 7-15: Different quadrature approach to compute the integral values in the 2D path tube method

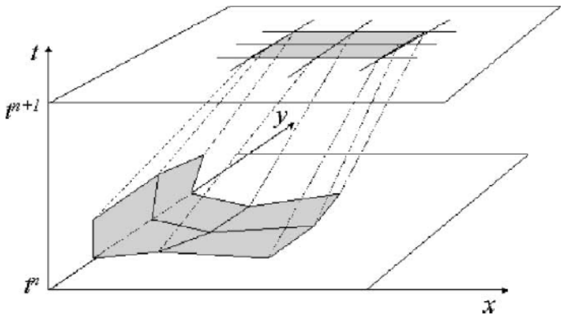

Figure 7-16: Boundary conditions implementation [3]

7-3 Eulerian

Most numerical schemes are Eulerian in nature. Eulerian methods are build on semi-discretization in space. It is well known that the classical Galerkin discretization when applied to pure convection leads to spurious (non-physical) oscillations [62]. Much attention as been devoted to this problem and several alternatives have been proposed to handle this [62]. In the case of scalar advection streamline upwind Petrov-Galerkin [63, 64], Galerkin/least-squares [65, 66] and Taylor-Galerkin [67, 68] are very popular schemes. A major drawback of all Eulerian methods is the limitation of CFL condition.

Furthermore, it is common to focus much of the attention and to acknowledge the spatial discretization as the major sort of numerical error. However, unphysical time discretization can reveal to be as much problematic has discrete spatial representation. Classical time marching schemes such as explicit Runge-Kutta will always add some artificial dissipation to the system compromising the kinetic energy. Oppositely, it is likely that symplectic time marching schemes allow the conservation of kinetic energy. This has been acknowledge in [69, 70] where a trapezoidal method, which is a low order symplectic scheme, has proven to preserve kinetic energy in the context of inviscid fluids. Still in the context of inviscid fluids, recently [71] developed a time-reversible integrator that preserves energy exactly. The time marching scheme used from this point onwards is derived based on the mimetic symplectic integrator introduced in Chapter 6. A geometric representation can be seen in Figure 7-17.

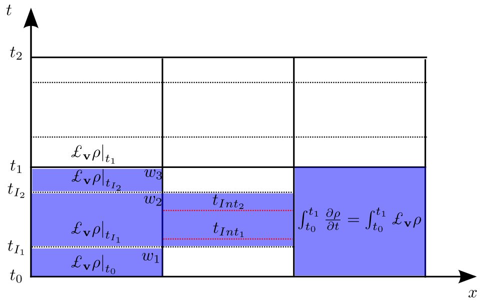
t
t_2
t_1
t_{I_2}
t_{I_1}
t_0
x
$\pounds_{\mathbf{v}}\rho|_{t_1}$
$\pounds_{\mathbf{v}}\rho|_{t_{I_2}}$
w_3
w_2
$\pounds_{\mathbf{v}}\rho|_{t_{I_1}}$
$\pounds_{\mathbf{v}}\rho|_{t_0}$
w_1
t_{Int_2}
t_{Int_1}
$\int_{t_0}^{t_1} \frac{\partial\rho}{\partial t} = \int_{t_0}^{t_1} \pounds_{\mathbf{v}}\rho$

Figure 7-17: Geometric representation of the time marching scheme

In order to compare the results with the ones obtained from the semi-Lagrangian discretization, the test cases are the same. Therefore, for 1D consider a constant velocity field, $\mathbf{v} = 1$, periodic boundary conditions and an 1-form $\rho^1 = sin\,(2\pi x) + 1dx$. The total physical time of simulation is of 10 seconds, which corresponds of 10 turns of the system.

The advection of a 1-form, $\rho^1 \in \mathbb{R}^1$, is given by,

$$\frac{\partial\rho^1}{\partial t} + \pounds_{\mathbf{v}}\rho^1 = 0, \tag{7-11}$$

where $\pounds_{\mathbf{v}}\rho^1 = d\iota_{\mathbf{v}}\rho^1$,

$$\frac{\partial\rho^1}{\partial t} + d\iota_{\mathbf{v}}\rho^1 = 0. \tag{7-12}$$

In vector calculus this can be seen as discretizing,

$$\frac{\partial\rho}{\partial t} + \mathbf{div}\,(\rho\mathbf{v}) = 0. \tag{7-13}$$

The discrete exterior derivative is simply an incidence matrix. The difficulty lies in discretizing the interior product. Keeping in mind that the interior product of a 1-form gives a 0-zero,

$$\iota_{\mathbf{v}}\rho^1 = v\rho^1. \tag{7-14}$$

Thus,

$$\left\langle \iota_{\mathbf{v}}\rho^1, \beta_0 \right\rangle = \left\langle q^0, \beta_0 \right\rangle \tag{7-15}$$

Let ρ^1 be expanded,

$$\rho^1 = \sum_{i=1}^{N_{l_x}} \rho_i e_i(x), \tag{7-16}$$

and

$$q^0 = \sum_{i=1}^{N_{px}} q_i h_i(x). \tag{7-17}$$

Then,

$$\left\langle \sum_{i=1}^{N_{l_x}} v_i \rho_i e_i(x), h_j(x) \right\rangle = \left\langle \sum_{i=1}^{N_{px}} q_i h_i(x), h_j(x) \right\rangle. \tag{7-18}$$

Then this allows to write a system,

$$M_{i,j}^T \rho_i v_i = N_{i,j}^T q_i, \tag{7-19}$$

where $M_{i,j} = \langle e_i(x), h_j(x) \rangle$ and $N_{i,j} = \langle h_i(x), h_j(x) \rangle$. After determining all q_i its only necessary to apply the exterior derivative $\mathbb{D}^{(0,1)}$. This ends the spatial discretization.

However, it is still necessary to define an accurate time discretization,

$$\int_{t_0}^{t_1} \frac{\partial \rho^1}{\partial t} = - \int_{t_0}^{t_1} \pounds_{\mathbf{v}}^h \rho^1. \tag{7-20}$$

This represents an ODE system that can be solved using the mimetic integrator previously introduced,

$$\rho_{t_1}^1 = \rho_{t_0}^1 - \sum_i \Delta t \pounds_{\mathbf{v}}^h \rho_{t_i}^1 w_i. \tag{7-21}$$

Figure 7-18 presents the solution and the error for different physical times. In fact this plot are slices of Figure 7-19 where it can be seen the space-time advection for the total physical time simulation with $N = 100$ with $p_x = 10$, this is the best space space discretization computed.

In Figure 7-19 it might seem that for $\Delta t = 10^{-1}$ that the image is blurred when compared with $\Delta t = 10^{-3}$. In fact the blurring is just a matter of time resolution. It is clear that the maximum error obtained is of the order of 10^{-10} and does not change significantly as the time step is refined.

Figure 7-20 plots the L^2 error function of the time step and the polynomial time order for the best spacial discretization available, i.e $N = 100$ and $p_x = 10$ and after 10 seconds of physical time simulation. The absolute value for which the convergence occurs is not exactly the zero machine and the reason for that is an error accumulation. Furthermore, as expected, using the Eulerian scheme it is not possible to use time steps as big as the semi-Lagrangian methods. Also, there is no clear trend of convergence.

Figure 7-21 shows the L^2 error for $\Delta t = 10^{-4}$ and $p_t = 10$, the best time discretization available. There is a clear difference for the absolute value for which the convergence occurs between 0 seconds and the final time of 10 seconds. Thus, there is some small numerical

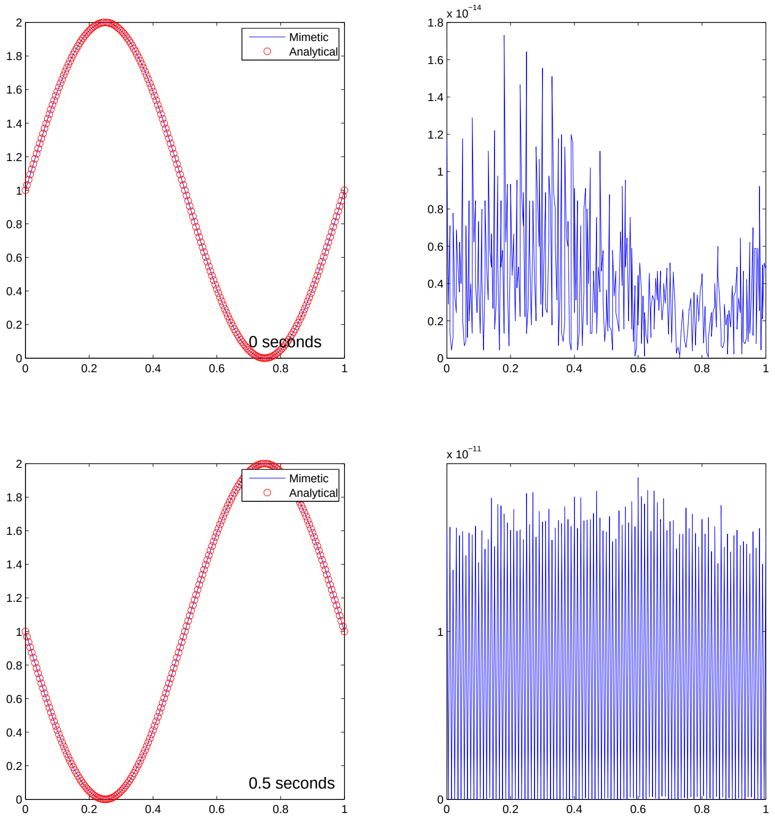

Figure 7-18: Comparison between the 1D advection of a 1-form, $sin(2\pi x) + 1dx$, with the analytical solution

diffusion or other spurious effect occurring. Even thought, there is still a spectral convergence with spatial order.

Figure 7-22 shows the L^2 error and the mass error for different time steps function of the number of iterations. For the case where $\Delta x = \Delta t$, i.e. $CFL = 1$, there is mass conservation. This means that all the quantities that is in one element is transfered for the adjacent one. The reason why mass is not preserved for other CFL conditions lies in the time interpolation used. There is the need to compute the fluxes in the intermediate time steps enforcing they are divergence free. Furthermore, there is an increase of the L^2 error function of the number of iterations. However, the rate of increase is function of the number of elements.

Figure 7-23 shows an example of the combination between the derived schemes for the discretization advection with diffusion. More details can be found [4].

7-3-1 2D

Although, no deep analysis is done in this section the extension of the previously defined framework is presented. It is left for future work a convergence study.

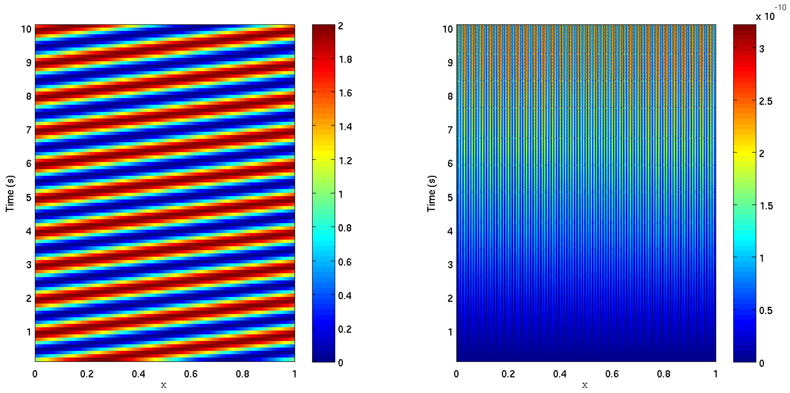

(a) $\Delta t = 10^{-1}$

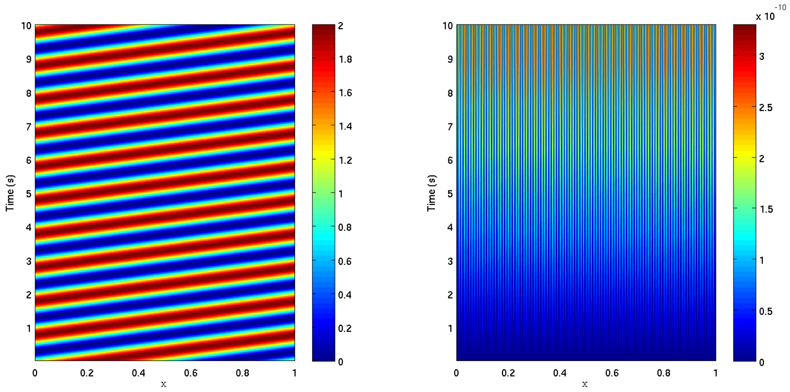

(b) $\Delta t = 10^{-2}$

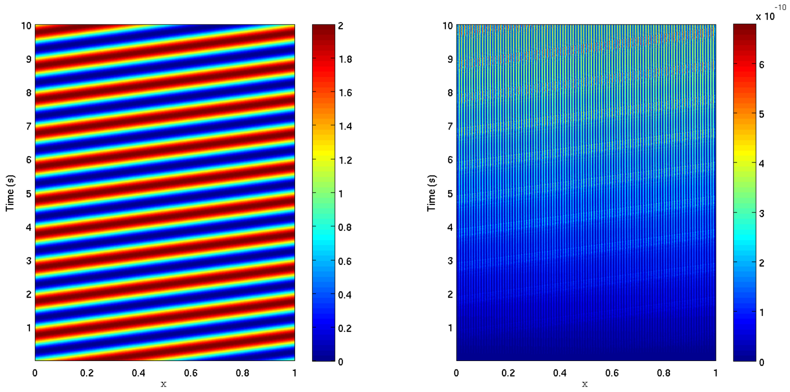

(c) $\Delta t = 10^{-4}$

Figure 7-19: Space-time 1D advection of a 1-form, $sin(2\pi x) + 1dx$

For a 2-form, $\rho^2 \in \mathbb{R}^2$, the Lie Derivative is given by,

$$\pounds_{\mathbf{v}} \rho^2 = d\iota_{\mathbf{v}} \rho^2. \tag{7-22}$$

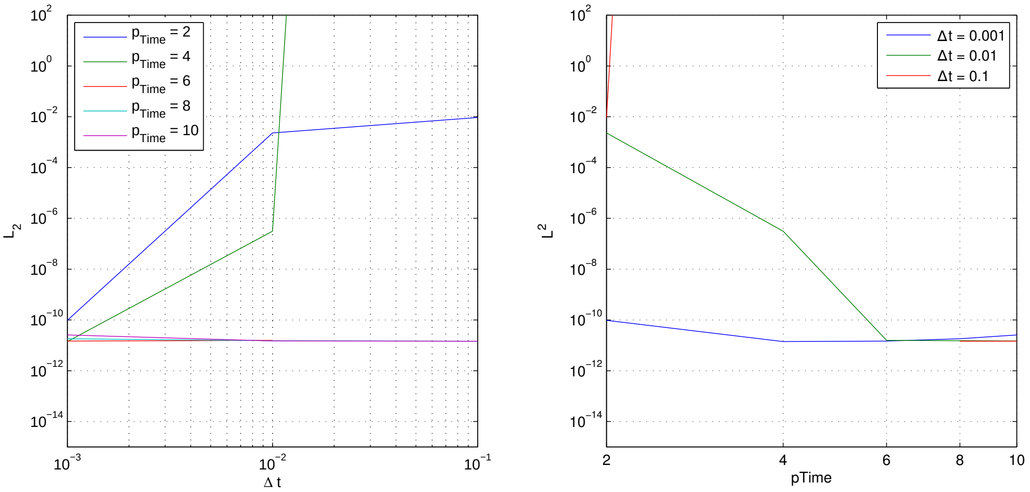

Figure 7-20: L^2 error of the Eulerian method for $N = 100$ and $p_x = 10$

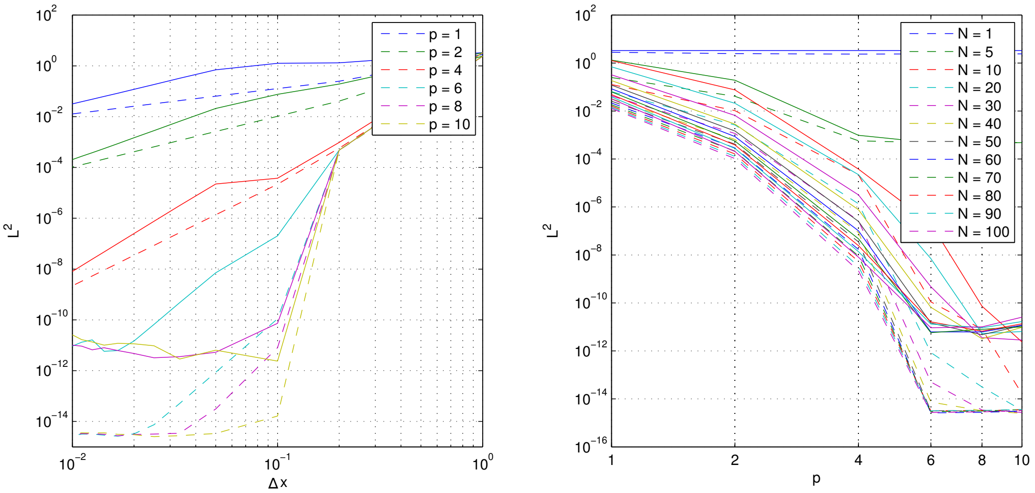

Figure 7-21: Convergence plot for the initial and after advection of $\rho^1 = sin(2\pi x) + 1dx$ with $\Delta t = 10^{-4}$ (– – Initial ; — Final)

Thus, the advection of a 2-form is given by,

$$\frac{\partial \rho^2}{\partial t} + d\iota_{\mathbf{v}}\rho^2 = 0. \tag{7-23}$$

In vector calculus this can be seen as,

$$\frac{\partial \rho}{\partial t} + \mathbf{div}\,(\rho\mathbf{v}) = 0. \tag{7-24}$$

Consider the 2-form, ρ^2 is given by,

$$\rho^2 = \rho dxdy. \tag{7-25}$$

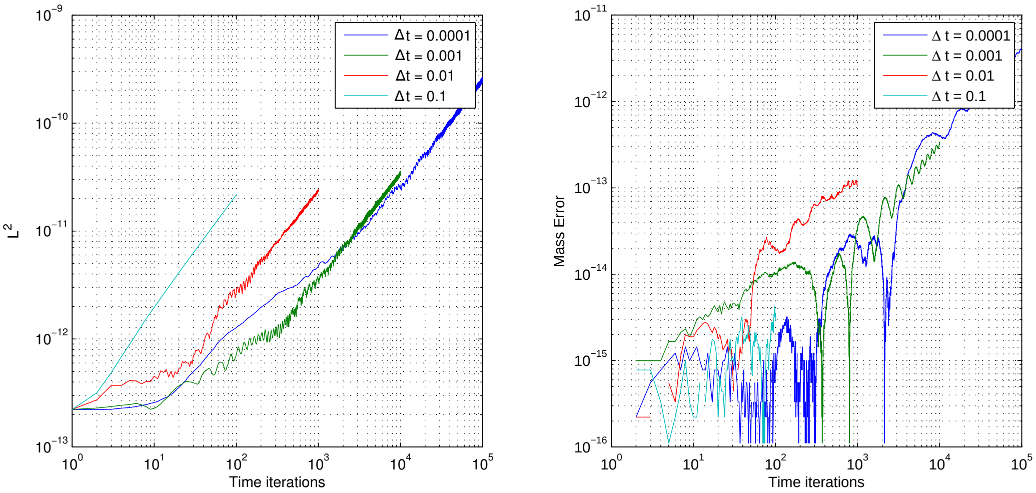

$\Delta x = 0.1$

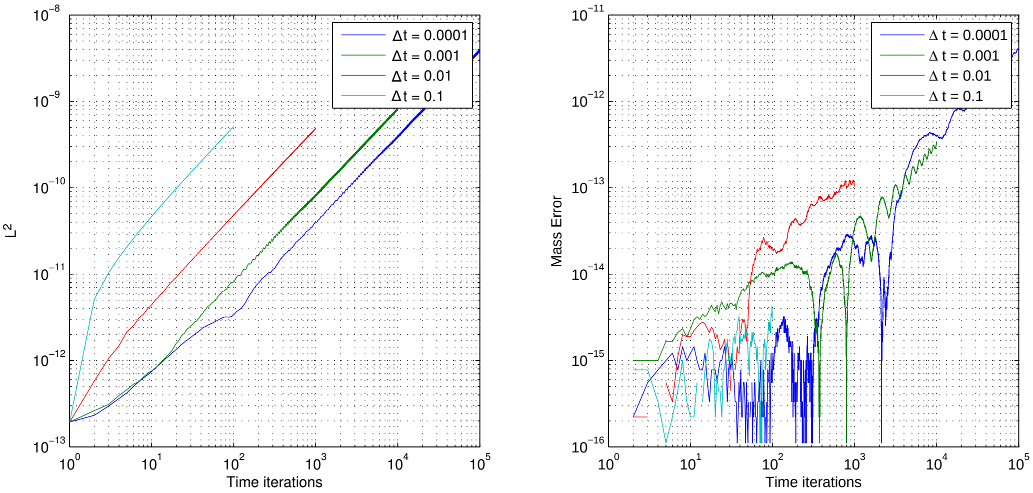

$\Delta x = 0.02$

Figure 7-22: Time error advection of a 1-form, $sin(2\pi x) + 1dx$

The interior product with the vector, $\mathbf{v} = v_x dx + v_y dy$, is given by,

$$\iota_{\mathbf{v}}\rho^2 = v_x\rho^2 dy - v_y\rho^2 dx. \tag{7-26}$$

Lets expand,

$$\rho^2 = \sum_{i=1}^{n_s} rho_i\phi_i, \tag{7-27}$$

where $\phi_i(x, y) = e(x)e(y)$. Then its possible to derive the following system,

$$M_{i,j}^T v_i^y \rho_i = N_{i,j}^T q_i^x, \tag{7-28}$$

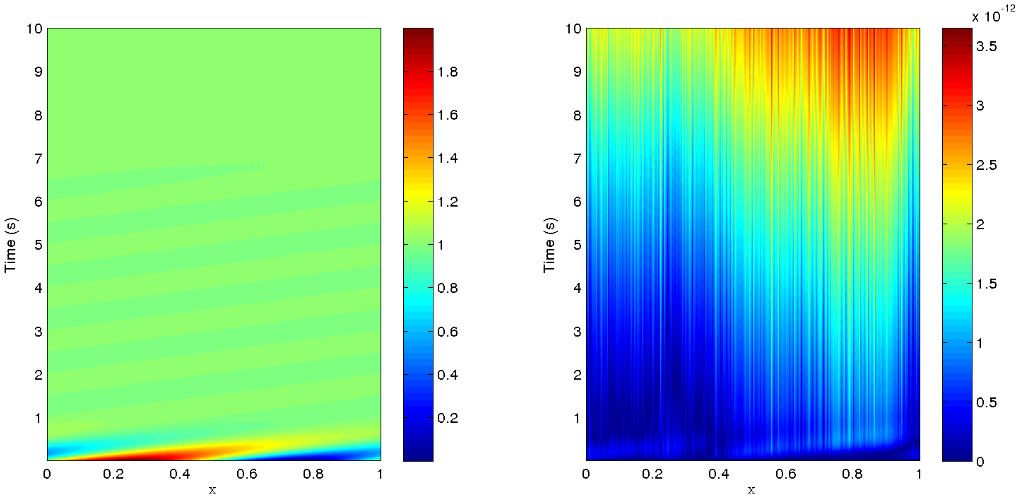

Figure 7-23: Space-time 1D advection-diffusion of a 1-form, $sin(2\pi x)+1dx$ with $N=90$,$px=10$ and a diffusion coefficient $=1$ [4]

where $M_{i,j}=\langle\phi_i(x,y),\xi_j(x,y)\rangle$ and $N_{i,j}=\langle\xi_i(x,y),\xi_j(x,y)\rangle$ with $\xi(x,y)=e(x)h(y)$. The same analysis can be done for the other term,

$$M^T_{i,j}v^x_i\rho_i=N^T_{i,j}q^y_i, \tag{7-29}$$

where $M_{i,j}=\langle\phi_i(x,y),\eta_j(x,y)\rangle$ and $N_{i,j}=\langle\eta_i(x,y),\eta_j(x,y)\rangle$ with $\eta(x,y)=h(x)e(y)$.

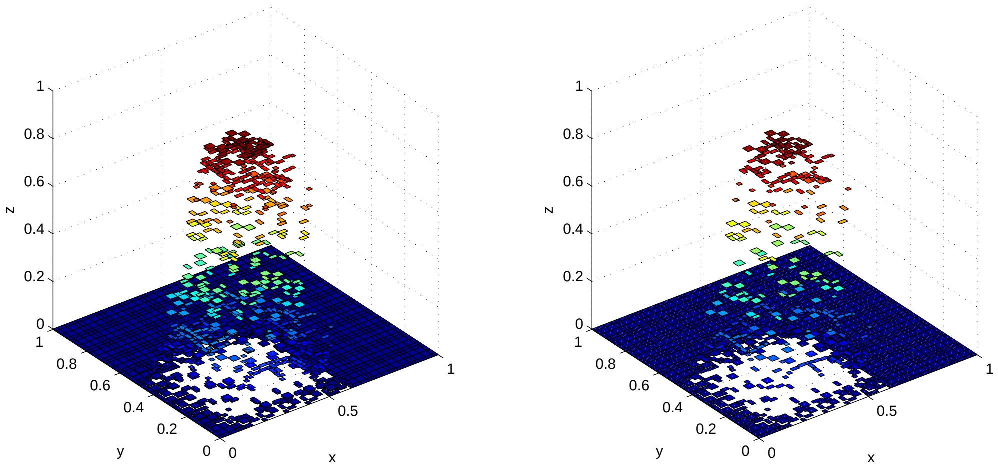

Figure 7-24: 2D advection of a 2-form Gaussian bell with $N_x=N_y=10$ and $p=4$

For a 1-form, α^1, the Lie Derivative is given by,

$$\pounds_{\mathbf{v}}\alpha^1=d\iota_{\mathbf{v}}\alpha^1+\iota_{\mathbf{v}}d\alpha^1. \tag{7-30}$$

Thus the advection of a 1-form, $\alpha^1 \in \mathbb{R}^2$, is given by,

$$\frac{\partial \alpha^1}{\partial t} + d\iota_{\mathbf{v}}\alpha^1 + \iota_{\mathbf{v}} d\alpha^1 = 0. \tag{7-31}$$

In vector calculus this corresponds to,

$$\frac{\partial \alpha}{\partial t} + \mathbf{curl}\,(\mathbf{v}) + \mathbf{vdiv}\,(\alpha)\,. \tag{7-32}$$

Consider the 1-form, α^1 is given by,

$$\alpha^1 = \alpha^1_x dx + \alpha^1_y dy. \tag{7-33}$$

The interior product with the vector, $\mathbf{v} = v_x dx + v_y dy$, is given by,

$$\iota_{\mathbf{v}}\alpha^1 = v_x \alpha^1_x + v_y \alpha^1_y. \tag{7-34}$$

Then expanding α^1,

$$\alpha^1 = \sum_{i=1}^{n_l x} \alpha_i \xi_i + \sum_{i=1}^{n_l y} \alpha_j \eta_j. \tag{7-35}$$

Then the following system can be constructed,

$$M^T_{i,k} v^y_i \rho_i + M^T_{j,k} v^x_j \rho_j = N^T_{i,j} q^x_i, \tag{7-36}$$

where $M_{i,k} = \langle \phi_i(x,y), \beta_k(x,y) \rangle$, $M_{j,k} = \langle \eta_j(x,y), \beta_k(x,y) \rangle$ and $N_{i,j} = \langle \beta_i(x,y), \beta_j(x,y) \rangle$ with $\beta(x,y) = h(x)h(y)$.

For a 0-form, α^0, the Lie Derivative is given by,

$$\pounds_{\mathbf{v}} \alpha^0 = \iota_{\mathbf{v}} d\alpha^0, \tag{7-37}$$

the term $d\alpha^0$ is a 1-form. Therefore, the treatment presented previously can be applied to this form.

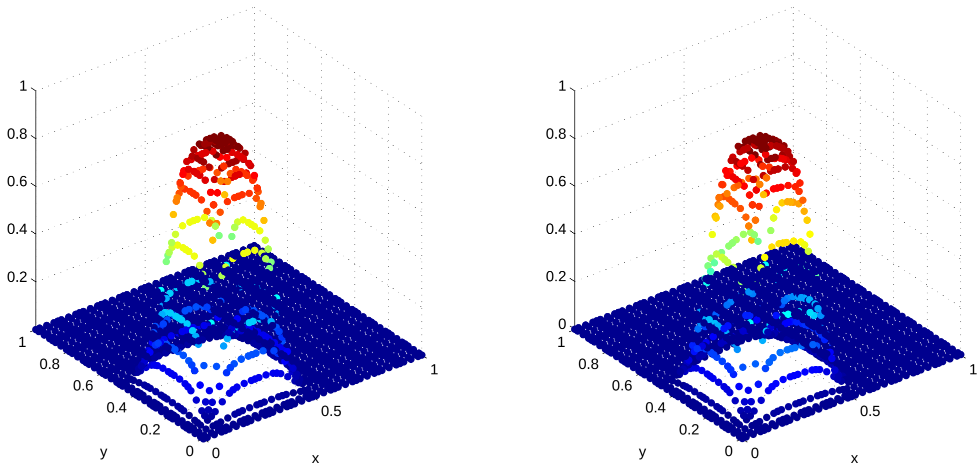

Figure 7-25: 2D advection of a 0-form Gaussian bell with $N_x = N_y = 10$ and $p = 4$

Chapter 8

Conclusions

This thesis merged spectral methods with the mimetic framework in order to design physical accurate discretizations of the generalized advection problem. The representation of discrete differential forms by algebraic topology offers the possibility to capture accurately the structures inherent to the problem.

The discretization of the interior product combined with the exterior product, thus, the Lie derivative allows the extension of the framework of mimetic spectral methods to hyperbolic problems. The use of known ideas of semi-Lagrangian schemes and the implementation of a flux based Eulerian perspective can be seen as span of classical scalar advection methods to the more generalized advection. It was clear in this thesis that both semi-Lagrangian and Eulerian methods have advantageous and disadvantageous.

To solve semi-Lagrangian methods it is necessary to compute the trajectory of the fluid particles. Thus, it is necessary to solve a set of ordinary differential equations. In this thesis a new arbitrary order mimetic integrator was presented and compared with a symplectic Gauss Runge-Kutta scheme. The mimetic scheme performs as good as the Gauss method in terms of energy convergence.

Semi-Lagrangian methods allow to choose larger time steps keeping the a good long term behavior. However, because of the discrete representation of the cochains, i.e. through basis functions that are discontinuous between elements, the quadrature error after backtracking is a major drawback.

On the other hand, Eulerian methods are computationally cheaper than semi-Lagrangian methods. However, the time step are more restricted and if the time marching scheme is not handed carefully results tend to get polluted over time. The limitations for both of these methods serve as motivation for future work.

8-1 Future work

The work developed during this thesis left open a set of numerical and theoretical challenges. Regarding the symplectic mimetic integrator it is left to be proven its formal symplectic nature. Remaining for future work is a detailed analysis of the behavior of the integrator using variable time steps, this has been reported as a drawback of symplectic integrators. Regarding the advection problem it remains has open direction a careful analysis of box schemes introduced by Keller [72] and Preissman [73]. In these methods space and time discretization are intimately coupled. Opposite to other methods, this ideas have proven powerful in wave propagation problems avoiding unphysical oscillations. These ideas have been applied to convection-diffusion in [74] and might reveal suitable for the generalized advection-diffusion of differential forms. Recently, the combination between discrete exterior calculus (DEC) and variational calculus have lead to exact preservation of momenta and good long-term energy behavior [22, 75]. The combination of these ideas with the mimetic spectral methods might reveal very fruitful.

The geometric nature of Fluid Mechanics, mainly Euler's equations for inviscid fluid have received some attention [76]. In here vorticity is represented as a two-form. This idea have been applied to obtain circulation preserving schemes [77]. Therefore, in the future it would be interesting to extend the use of the mimetic spectral methods, mainly the discrete Lie derivative developed in this thesis, to Euler's equation and later on to Navier-Stokes equations. However, to complete this goal it might be necessary the extension of this framework to operate not only in differential forms, but in arbitrary tensors, in such a way that the geometric identities remain intact. Furthermore, the extension of Kelvin's circulation to compressible fluids done by Bjerkne [78] can be also be used a starting point for further developments.

The application of differential geometry to other continuum theories such as magnetohydrodynamics (MHD) might prove very useful. In the case of MHD it is well known that the failure to preserve the divergence-free property of the magnetic field during simulation can lead to unphysical motions. This problem might be solve by a proper discretization through the use of mimetic methods.

Appendix A

Edge Functions

Integration is the mathematical operation that allows to associate physical variables with their respective geometric orientation, A-1 shows an example of this connection for density of an object,

$$\int_{\mathcal{M}^3} \rho dV = \left\langle \mathcal{M}^3, \rho \right\rangle \tag{A-1}$$

Spectral basis functions associated with points, lines, surfaces and volumes are the base for the numerical computations along this thesis. The use of quadrilateral elements its simple and can be done by applying tensor products.

A-1 The edge functions

Consider the one-dimensional equation,

$$u(\xi) = \frac{d\phi}{d\xi}, \quad \xi \in [a, b] \tag{A-2}$$

Let $a = \xi_0 < \xi_1 < \cdots < \xi_{N-1} < \xi_N = b$ be a partition of the interval $[a, b]$, then the function $\phi(\xi)$ can be expanded in nodal basis functions,

$$\phi(\xi) = \sum_{i=0}^{N} \phi_i h_i(\xi) \tag{A-3}$$

in which $h_i(\xi)$ are Lagrange basis functions through the points $\xi_i, i = 0, \cdots, N$ and $\phi_i = \phi(\xi_i)$. Its common in nodal approach to discretize $u(\xi)$ using the same Lagrange basis functions,

$$u(\xi) = \sum_{i=0}^{N} u_i h_i(\xi) \tag{A-4}$$

Combining A-3 and A-4,

$$\sum_{i=0}^{N} u_i h_i(\xi) = \sum_{i=0}^{N} \phi_i \frac{dh_i}{d\xi} \tag{A-5}$$

There are two main concerns with this approach. First of all, this formulation is not invariant under general C^1 coordinate transformations. Furthermore, a polynomial of degree N on the left hand side is equated to a polynomial of degree $N-1$ on the right hand side. Re-writing the equation in terms of differential geometry,

$$u^1 = d\phi^0 \tag{A-6}$$

Integrating this expression,

$$\phi(p) = \phi(q) + \int_q^p u(x)dx \tag{A-7}$$

It is possible to exactly satisfy $\bar{u_i} = \phi_i - \phi_{i-1}$ by defining, the integral quantities,

$$\bar{u_i} = \int_{\xi_{i-1}}^{\xi_i} u(x)dx, \quad i = 1, \cdots, N \tag{A-8}$$

Interpolation of integral quantities is called *histopolation* [79]. Its then possible to define,

$$\begin{aligned}
u^N(\xi) &= \sum_{i=0}^{N} \phi_i dh_i(\xi) \\
&= \sum_{i=0}^{N} (\phi_i \phi_k)\, dh_i(\xi) \\
&= \sum_{i=0}^{N} \left[-\sum_{j=i+1}^{k} \bar{u_j} + \sum_{j=k+1}^{i} \bar{u_j} \right] dh_i(\xi) \\
&= -\sum_{j=1}^{k} \left(\sum_{i=0}^{j-1} dh_i(\xi) \right) \bar{u_j} + \sum_{j=k+1}^{N} \left(\sum_{i=j}^{N} dh_j(\xi) \right) \bar{u_j}
\end{aligned} \tag{A-9}$$

Its possible to eliminate k by averaging over all k,

$$\begin{aligned}
u^N(\xi) &= \frac{1}{N+1} \sum_{k=0}^{N} u^N(\xi) \\
&= -\frac{1}{N+1} \sum_{k=0}^{N} \sum_{j=1}^{k} \left(\sum_{i=0}^{j-1} dh_i(\xi) \right) \bar{u}_j + \frac{1}{N+1} \sum_{k=0}^{N} \sum_{j=k+1}^{N} \left(\sum_{i=j}^{N} dh_i(\xi) \right) \bar{u}_j \\
&= \frac{1}{N+1} \sum_{j=1}^{N} \left[-(N+1)\bar{u}_j \sum_{i=0}^{j-1} dh_i(\xi) + j\bar{u}_j \sum_{i=0}^{N} dh_i(\xi) \right] \\
&= -\sum_{j=1}^{N} \bar{u}_j \sum_{i=0}^{j-1} dh_i(\xi)
\end{aligned} \tag{A-10}$$

Taking as basis function,

$$e_j(\xi) = -sum_{i=0}^{j-1} dh_i(\xi), \quad j = 1, \cdots, N \tag{A-11}$$

Thus, u can be expressed in terms of the integral quantities $\bar{u_i}$ as,

$$u^N(\xi) = sum_{i=1}^{N} \bar{u_i} e_i(\xi) \tag{A-12}$$

The basis function $e_i(\xi)$ satisfy,

$$\int_{\xi_{k-1}}^{\xi_k} e_i(x) = \delta_{i,k} = \begin{cases} 1 & \text{if } i = k \\ 0 & \text{if } i \neq k \end{cases} \tag{A-13}$$

The edge basis functions correspond in fact to a higher order Whitney forms [80]. Applying $de_j(\xi) = -d \circ d \sum h_i(\xi) \equiv 0$. Returning to A-2, now expanding u in terms of edge basis functions,

$$\sum_{i=1}^{N} \bar{u}_i e_i(\xi) = \sum_{i=0}^{N} \phi_i \eth_i(\xi) \tag{A-14}$$

$$= -\sum_{i=1}^{N} (\phi_i - \phi_{i-1}) \sum_{j=0}^{i-1} dh_j(\xi) \tag{A-15}$$

$$= \sum_{i=1}^{N} (\phi_i - \phi_{i-1}) \, e_i(\xi) \tag{A-16}$$

This solves the problems previously mentioned, i.e. the polynomial degrees match for both sides and this relation remains valid under arbitrary C^1 transformations. Since the basis functions, $e_i(\xi)$ are linearly independent,

$$\sum_{i=1}^{N} \left[\bar{u}_i - (\phi_i - \phi_{i-1})\right] e_i(\xi) = 0 \tag{A-17}$$

This is a purely topological, metric-free relation. What this means is that, once the boundary nodes of a given line are known this relation can be set up. This definition is shown to be exact and no approximations are involved.

A-1-1 Gradient operator

Consider

$$u = grad\phi \tag{A-18}$$

Lets expand ϕ as a tensor product of nodal functions in the coordinates (ξ, η, ζ)

$$\phi(\xi, \eta, \zeta) = \sum_{i=0}^{N} \sum_{j=0}^{N} \sum_{k=0}^{N} \phi_{i,j,k} h_i(\xi) h_j(\eta) h_k(\zeta) \tag{A-19}$$

then its possible to derive an exact, coordinate free and invariant under C^1 transformation,

$$\bar{u}^{\xi}_{i,j,k} = \phi_{i,j,k} - \phi_{i-1,j,k} \quad \bar{u}^{\eta}_{i,j,k} = \phi_{i,j,k} - \phi_{i,j-1,k} \quad \bar{u}^{\zeta}_{i,j,k} = \phi_{i,j,k} - \phi_{i,j,k-1} \tag{A-20}$$

with

$$\begin{aligned} u^{\xi}(\xi,\eta,\zeta) &= \sum_{i=1}^{N}\sum_{j=0}^{N}\sum_{k=0}^{N} \bar{u}^{\xi}_{i,j,k} e_i(\xi) h_j(\eta) h_k(\zeta) \\ u^{\eta}(\xi,\eta,\zeta) &= \sum_{i=0}^{N}\sum_{j=1}^{N}\sum_{k=0}^{N} \bar{u}^{\eta}_{i,j,k} h_i(\xi) e_j(\eta) h_k(\zeta) \\ u^{\zeta}(\xi,\eta,\zeta) &= \sum_{i=0}^{N}\sum_{j=0}^{N}\sum_{k=1}^{N} \bar{u}^{\zeta}_{i,j,k} h_i(\xi) h_j(\eta) e_k(\zeta) \end{aligned} \tag{A-21}$$

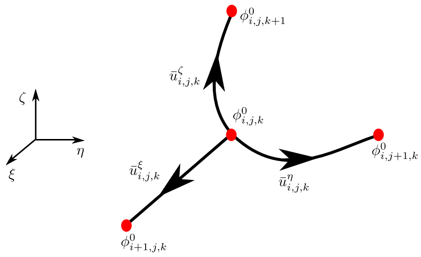

Figure A-1: Geometric representation of the discrete gradient operator

A-1-2 Curl operator

Let $\mathbf{u}$ be defined along edges then $w = curl\mathbf{u}$ is given by,

$$w^{\xi}_{i,j,k} = \bar{u}^{\zeta}_{i,j,k} - \bar{u}^{\zeta}_{i,j-1,k} - \bar{u}^{\eta}_{i,j,k} + \bar{u}^{\eta}_{i,j,k-1} \tag{A-22}$$

$$w^{\eta}_{i,j,k} = \bar{u}^{\xi}_{i,j,k} - \bar{u}^{\xi}_{i,j,k-1} - \bar{u}^{\zeta}_{i,j,k} + \bar{u}^{\zeta}_{i-1,j,k} \tag{A-23}$$

$$w^{\zeta}_{i,j,k} = \bar{u}^{\eta}_{i,j,k} - \bar{u}^{\eta}_{i-1,j,k} - \bar{u}^{\xi}_{i,j,k} + \bar{u}^{\xi}_{i,j-1,k} \tag{A-24}$$

$$\tag{A-25}$$

with

$$\begin{aligned} w^{\xi}(\xi,\eta,\zeta) &= \sum_{i=0}^{N}\sum_{j=1}^{N}\sum_{k=1}^{N} \bar{w}^{\xi}_{i,j,k} h_i(\xi) e_j(\eta) e_k(\zeta) \\ w^{\eta}(\xi,\eta,\zeta) &= \sum_{i=1}^{N}\sum_{j=0}^{N}\sum_{k=1}^{N} \bar{w}^{\eta}_{i,j,k} e_i(\xi) h_j(\eta) e_k(\zeta) \\ w^{\zeta}(\xi,\eta,\zeta) &= \sum_{i=1}^{N}\sum_{j=1}^{N}\sum_{k=0}^{N} \bar{w}^{\zeta}_{i,j,k} e_i(\xi) e_j(\eta) h_k(\zeta) \end{aligned} \tag{A-26}$$

This is again exact, metric free and invariant under C^1 transformations. Furthermore, if $\mathbf{u}$ is a gradient then $w^{\xi} = w^{\eta} = w^{\zeta} \equiv 0$ then,

$$u = grad\phi \Longleftrightarrow curlu = 0 \tag{A-27}$$

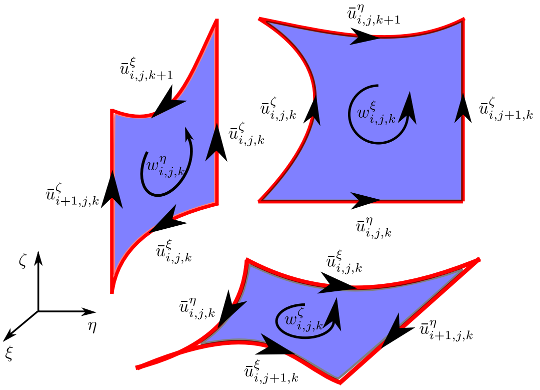
$\bar{u}^{\eta}_{i,j,k+1}$
$\bar{u}^{\xi}_{i,j,k+1}$
$\bar{u}^{\zeta}_{i,j,k}$
$w^{\xi}_{i,j,k}$
$\bar{u}^{\zeta}_{i,j+1,k}$
$\bar{u}^{\zeta}_{i,j,k}$
$w^{\eta}_{i,j,k}$
$\bar{u}^{\zeta}_{i+1,j,k}$
$\bar{u}^{\eta}_{i,j,k}$
$\bar{u}^{\xi}_{i,j,k}$
ζ
$\bar{u}^{\xi}_{i,j,k}$
$\bar{u}^{\eta}_{i,j,k}$
$w^{\zeta}_{i,j,k}$
η
$\bar{u}^{\eta}_{i+1,j,k}$
ξ
$\bar{u}^{\xi}_{i,j+1,k}$

Figure A-2: Geometric representation of the discrete curl operator

A-1-3 Divergence operator

Considering the divergence equation,

$$a = div f \tag{A-28}$$

Given fluxes defined over surfaces. Let the flux vector be expanded as

$$\begin{aligned}
f^{\xi}(\xi,\eta,\zeta) &= \sum_{i=0}^{N}\sum_{j=1}^{N}\sum_{k=1}^{N} \bar{f}^{\xi}_{i,j,k} h_i(\xi) e_j(\eta) e_k(\zeta) \\
f^{\eta}(\xi,\eta,\zeta) &= \sum_{i=1}^{N}\sum_{j=0}^{N}\sum_{k=1}^{N} \bar{f}^{\eta}_{i,j,k} e_i(\xi) h_j(\eta) e_k(\zeta) \\
f^{\zeta}(\xi,\eta,\zeta) &= \sum_{i=1}^{N}\sum_{j=1}^{N}\sum_{k=0}^{N} \bar{f}^{\zeta}_{i,j,k} e_i(\xi) e_j(\eta) h_k(\zeta)
\end{aligned} \tag{A-29}$$

If a is expanded in terms of the volume basis functions

$$a(\xi,\eta,\zeta) = \sum_{i=1}^{N}\sum_{j=1}^{N}\sum_{k=1}^{N} \bar{a}_{i,j,k} e_i(\xi) e_j(\eta) e_k(\zeta) \tag{A-30}$$

the divergence operator reduces to

$$\bar{a}_{i,j,k} = \bar{f}^{\xi}_{i,j,k} - \bar{f}^{\xi}_{i-1,j,k} + \bar{f}^{\eta}_{i,j,k} - \bar{f}^{\eta}_{i,j-1,k} + \bar{f}^{\zeta}_{i,j,k} - \bar{f}^{\zeta}_{i,j,k-1} \tag{A-31}$$

Once more, no numerical approximations are involved and the divergence equation reduces to a topological equation which is independent of the basis functions. If the fluxes are $\mathbf{f} = curl\mathbf{w}$ then,

$$div\mathbf{f} = 0 \Longleftrightarrow \mathbf{f} = curl\mathbf{w} \tag{A-32}$$

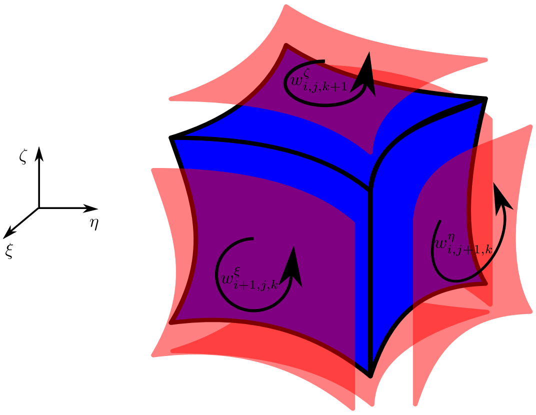
ζ
η
ξ
$w^{\zeta}_{i,j,k+1}$
$w^{\eta}_{i,j+1,k}$
$w^{\xi}_{i+1,j,k}$

Figure A-3: Geometric representation of the discrete divergence operator

Appendix B

Geometric integration tableaus

In this appendix a set of Butcher tableaus can be found for the fully implicit Gauss method.

B-1 Gauss

Table B-1: Gauss method of order 6

$\frac{1}{2}-\frac{\sqrt{15}}{10}$	$\frac{5}{36}$	$\frac{2}{9}-\frac{\sqrt{15}}{15}$	$\frac{5}{36}-\frac{\sqrt{15}}{30}$
$\frac{1}{2}$	$\frac{5}{36}+\frac{\sqrt{15}}{24}$	$\frac{2}{9}$	$\frac{5}{36}-\frac{\sqrt{15}}{24}$
$\frac{1}{2}+\frac{\sqrt{15}}{10}$	$\frac{5}{36}+\frac{\sqrt{15}}{30}$	$\frac{2}{9}+\frac{\sqrt{15}}{15}$	$\frac{5}{36}$
	$\frac{5}{18}$	$\frac{4}{9}$	$\frac{5}{18}$

Table B-2: Gauss method of order 8

$$w(1,1) = \frac{1}{8} - \frac{\sqrt{30}}{144} \qquad w(1,2) = \frac{1}{8} + \frac{\sqrt{30}}{144}$$

$$w(2,1) = \frac{1}{2}\sqrt{\frac{15+2\sqrt{30}}{35}} \qquad w(2,2) = \frac{1}{2}\sqrt{\frac{15-2\sqrt{30}}{35}}$$

$$w(3,1) = w(2,1)\frac{1/6+\sqrt{30}}{24} \qquad w(3,2) = w(2,2)\frac{1/6-\sqrt{30}}{24}$$

$$w(4,1) = w(2,1)\frac{1/21+5\sqrt{30}}{168} \qquad w(4,2) = w(2,2)\frac{1/21-5\sqrt{30}}{168}$$

$$w(5,1) = w(2,1) - 2w(3,1) \qquad w(5,2) = w(2,2) - 2w(3,2)$$

$\frac{1}{2} - w(2,1)$	w(1,1)	w(1,2)-w(3,1)+w(4,2)	w(1,2)-w(3,1)-w(4,2)	w(1,1)-w(5,1)
$\frac{1}{2} - w(2,2)$	w(1,1)-w(3,2)+w(4,1)	w(1,2)	w(1,2)-w(5,2)	w(1,1)-w(3,2)-w(4,1)
$\frac{1}{2} + w(2,2)$	w(1,1)+w(3,2)+w(4,1)	w(1,2)+w(5,2)	w(1,2)	w(1,1)+w(3,2)-w(4,1)
$\frac{1}{2} + w(2,1)$	w(1,1)+w(5,1)	w(1,2)+w(3,1)+w(4,2)	w(1,2)+w(3,1)-w(4,2)	w(1,1)
	2 w(1,1)	2 w(1,2)	2 w(1,2)	2 w(1,1)

Table B-3: Gauss method of order 10

$$
\begin{aligned}
w(1,1) &= \frac{322-13\sqrt{70}}{3600} & w(1,2) &= \frac{322+13\sqrt{70}}{3600}\\
w(2,1) &= \frac{1}{2}\sqrt{\frac{35+2\sqrt{70}}{63}} & w(2,2) &= \frac{1}{2}\sqrt{\frac{35-2\sqrt{70}}{63}}\\
w(3,1) &= w(2,1)\frac{452+59\sqrt{70}}{3240} & w(3,2) &= w(2,2)\frac{452-59\sqrt{70}}{3240}\\
w(4,1) &= w(2,1)\frac{64+11\sqrt{70}}{1080} & w(4,2) &= w(2,2)\frac{64-11\sqrt{70}}{1080}\\
w(5,1) &= 8w(2,1)\frac{23-\sqrt{70}}{405} & w(5,2) &= 8w(2,2)\frac{23+\sqrt{70}}{405}\\
w(6,1) &= w(2,1)-2w(3,1)-w(5,1) & w(6,2) &= w(2,2)-2w(3,2)-w(5,2)\\
w(7,1) &= w(2,1)\frac{308-23\sqrt{70}}{960} & w(7,2) &= w(2,2)\frac{308+23\sqrt{70}}{960}
\end{aligned}
$$

$\frac{1}{2}-w(2,1)$	w(1,1)	w(1,2)-w(3,1)+w(4,2)	32/225-w(5,1)	w(1,2)-w(3,1)-w(4,2)	w(1,1)-w(6,1)
$\frac{1}{2}-w(2,2)$	w(1,1)-w(3,2)+w(4,1)	w(1,2)	32/225-w(5,2)	w(1,2)-w(6,2)	w(1,1)-w(3,2)-w(4,1)
$\frac{1}{2}$	w(1,1)+w(7,1)	w(1,2)+w(7,2)	32/225	w(1,2)-w(7,2)	w(1,1)-w(7,1)
$\frac{1}{2}+w(2,2)$	w(1,1)+w(3,2)+w(4,1)	w(1,2)+w(6,2)	32/225+w(5,2)	w(1,2)	w(1,1)+w(3,2)-w(4,1)
$\frac{1}{2}+w(2,1)$	w(1,1)+w(6,1)	w(1,2)+w(3,1)+w(4,2)	32/225+w(5,1)	w(1,2)+w(3,1)-w(4,2)	w(1,1)
	2 w(1,1)	2 w(1,2)	64/225	2 w(1,2)	2 w(1,1)

Appendix C

Outer solar system

In this appendix the initial conditions used to simulate the outer solar system in Chapter 6 are given. The gravitational constant, $G = 2.95912208286e - 4$. Furthermore, the masses of the system are relative to the mass of the sun and are summarized in Table C-1.

Table C-1: Mass of the planets relative to the mass of the sun for the outer solar system simulation

Sun + inner planets	1.00000597682
Jupiter	9.54786104043e-4
Saturn	2.85583733151e-4
Uranus	4.37273164546e-5
Neptune	5.17759138449e-5
Pluto	7.692307692307693e-9

Distances are measured in astronomical units (1[A.U.] = 149597870 [km]) and time in earth days. Initial locations and velocities are given in Table C-2

Table C-2: Initial position and velocity of the planets relative to the mass of the sun for the outer solar system simulation

	Position = (q_1, q_2, q_3)	Velocity = (p_1, p_2, p_3)
Sun + inner planets	0	0
	0	0
	0	0
Jupiter	0.00565429	0
	-3.0458353	-0.00412490
	-1.5507963	-0.00190589
Saturn	0.00168318	0
	-3.8169847	0.00483525
	-1.6483708	0.00192462
Uranus	8.3101420	0.00354178
	-16.2901086	0.00137102
	-7.2521278	0.00055029
Neptune	11.4707666	0.00288930
	-25.7294829	0.00114527
	-10.8169456	0.00039677
Pluto	-15.5387357	0.00276725
	-25.2225594	-0.00170702
	-3.1902382	-0.00136504

Bibliography

[1] D. N. Arnold, R. S. Falk, and R. Winther, “Finite element exterior calculus: from (hodge) theory to numerical stability,” Aug. 2009.

[2] G. W. Ernst Hairer, Christian Lubich, *Geometric Numerical Integration: Structure-Preserving Algorithms for Ordinary Differential Equations.* Springer, 2006.

[3] T. F. Russell and M. A. Celia, “An overview of research on eulerian-lagrangian localized adjoint methods (ellam),” *Advances in Water Resources*, vol. 25, pp. 1215–1231, 2002.

[4] A. Palha. PhD thesis, Delft University Technology, 2011.

[5] J. B. Perot, “Discrete conservation properties of unstructured mesh schemes,” *Annual Review of Fluid Mechanics*, vol. 43, no. 1, pp. 299–318, 2011.

[6] E. Tonti, *On the formal structure of physical theories.* PhD thesis, Italian National Research Council, 1975.

[7] A. Bossavit, *Differential Geometry for the student of numerical methods in Electromagnetism.* Électricité de France, Études et Recherches, 1991.

[8] W. L. Burke, *Applied Differential Geometry.* Cambridge University Press, 1985.

[9] H. Flanders, *Differential forms with Applications to the Physical Sciences.* Dover Publications, 1989.

[10] P. Bochev and J. Hyman, “Principles of mimetic discretizations of differential operators,” in *Compatible Spatial Discretizations* (D. N. Arnold, P. B. Bochev, R. B. Lehoucq, R. A. Nicolaides, and M. Shashkov, eds.), vol. 142 of *The IMA Volumes in Mathematics and its Applications*, pp. 89–119, Springer New York, 2006.

[11] A. N. Hirani, *Discrete exterior calculus.* PhD thesis, California Institute of Technology, 2003.

[12] J. M. Hyman and M. Shashkov, “Mimetic discretizations for maxwell’s equations,” *J. Comput. Phys*, vol. 151, pp. 881–909, 1999.

[13] A. P. J.J. Kreeft and M. Gerritsma, "Mimetic spectral element method for generalized convection-diffusion problems," in *V European Conference On Computational Fluid Dynamics Eccomas CFD 2010*, 2010.

[14] C. Canuto, M. Hussaini, A. Quarteroni, and T. Zang, *Spectral methods.* Springer, 2006.

[15] G. Karniadakis and S. Sherwin, *Spectral/hp element methods for computational fluid dynamics.* Oxford University Press, USA, 2005.

[16] D. Kuzmin, "A guide to numerical methods for transport equations." 2010.

[17] H. Roos, M. Stynes, and L. Tobiska, "Robust numerical methods for singularly perturbed differential equations,"

[18] B. Cockburn and C.-W. Shu, "Review article runge-kutta discontinuous galerkin methods for convection-dominated problems," *Journal of Scientific Computing*, 2001.

[19] R. LeVeque, *Finite volume methods for hyperbolic problems*, vol. 31. Cambridge University Press, 2002.

[20] P. Mullen, A. McKenzie, D. Pavlov, L. Durant, Y. Tong, E. Kanso, J. Marsden, and M. Desbrun, "Discrete lie advection of differential forms," *Foundations of Computational Mathematics*, vol. 11, pp. 131–149, 2011. 10.1007/s10208-010-9076-y.

[21] R. H. Holger Heumann, "Eulerian and semi-lagrangian methods for convection-diffusion for differential forms," *Discrete and Continuous Dynamical Systems*, vol. 29, pp. 1471–1495, 2011.

[22] D. Pavlov, P. Mullen, Y. Tong, E. Kanso, J. Marsden, and M. Desbrun, "Structure-preserving discretization of incompressible fluids," *Physica D: Nonlinear Phenomena*, vol. 240, no. 6, pp. 443 – 458, 2011.

[23] Z. Lei and T. Hou, "On the stabilizing effect of convection in three-dimensional incompressible flows," *Communications on Pure and Applied Mathematics*, vol. 62, no. 4, pp. 501–564, 2009.

[24] H. Cartan, *Differential forms.* Hermann, 1970.

[25] M. Fecko, *Differential Geometry and Lie Groups for Physicists.* Cambridge University Press, 2006.

[26] T. Frankel, *The Geometry of Physics.* Cambridge University Press, 2006.

[27] C. Mattiussi, "A reference discretization strategy for the numerical solution of physical field problems," in *Electron Microscopy and Holography* (P. W. Hawkes, ed.), vol. 121 of *Advances in Imaging and Electron Physics*, pp. 143 – 279, Elsevier, 2002.

[28] C. J. Isham, *Modern Differential Geometry for Physicist.* World Scientific Publishing Co,Re. Ltd., 2001.

[29] M. Perry, "Applications of differential geometry to physics," June 2009.

[30] M. Desbrun, E. Kanso, and Y. Tong, "Discrete differential forms for computational modeling," in *ACM SIGGRAPH ASIA 2008 courses*, SIGGRAPH Asia '08, (New York, NY, USA), pp. 15:1–15:17, ACM, 2008.

[31] A. Pressley, *Elementary Differential Geometry.* Springer, 2010.

[32] R. Hiptmair, "Discrete (hodge) operators," *Numerische Mathematik*, vol. 90, pp. 265–289, 1999.

[33] D. N. Arnold, R. S. Falk, and R. Winther, "Finite element exterior calculus, homological techniques, and applications," *Acta Numerica*, vol. 15, pp. 1–155, 2006.

[34] K. Warnick, R. Selfridge, and D. Arnold, "Teaching electromagnetic field theory using differential forms," *Education, IEEE Transactions on*, vol. 40, no. 1, pp. 53–68, 1997.

[35] A. Bossavit, "Extrusion, contraction: their discretization via whitney forms," *COMPEL: The International Journal for Computation and Mathematics in Electrical and Electronic Engineering*, vol. 22, pp. 470–480, 2003.

[36] V. Arnold, *Mathematical methods of classical mechanics*, vol. 60. Springer, 1989.

[37] B. Harrison, "The differential form method for finding symmetries," *SIGMA*, vol. 1, no. 001, p. 12, 2005.

[38] A. Hatcher, *Algebraic Topology.* Cambridge University Press, 2002.

[39] J. Dieudonné, *A History of Algebraic and Differential Topology, 1900 - 1960.* Birkhäuser Boston, 1989.

[40] K. Lipnikov, G. Manzini, F. Brezzi, and A. Buffa, "The mimetic finite difference method for the 3d magnetostatic field problems on polyhedral meshes," *J. Comput. Phys.*, vol. 230, pp. 305–328, January 2011.

[41] M. Bouman, "Mimetic spectral element methods for elliptic problems," Master's thesis, TU Delft, 2010.

[42] J. K. A. Palha and M. Gerritsma, "Numerical solution of advection equations with the discretization of the lie derivative," in *V European Conference on Computational Fluid Dynamics ECCOMAS CFD 2010*, 2010.

[43] J. Kreeft, A. Palha, and M. Gerritsma, "Mimetic framework on curvilinear quadrilaterals of arbitrary order," *Arxiv preprint arXiv:1111.4304*, 2011.

[44] R. Hiemstra, "Isogeometric mimetic methods - applied geometry in cfd," Master's thesis, TU Delft, 2011.

[45] A. Buffa, C. de Falco, and G. Sangalli, "Isogeometric analysis: stable elements for the 2d stokes equation," *International Journal for Numerical Methods in Fluids*, vol. 65, no. 11-12, pp. 1407–1422, 2011.

[46] J. A. Evans, *Divergence-free B-spline Discretizations for the Stokes and Navier-Stokes Equations.* PhD thesis, University of Texas at Austin, 2011.

[47] G. Oud, “Discrete differential geometry,” Master’s thesis, TU Delft, 2011.

[48] M. Gerritsma, “Edge functions for spectral element methods,” *Spectral and High Order Methods for Partial Differential Equations*, pp. 199–207, 2011.

[49] R. De Vogelaere, “Methods of integration which preserve the contact transformation property of the hamiltonian equations,” *University of Notre Dame preprint*, 1956.

[50] R. Ruth, “A canonical integration technique,” *IEEE Trans. Nucl. Sci*, vol. 30, no. 4, pp. 2699–2671, 1983.

[51] A. Cromer, “Stable solutions using the euler approximation,” *American Journal of Physics*, vol. 49, p. 455, 1981.

[52] J. Butcher and J. Wiley, *Numerical methods for ordinary differential equations.* Wiley Online Library, 2008.

[53] Y. Habib, *Long-term behaviour of G-symplectic methods.* PhD thesis, ResearchSpace@ Auckland, 2010.

[54] J. Monaghan, “Smoothed particle hydrodynamics,” *Reports on Progress in Physics*, vol. 68, p. 1703, 2005.

[55] D. Terzopoulos, J. Platt, A. Barr, and K. Fleischer, “Elastically deformable models,” in *ACM Siggraph Computer Graphics*, vol. 21, pp. 205–214, ACM, 1987.

[56] A. Wiin-Nielsen, “On the application of trajectory methods in numerical forecasting,” *Tellus*, vol. 11, no. 2, pp. 180–196, 1959.

[57] K. Boukir, Y. Maday, and B. Métivet, “A high order characteristics method for the incompressible navierŮstokes equations,” *Computer Methods in Applied Mechanics and Engineering*, vol. 116, no. 1-4, pp. 211 – 218, 1994.

[58] Claes and Johnson, “A new approach to algorithms for convection problems which are based on exact transport + projection,” *Computer Methods in Applied Mechanics and Engineering*, vol. 100, no. 1, pp. 45 – 62, 1992.

[59] O. Pironneau, “On the transport-diffusion algorithm and its applications to the navier-stokes equations,” *Numerische Mathematik*, vol. 38, no. 3, pp. 309–332, 1982.

[60] J. Pudykiewicz, “A class of semi-lagrangian approximations for fluids,” *J. Atmos. Sci*, vol. 49, pp. 2082–2096, 1992.

[61] A. Priestley, “Exact projections and the lagrange-galerkin method: A realistic alternative to quadrature,” *Journal of Computational Physics*, vol. 112, no. 2, pp. 316 – 333, 1994.

[62] V. John and P. Knobloch, “On spurious oscillations at layers diminishing (sold) methods for convection-diffusion equations: Part i-a review,” *Computer methods in applied mechanics and engineering*, vol. 196, no. 17-20, pp. 2197–2215, 2007.

[63] T. Hughes, L. Franca, and M. Mallet, “A new finite element formulation for computational fluid dynamics: Vi. convergence analysis of the generalized supg formulation for linear time-dependent multidimensional advective-diffusive systems,” *Computer Methods in Applied Mechanics and Engineering*, vol. 63, no. 1, pp. 97–112, 1987.

[64] D. Kelly, S. Nakazawa, O. Zienkiewicz, and J. Heinrich, "A note on upwinding and anisotropic balancing dissipation in finite element approximations to convective diffusion problems," *International journal for numerical methods in engineering*, vol. 15, no. 11, pp. 1705–1711, 1980.

[65] T. Hughes, L. Franca, and G. Hulbert, "A new finite element formulation for computational fluid dynamics: Viii. the galerkin/least-squares method for advective-diffusive equations," *Computer Methods in Applied Mechanics and Engineering*, vol. 73, no. 2, pp. 173–189, 1989.

[66] F. Shakib and T. Hughes, "A new finite element formulation for computational fluid dynamics: Ix. fourier analysis of space-time galerkin/least-squares algorithms," *Computer Methods in Applied Mechanics and Engineering*, vol. 87, no. 1, pp. 35–58, 1991.

[67] J. Donea, "A taylor–galerkin method for convective transport problems," *International Journal for Numerical Methods in Engineering*, vol. 20, no. 1, pp. 101–119, 1984.

[68] J. Donea, L. Quartapelle, and V. Selmin, "An analysis of time discretization in the finite element solution of hyperbolic problems," *Journal of Computational Physics*, vol. 70, no. 2, pp. 463–499, 1987.

[69] B. Perot, "Conservation properties of unstructured staggered mesh schemes," *Journal of Computational Physics*, vol. 159, no. 1, pp. 58–89, 2000.

[70] X. Zhang, D. Schmidt, and B. Perot, "Accuracy and conservation properties of a three-dimensional unstructured staggered mesh scheme for fluid dynamics," *Journal of Computational Physics*, vol. 175, no. 2, pp. 764–791, 2002.

[71] P. Mullen, K. Crane, D. Pavlov, Y. Tong, and M. Desbrun, "Energy-preserving integrators for fluid animation," *ACM Trans. Graph.*, vol. 28, pp. 38:1–38:8, July 2009.

[72] H. Keller, "A new difference scheme for parabolic problems," *Numerical solution of partial differential equations*, vol. 2, pp. 327–350, 1971.

[73] A. Preissmann, "Propagation des intumescences dans les canaux et rivieres," in *First Congress of the French Association for Computation, Grenoble, France*, pp. 433–442, 1961.

[74] J. Croisille and I. Greff, "An efficient box-scheme for convection–diffusion equations with sharp contrast in the diffusion coefficients," *Computers & fluids*, vol. 34, no. 4, pp. 461–489, 2005.

[75] E. Gawlik, *Geometric, Variational Discretization of Continuum Theories.* PhD thesis, California Institute of Technology, 2010.

[76] J. Marsden and A. Weinstein, "Coadjoint orbits, vortices, and clebsch variables for incompressible fluids," *Physica D: Nonlinear Phenomena*, vol. 7, no. 1-3, pp. 305–323, 1983.

[77] S. Elcott, Y. Tong, E. Kanso, P. Schröder, and M. Desbrun, "Stable, circulation-preserving, simplicial fluids," *ACM Transactions on Graphics (TOG)*, vol. 26, no. 1, p. 4, 2007.

[78] A. Thorpe, H. Volkert, and M. ZIEMIA1/4SKI, “The bjerknesŠcirculation theorem,” *Bulletin of the American Meteorological Society*, vol. 84, no. 4, p. 471, 2003.

[79] N. Robidoux, “Polynomial histopolation, superconvergent degrees of freedom, and pseudospectral discrete (hodge) operators,” *Unpublished: http://www. cs. laurentian. ca/n-robidoux/prints/super/histogram. pdf*, 2008.

[80] H. Whitney, *Geometric Integration Theory.* Dover Publications, 2005.